Title
Organic Tandem Solar Cells: Design and Formation

Author
Chen, Chun-Chao

Publication Date
2015

Peer reviewed|Thesis/dissertation

UNIVERSITY OF CALIFORNIA

Los Angeles

Organic Tandem Solar Cells: Design and Formation

A dissertation submitted in partial satisfaction of the

requirements for the degree Doctor of Philosophy

in Materials Science and Engineering

by

Chun-Chao Chen

2015

ABSTRACT OF THE DISSERTATION

Organic Tandem Solar Cells: Design and Formation

by

Chun-Chao Chen

Doctor of Philosophy in Materials Science and Engineering

University of California, Los Angeles, 2015

Professor Yang Yang, Chair

In the past decade, research on organic solar cells has gone through an important development stage leading to major enhancements in power conversion efficiency, from 4% to 9% in single-junction devices. During this period, there are many novel processing techniques and device designs that have been proposed and adapted in organic solar-cell devices. One well-known device architecture that helps maximize the solar cell efficiency is the multi-junction tandem solar-cell design. Given this design, multiple photoactive absorbers as subcells are stacked in a monolithic fashion and assembled via series connection into one complete device, known as the tandem solar cell. Since multiple absorbers with different optical energy bandgaps are being applied in one tandem solar-cell device, the corresponding solar cell efficiency is maximized through expanded absorption spectrum and reduced carrier thermalization loss.

In Chapter 3, the architecture of solution-processible, visibly transparent solar cells is introduced. Unlike conventional organic solar-cell devices with opaque electrodes (such as silver, aluminum, gold and etc.), the semi-transparent solar cells rely on highly transparent electrodes and visibly transparent photoactive absorbers. Given these two criteria, we first demonstrated the visibly transparent single-junction solar cells via the polymer absorber with near-infrared absorption and the top electrode based on solution-processible silver nanowire conductor. The highest visible transparency (400 ~ 700 nm) of 65% was achieved for the complete device structure. More importantly, power conversion efficiency of 4% was also demonstrated.

In Chapter 4, we stacked two semi-transparent photoactive absorbers in the tandem architecture in order to realize the semi-transparent tandem solar cells. A noticeable performance improvement from 4% to 7% was observed. More importantly, we modified the interconnecting layers with the incorporation of a thin conjugated polyelectrolyte layer functioning as the surface dipole formation layer to provide better electrical contact with the photoactive layer. Due to the effectiveness of the conjugated polyelectrolyte layer, performance improvement was also observed. Furthermore, other issues regarding the semi-transparent tandem solar cells (e.g., photocurrent matching, exterior color tuning, and transparency tuning) are all explored to optimize best performance.

In Chapter 5 and 6, the architectures of double- and triple-junction tandem solar cells are explored. Theoretically, triple-junction tandem solar cells with three photoactive absorbers with cascaded energy bandgaps have the potential to achieve higher performance, in comparison with double-junction tandem solar cells. Such expectations can be ascribed to the minimized carrier thermalization loss and further improved light absorption. However, the design of triple-junction

solar cells often involves sophisticated multiple layer deposition as well as substantial optimization. Therefore, there is a lack of successful demonstrations of triple-junction solar cells outperforming the double-junction counterparts.

To solve the incompatible issues related to the layer deposition in the fabrication, we proposed a novel architecture of inverted-structure tandem solar cells with newly designed interconnecting layers. Our design of interconnecting layers does not only focus on maintaining the orthogonal solution processing advantages, but also provides an excellent compatibility in the energy level alignment to allow different absorber materials to be used. Furthermore, we also explored the light management inside the double- and triple-junction tandem solar cells. The study of light management was carried out through optical simulation method based transfer matrix formalism. The intention is to obtain a balanced photocurrent output from each subcells inside the tandem solar cell, thus the minimal recombination loss at the contact of interconnecting layers and the optimal efficiency can be expected. With help from simulations, we were able to calibrate the thickness of each photoactive layer as well as the thickness of interconnecting layers to achieve the optimized processing conditions. With the highest power conversion efficiency, 11.5%, triple-junction tandem solar cells outperform the double-junction tandem solar cells at 10.5%.

In summary, this dissertation has provided practical solutions to the current demand of high-performance and easily manufactured organic solar cells from the solar cell industry. Particularly, triple-junction tandem solar cells with efficiencies over 11% should have great potential to contribute to high-efficiency solar-cell applications, whereas semi-transparent tandem solar cells with efficiency at 7% should be applicable to building-integrated applications.

The dissertation of Chun-Chao Chen is approved.

Pei-Yu (Eric) Chiou

Yu Huang

Paul Weiss

Yang Yang, Committee Chair

University of California, Los Angeles

2015

Table of Contents

List of Figures

List of Tables

List of Abbreviations

OPV	Organic photovoltaic
PSC	Polymer solar cells
HTL	Hole transporting layer
ETL	Electron transporting layer
D-A	Donor-acceptor
BHJ	Bulk heterojunction
PCE	Power conversion efficiency
EQE	External quantum efficiency
IQE	Internal quantum efficiency
HOMO	Highest occupied molecular orbital
LUMO	Lowest unoccupied molecular orbital
CB	Conduction band
VB	Valence band
WF	Work function
EA	Electron affinity
IE	Ionization potential
NP	Nanoparticles
ITO	Indium tin oxide
Ag	Silver
Au	Gold
Al	Aluminum

Ca	Calcium
MoO_3	Molybdenum oxide
V_2O_5	Vanadium oxide
WO_3	Tungsten oxide
TiO_2	Titanium oxide
ZnO	Zinc oxide
AgNW	Silver nanowire
TiO_2 NP	Titanium oxide nanoparticle
ITO NP	Indium tin oxide nanoparticle
PEDOT: PSS	poly-(3,4-ethylenedioxythiophene): poly(styrenesulfonate)
P3HT	poly(3-hexylthiophene)
PTB7-Th	Poly[4,8-bis(5-(2-ethylhexyl)thiophen-2-yl)benzo[1,2-b;4,5-b']dithiophene-2,6-diyl-alt-(4-(2-ethylhexyl)-3-fluorothieno[3,4-b]thiophene-)-2-carboxylate-2-6-diyl)]
PBDTT-DPP	poly(2,6'-4,8-di(5-ethylhexylthienyl)benzo[1,2-b;3,4-b]dithiophene-alt-5-dibutyloctyl-3,6-bis(5-bromothiophen-2-yl)pyrrolo[3,4-c]pyrrole-1,4-dione)
PBDTT-SeDPP	Poly(2,6'-4,8-di(5-ethylhexylthienyl)benzo[1,2-b;3,4-b]dithiophene-alt-2,5-bis(2-butyloctyl)-3,6-bis(selenophene-2-yl)pyrrolo[3,4-c]pyrrole-1,4-dione)
PBDTT-FDPP-C12	poly[4,8-bis(5-ethylhexyl-2-thienyl)-benzo[1,2- b:4,5-b']dithiophene-alt-2,5-n-tetradecyl-3,6-bis(furan-2-yl)pyrrolo[3,4-c]-pyrrole-1,4-dione]
PFN	Poly[(9,9-dioctyl-2,7-fluorene)- alt -(9,9-bis(3'-(N, N dimethylamino)propyl)-2,7-fl uorene)]
$PC_{61}BM$ or PCBM	[6,6]-phenyl-C61 butyric acid methyl ester
$PC_{71}BM$	[6,6]-phenyl-C71 butyric acid methyl ester
CB	Chlorobenzene
DCB	Dichlorobenzene
DIO	1, 8-diiodooctane

UV	Ultraviolet light
IR	Infaread light
VIS	Visible light
SEM	Scanning electron microscopy
WBG	Wide-bandgap material
LBG	Low-bandgap material
MBG	Medium-bandgap material
ICL	Interconnecting layers

List of Symbols

J	Current density
V	Voltage
J-V	Current density-voltage
J_{SC}	Short-circuit current density
V_{OC}	Open-circuit voltage
FF	Fill factor
η	Power conversion efficiency
P_{MAX}	Maximal power output
P_{LIGHT}	Incident light power intensity
R_S	Series resistance
R_{SH}	Shunt resistance
J_{ph}	Photocurrent density

V_{bi}	Built-in potential
ε_0	Permittivity of free space
ε_r	Dielectric constant
α	Absorption coefficient
τ	Carrier lifetime
ω	Resonance frequency
E_g	Energy bandgap
E_{opt}	Optical bandgap
L_D	Exciton diffusion length
n	Refractive index
k	Extinction coefficient
wt.	Weight percent
d	Film thickness
λ	Wavelength
$T_{average}$	Average visible transmission
T_{IR}	IR transmission

Acknowledgements

This work has come together as a result of continuous support, encouragement, and guidance from a group of important people in my life. First and foremost, I would like to express my deepest respect and gratitude to my advisor, Professor Yang Yang, for providing me with a unique opportunity to study and research at UCLA under his supervision. His encouragement and support have facilitated my growth for the past 5 years. I am also grateful for the guidance and advice from my committee members, Professor Pei-Yu (Eric) Chiou, Professor Yu Huang, and Professor Paul Weiss. I also like to express my sincere gratitude to Professor Benjamin J. Schwartz for his guidance in my first oral defense.

I would like to extend my sincere gratitude to group members in YY lab. I would like to thank Drs. Zhu Rui, Gang Li, Ziruo Hong, Jingbi You, Youjun He, Seiichiro Murase, Chih-Wei Chu, Zheng Xu, Sheng-han Li, Choong-Heui Chung, Run Xu and Ankit Kumar for their mentorship and helpful discussion. I would also like to thank all the friends and colleagues (Letain Dou, Jase Chang, Michael Yang, Steven A. Hawks, Rene Green, Min Cai, Jing Gao, Yongsheng Liu, Ryo Kokubu, Steve Hawks) at our OPV team and colleagues (Tze-Bin Song, Brion Bob, Shenglin Ye, Lei Bao, Wan-Ching Hsu, Hsin-Sheng Duan, Cara Hsu, XiaoHui Tan) at our CIGS team for their great team work and friendship.

My study was supported financially by the AFOSR (grant no. FA9550-09-1-0610), ONR (grant no. N000141110250), NSF (grant no. CHE0822573), NSFC (grant nos. 50633050 and 20821120293), Sumitomo Chemical Co., Ltd., and NSF-funded IGERT: Clean Energy for Green Industry Fellowship (grant no. DGE-0903720).

Last but not least, I would like to thank my parents and my families for their support.

Chapter 3 is a version of "Visibly transparent polymer solar cells produced by solution processing", Chun-Chao Chen, Letian Dou, Rui Zhu, Choong-Heui Chung, Tze-Bin Song, Yue Bing Zheng, Steve Hawks, Gang Li, Paul S. Weiss, and Yang Yang, *ACS Nano*, 6, 7185-7190 (2012). I would like to thank L. Dou for polymer synthesis. I would like to thank C-C. Chung, T-Z. Song, YB. Zheng, S. Hawks, and G. Li for fruitful discussions. The research is carried out under the supervision of Dr. Rui Zhu, Professor Paul Weiss and Professor Yang Yang.

Chapter 4 is a version of "High-performance semi-transparent polymer solar cells possessing tandem structures'', Chun-Chao Chen, Letian Dou, Jing Gao, Wei-Hsuan Chang, Gang Li and Yang Yang, *Energy and Environmental Science*, 6, 2714-2720 (2013). I would like to thank L. Dou and W-H. Chang for polymer synthesis. I would like to thank J. Gao and G. Li for fruitful discussions. The research is carried out under the supervision of Professor Yang Yang.

Chapter 5 and 6 are a version of "An efficient triple-Junction polymer solar cell having a power conversion efficiency exceeding 11%'', Chun-Chao Chen, Wei-Hsuan Chang, Ken Yoshimura, Kenichiro Ohya, Jingbi You, Jing Gao, Zirou Hong and Yang Yang, *Advanced Materials*, 26, 5670-5677 (2014). I would like to thank W-H. Chang, K. Yoshimura and K. Ohya for polymer synthesis. I would like to thank J. Gao, G. Li, and ZR. Hong for fruitful discussions. The research is carried out under the supervision of Professor Yang Yang.

VITA

2006 Bachelor of Science in Electrical and Computer Engineering

University of California, San Diego

San Diego, USA

2009 Master of Science in Material Science and Engineering

National Chiao Tung University

Hsinchu, Taiwan, ROC

Publications

Journal papers

1. **Chun-Chao Chen**, Wei-Hsuan Chang, Ken Yoshimura, Kenichiro Ohya, Jingbi You, Jing Gao, Zirou Hong and Yang Yang, "An efficient triple-junction polymer solar cell having a power conversion efficiency exceeding 11%'', *Advanced Materials*, **2014**, 26, 5670
2. **Chun-Chao Chen**, Letian Dou, Jing Gao, Wei-Hsuan Chang, Gang Li and Yang Yang, "High-performance semi-transparent polymer solar cells possessing tandem structures'', *Energy and Environmental Science*, **2013**, 6, 2714
3. **Chun-Chao Chen**, Letian Dou, Rui Zhu, Choong-Heui Chung, Tze-Bin Song, Yue Bing Zheng, Steve Hawks, Gang Li, Paul S. Weiss, and Yang Yang, "Visibly transparent polymer solar cells produced by solution processing", *ACS Nano*, **2012**, 6, 7185
4. Yongsheng Liu, **Chun-Chao Chen**, Ziruo Hong, Jing Gao, Yang Michael Yang, Huanping Zhou, Letian Dou, Gang Li, Yang Yang, ''Solution-processed small-molecule solar cells:

breaking the 10% power conversion efficiency'', *Scientific Reports*, **2013**, 3, 3356

5. Jingbi You, **Chun-Chao Chen**, Ziruo Hong, Ken Yoshimura, Kenichiro Ohya, Run Xu, Shenglin Ye, Jing Gao, Gang Li, Yang Yang, ''10.2% power conversion efficiency polymer tandem solar cells consisting of two identical sub-cells', *Advanced Materials*, **2013**, 25 (29), 3973-3978
6. Letian Dou, **Chun-Chao Chen**, Ken Yoshimura, Kenichiro Ohya, Wei-Hsuan Chang, Jing Gao, Yongsheng Liu, Eric Richard, and Yang Yang, "Synthesis of 5h-dithieno[3,2-b:2',3'-d]pyran as an electron-rich building block for donor–acceptor type low-bandgap polymers", *Macromolecules*, **2013**, 46, 3384
7. Jingbi You, **Chun-Chao Chen**, Letian Dou, Seiichiro Murase, Hsin-Sheng Duan, Steve Hawks, Tao Xu, Hae Jung Son, Luping Yu, Gang Li, and Yang Yang, "Metal oxide nanoparticles as electron transport layer in high performance and stable inverted polymer solar cells", *Advanced Materials*, **2012**, 24, 5267
8. Youjun He, **Chun-Chao Chen**, Eric Richard, Letian Dou, Yue Wu, Gang Li and Yang Yang, "Novel fullerene acceptors: synthesis and application in low band gap polymer solar cells", *Journal of Materials Chemistry*, **2012**, 22, 13391
9. Jingbi You, Letian Dou, Ken Yoshimura, Takehito Kato, Kenichiro Ohya, Tom Moriarty, Keith Emery, **Chun-Chao Chen**, Jing Gao, Gang Li, Yang Yang, "A polymer tandem solar cell with 10.6% power conversion efficiency'', *Nature Communications*, **2013**, 4, 1446
10. Letian Dou, Wei-Hsuan Chang, Jing Gao, **Chun-Chao Chen**, Jingbi You, Yang Yang, ''A selenium-substituted low-bandgap polymer with versatile photovoltaic applications'', *Advanced Materials*, **2013**, 25, 825
11. Jing Gao, Wei Chen, Letian Dou, **Chun-Chao Chen**, Wei-Hsuan Chang, Yongsheng Liu,

Gang Li, Yang Yang, "Elucidating double aggregation mechanisms in the morphology optimization of diketopyrrolopyrrole-based narrow bandgap polymer solar cells'', *Advanced Materials*, **2014**, 26, 3142

12. Jing Gao, Letian Dou, Wei Chen, **Chun-Chao Chen**, Xuanrong Guo, Jingbi You, Brion Bob, Wei-Hsuan Chang, Joseph Strzalka, Cheng Wang, Gang Li, Yang Yang, "Improving structural order for a high-performance diketopyrrolopyrrole-based polymer solar cell with a thick active layer'', *Advanced Energy Materials*, **2014**, 4, 1300739
13. Wei-Hsuan Chang, Jing Gao, Letian Dou, **Chun-Chao Chen**, Yongsheng Liu, Yang Yang, "Side-chain tunability via triple component random copolymerization for better photovoltaic polymers", *Advanced Energy Materials*, **2014**, 4, 1300864
14. Letian Dou, Jing Gao, Eric Richard, Jingbi You, **Chun-Chao Chen**, Kitty C Cha, Youjun He, Gang Li, Yang Yang, "Systematic investigation of benzodithiophene-and diketopyrrolopyrrole-based low-bandgap polymers designed for single junction and tandem polymer solar cells", *Journal of the American Chemical Society*, **2012**, 134, 10071

Conference Presentations

1. Chun-Chao Chen, Wei-Hsuan Chang and Yang Yang, "Triple-junction polymer tandem solar cell having a record-high PCE of 11.5%", oral presentation, MRS Fall 2014, Boston.
2. Chun-Chao Chen, and Yang Yang, "Triple-junction polymer tandem solar cell with a record-high efficiency of 11.5%", invited talk, 10th SPSJ International Polymer Conference (IPC 2014), Tsukuba, Japan.
3. Chun-Chao (Johnny) Chen, and Yang Yang, "High performance polymer solar cell via morphology understanding and tandem structure", invited talk, 2014 International Workshop on Flexible & Printable Electronics, Jeonju, Korea.

Chapter 1 Introduction to Organic Solar Cells

1.1 Introduction

"Tonight I want to have an unpleasant talk with you about a problem unprecedented in our history. With the exception of preventing war, this is the greatest challenge our country will face during our lifetimes. The energy crisis has not yet overwhelmed us, but it will if we do not act quickly", quoted from President Jimmy Carter's speech on 1977.

The energy issue has been the greatest challenge faced by mankind since industrial revolution. The US Energy Information Administration showed that the total world electrical consumption has reached a new record high of 19,000 TWh in 2013 due to the continuous growth in population.[1] Nevertheless, even with such high output of power there is still energy shortage issue in many countries and regions. The high demand of energy has given an opportunity to energy related research and technology to develop rapidly in the past few decades.

Solar cell technology, a unique kind of renewable technology that can extract electricity power directly from the sun, is first demonstrated in 1953 by Bell Labs with the first practical silicon solar cell.[2] Afterward, solar-cell technologies have progressed with the inventions of different inorganic materials applied as the photoactive layer in the solar cell devices. The examples are crystalline silicon, amorphous silicon, and III-V semiconductors (e.g., CdSe, GaAs, InP, and etc).[3] Nevertheless, most of these inorganic solar-cell technologies often involve high cost and high pollution manufacturing methods. More importantly, some of the inorganic solar cells also present environmental hazards due to the toxic elements (e.g., Cd) used in the devices. Therefore, a cleaner and more efficient solar cell technology is desired.

Organic solar cells, relatively recent developed solar-cell technologies, have attracted much attention during the past decade. Owning to its name "organic", the organic solar cell devices are largely based on the organic materials, such as small molecules, oligomers, and polymers. Since most of the elements of organic compounds are C, H, and O, they are considerably benign to environment. More importantly, organic solar cells have been developed initially with a process completely different from traditional silicon-based process. Solution-based processing, which is what organic compounds can be processed with, has greatly reduced the difficulties as well as the cost related to manufacturing. Therefore, organic solar cells, with potential in low-cost and environmental friendly process, are expected to be the next-generation solar cell technology.

1.2 History review of organic solar cells

The first successful demonstration of organic photovoltaics (OPV) was given by T. Feng et al. in 1978, with a single layer homojunction made of merocyanine with 0.7% power conversion efficiency (PCE).[4] Such OPV structures are based on metal-insulator-metal (MIM) structure in which a single organic layer is sandwiched between two electrodes of different work functions, as shown in the Figure 1.1a. The relatively low efficiency was due to the potential difference created by the work functions of metal electrodes being too small to separate the excitons created inside the organic layer into free charge carriers.

The next evolution was introduced to organic photovoltaics by C. W. Tang in 1985 with the concept of a bilayer heterojunction, in which two organic layers with a large difference in electron affinity were stacked in sequence to create a strong internal field to separate the excitons. This demonstration successfully improved the PCE to around 1%.[5] The enhanced photovoltaic

performance of the bilayer solar cell was attributed to the exciton separation now happening at the interfaces formed between the two organic materials instead of happening at the electrodes, as shown in Figure 1.1b. The organic layer with lower electron affinity is designated as *p*-type layer (or known as electron donor) whereas the organic layer with higher electron affinity is designated as *n*-type layer (or known as electron accepter). Although an improvement in bilayer OPV was observed, the bilayer structure is still limited by the short diffusion length of excitons (5 to 20 nm) generated by organic materials. Thus, bilayer OPV typically cannot have active layer thickness larger than 50 nm.

The next major evolution was introduced by A. J. Heeger and F. Wudl in 1992 with the concept of bulk heterojunction, in which two organic materials (one electron donor and one electron accepter) were blended in solution in order to form a randomly mixed bulk layer with numerous heterojunction and interfaces formed upon spin-coating. The first bulk heterojunction based on a mixture of MEH-PPV and a soluble fullerene derivative, PCBM, could achieve a remarkable efficiency at 1.5%.[6] This improvement can be ascribed to the formation of three-dimensional interpenetrating network of donor and acceptor materials throughout the entire active layer. Thus when excitons are generated, they can easily find a donor-acceptor interface nearby for separation and the free charge carriers can travel to an electrode along connected network, which is created by the phase separation of two organic materials due to differences in solvent solubility and surface energy. Figure 1.1c shows an example of a bulk heterojunction organic solar cell.

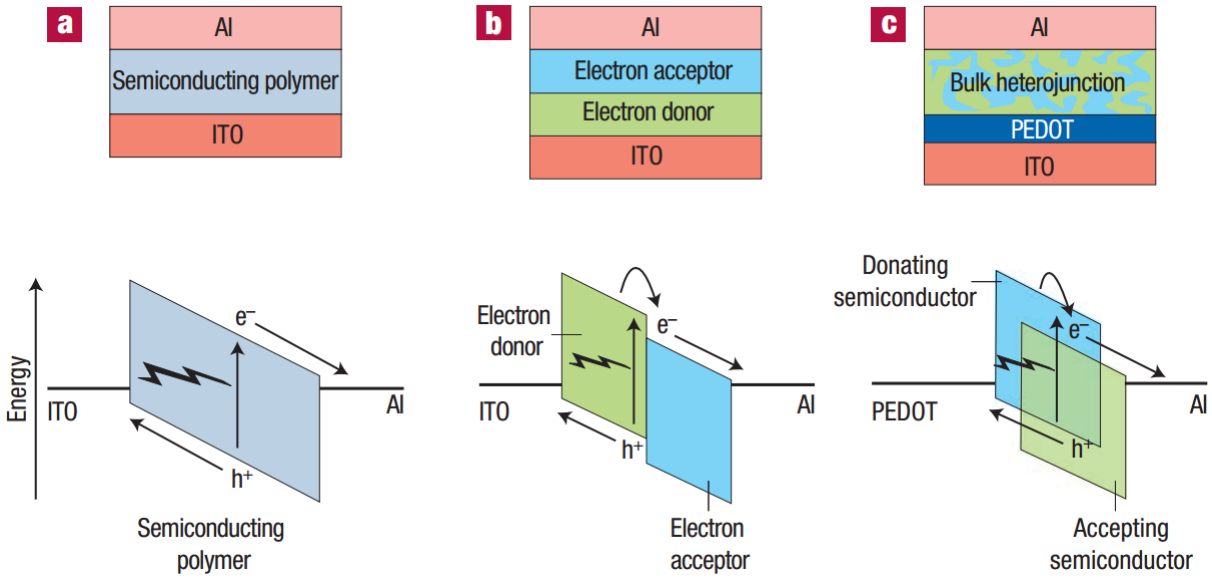

Figure 1.1 Schematic of (a) single layer homojunction; (b) bilayer heterojunction; and (c) bulk heterojunction solar cell.[7] Copyright © *Nature Materials*.

The following major milestones in OPV research have been accomplished by several groups. In 2001, N. S. Sariciftci and J. C. Hummelen obtained the first promising results of 2.5% PCE for a bulk heterojunction OPV by controlling the solubility of MDMO-PPV and PCBM in solution via distinct solvents in order to trigger different levels of phase separation in photoactive layer for efficient exciton separation.[8] In 2003, a new combination of organic binary materials consisting of P3HT and PCBM as electron donor and acceptor was proposed by N. S. Sariciftci's research group with PCE of 2.5%.[9] By 2006, Yang Yang's research group was able to produce stable efficiencies of 4% PCE repeatedly using so-called solvent annealing and thermal annealing treatments to increase the crystallinity of P3HT as well as the phase separation level between P3HT and PCBM.[10]

In the following decade, researchers quickly found that even with the optimal morphology and phase separation level for bulk heterojunction solar cell, the efficiency can still

be limited by the absorption of donor materials (e.g., P3HT is a wide-bandgap material with E_g of 1.9 eV). Therefore, by reducing the energy bandgap (E_g) of electron donor materials (e.g., polymer), we can expect broader coverage in the absorption spectrum and better utilization of solar energy. In 2007, Luping Yu's research group demonstrated a series of med-bandgap polymers with E_g ~ 1.7 eV, so called PTB series. Among them, PTB7 showed a highest efficiency of 7.5% with the absorption edge extended to 750 nm.[11] Later in 2007, R.A.J Janssen's group demonstrated a low-bandgap polymer, PDPP3P with E_g = 1.4 eV.[12] This polymer had absorption extended to 900 nm and short-current density (J_{SC}) increased up to 12 mA/cm^2 in solar-cell devices.[13] In 2014, the most efficient result for polymer bulk heterojunction solar cell was presented by Show-An Chen's group using PTB7-Th as electron donor material leading to 10.1% PCE.[14] Below, some commonly used high-performance polymers for bulk heterojunction solar cells are summarized in Figure 1.2.

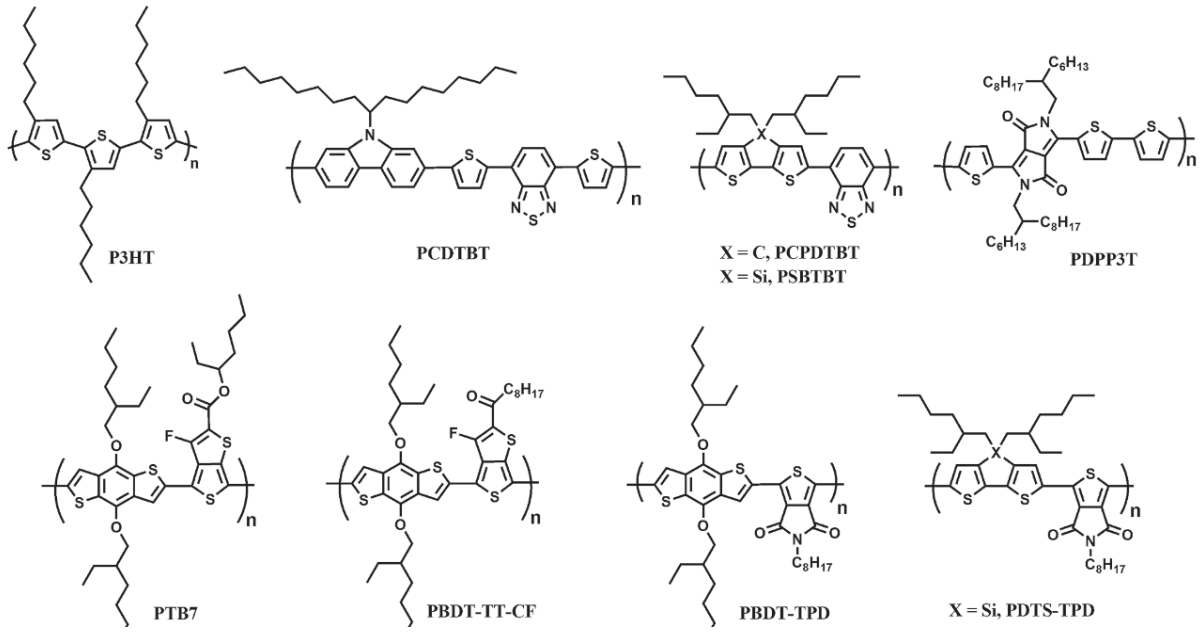

Figure 1.2 Chemical structures of some high performance polymer donor materials.[15] Copyright © *Advanced Materials*

Beginning in 2009, another new class of organic donor materials, so-called small molecules with only six to eight core units on the main chain, are selected to replace the conjugated polymer as electron donor materials in the bulk heterojunction structure of OPV. Y.S. Chen's group first demonstrated a successful small molecule OPV by solution process with 4% PCE.[16] In 2009, Alan Heeger's and Gui Bazan's group demonstrated another major breakthrough in small molecule OPV by carefully selecting the cathode interface material and reached 9% PCE.[17-19] In 2014, the most recent advance for small molecule bulk heterojunction solar cell was demonstrated by Y.S. Chen's group with a certified 9.9% PCE.[20] Below in Figure 1.3, we provide several well-known small molecules as *p*-type materials for organic solar cell devices.

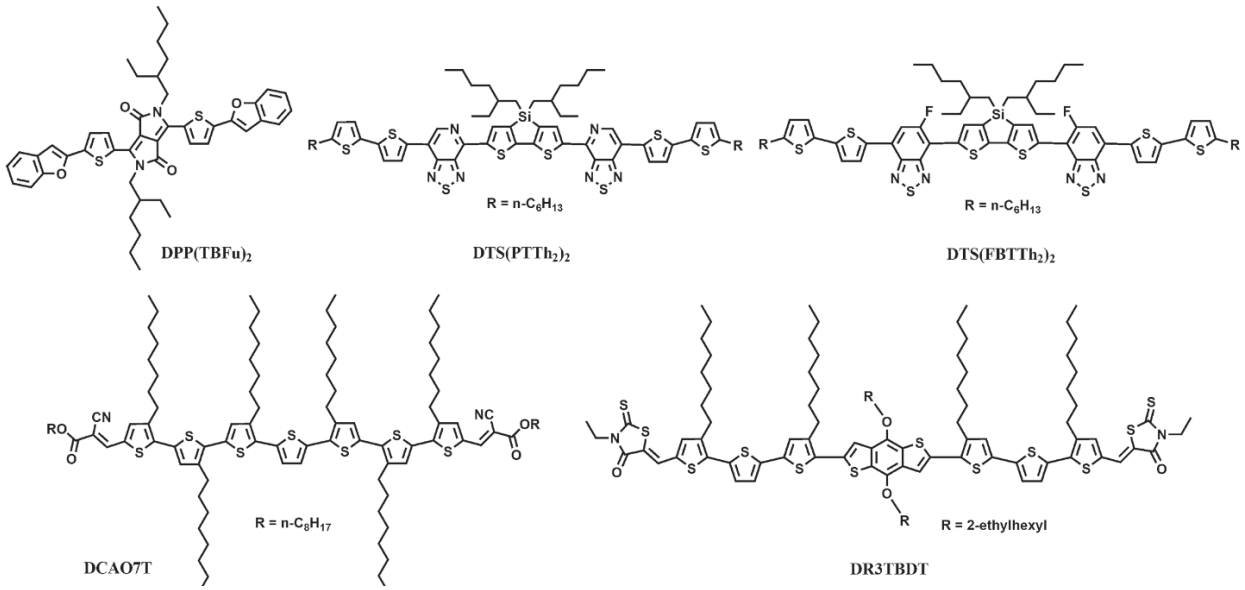

Figure 1.3 Chemical structures of some high performance small molecule donor materials.[15] Copyright © *Advanced Materials.*

1.3 Conjugated polymer

As discussed earlier, polymeric materials are blended with PCBM to form a bulk heterojunction sandwiched in between the electrodes. These polymeric materials typically belong

to the family of conjugated polymer owing to their conjugated main chain. A conjugated polymer system is generally consisting of alternating single and double bonds at its backbones forming a connected *p* orbitals with delocalized electrons. For example, in polyacetylene when a carbon atom is connected with three other atoms, three sp^2 hybridized orbitals are formed by one *2s* and two *2p* (p_x, p_y) atomic orbitals. The overlapping of hybridized sp^2 orbitals provides bonding orbital (σ) and antibonding orbital (σ^*). Single C-C bonds fill up σ-bonds first and are associated with localized electrons, whereas double C=C bonds fill up a σ-bond and a π-bond. The π- bonding (π) and antibonding (π^*) orbitals are formed by the electrons at p_z orbitals. The π- π interaction is a description for the interaction between the neighboring π bonds (for example, between the neighboring atomic rings). Figure 1.4 shows an example of a conjugated structure (double bond-single bond-double bond) in polyacetylene with the illustrations of molecular orbitals discussed above.

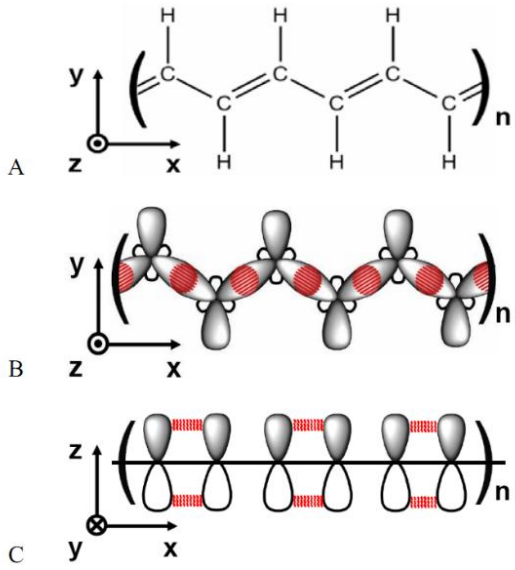

Figure 1.4 (a) Example of a conjugated polymer: polyacetylene with visualization of p_x, p_y, p_z orbitals; (b) The overlapping of sp^2 orbitals to form σ-bonds; (c) The overlapping of p_z orbitals to form π-bonds.

The energy states in conjugated polymers can be described as following: In the monomer, the π-bonding orbitals are either empty, known as lowest unoccupied molecular orbital (LUMO), or filled with electrons, known as highest occupied molecular orbital (HOMO). As monomers turn into oligomers and eventually become polymers, the π-bonding orbitals begin to split into energy levels as the overlapping of π-bonding orbitals occur and allowed energy levels begin to form continuous energy levels as many allowed energy levels get close to each other. Eventually, there is a near continuum in filled energy level and unfilled energy levels, which we often just designated as HOMO level and LUMO level of the polymers. The energy bandgap of polymer can simply be determined by the difference between HOMO and LUMO. However, more accurate optical energy bandgap corresponding to the absorption edge of polymer should be determined by the UV-Vis measurement. Figure 1.5 shows an illustration of molecular overlapping of conjugated polymer.

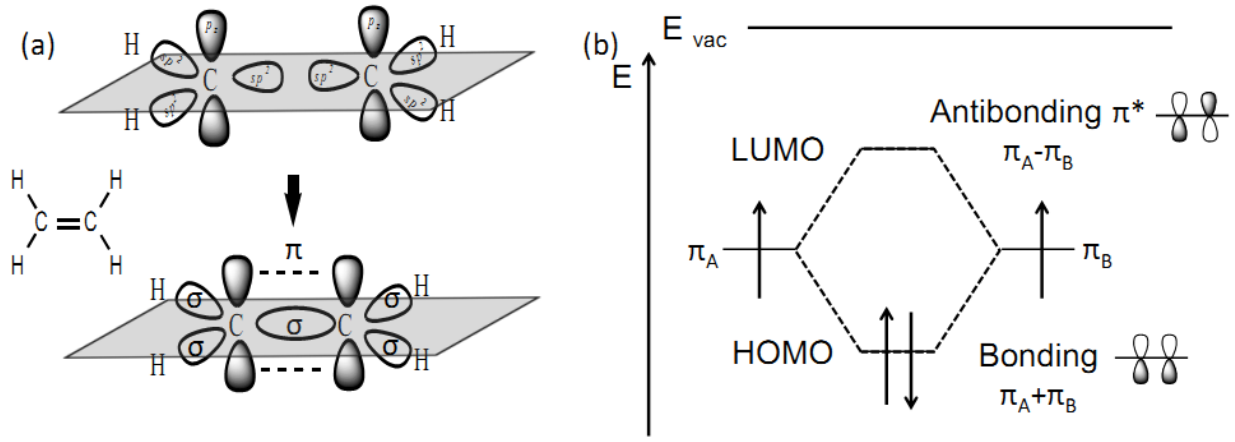

Figure 1.5 (a) Indication of σ-bonds and π-bonds formed by overlapping of molecular orbitals; (b) the splitting of energy levels due to the overlapping of molecular orbitals. The HOMO and LUMO energy levels are formed by the bonding and antibonding of these molecular orbitals.

Next, the mechanism of charge carrier transport in conjugated polymers is based on thermally assisted intermolecular hopping of highly localized charge carriers. The mobility, μ, can be written as

$$\mu(E) = \mu_0(T) e^{\left(\gamma(T)\sqrt{E}\right)}, \tag{1.1}$$

where T is the temperature, $\gamma(T)$ is field activation factor, and $\mu_0(T)$ is the mobility at zero field. Thus, μ generally increases with increasing applied electric field and temperature.

1.4 Exciton formation and charge-transfer state

Polymer solar cells, unlike traditional silicon solar cells, are not free-carrier solar cells; instead, they are excitonic solar cells. The excitons are defined as tightly bounded electron-hole pairs that require a large driving force to separate into free charge carriers. When light illuminates on a polymer solar cell, the following steps (as shown in Figure 1.6) are taken to convert photons from sun into electrons collected at electrodes:

1) Light absorption and exciton formation by electron donor materials (Fig. 1.6a)
2) Exciton migration to the donor-acceptor interface (Fig. 1.6b);
3) Exciton dissociation into free charge carriers at interface (Fig. 1.6c);
4) Charge carrier migration to the electrode (Fig. 1.6d).

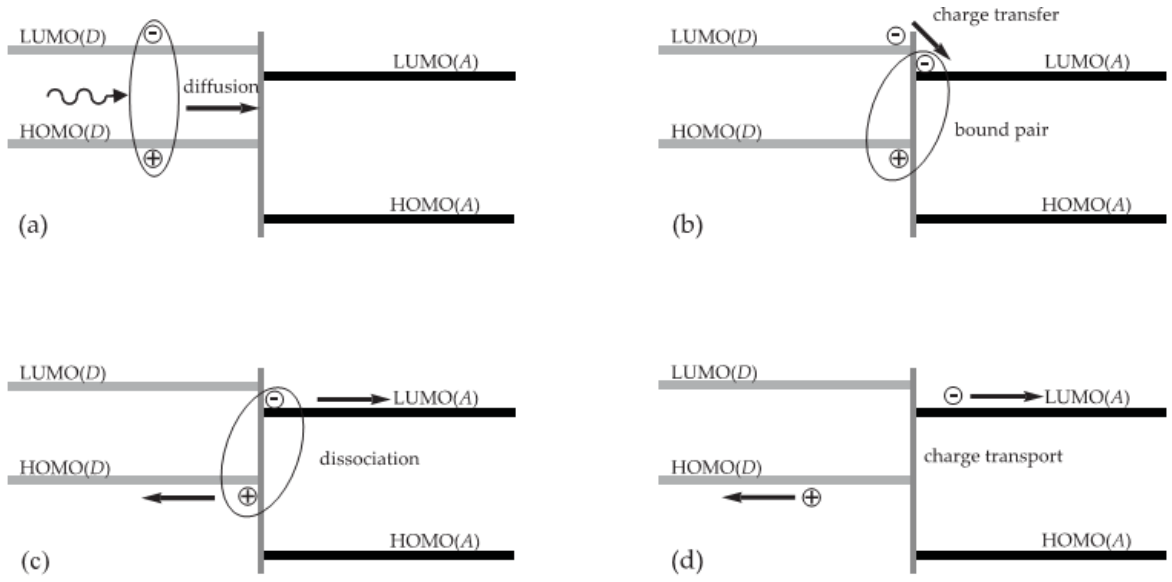

Figure 1.6 Diagrams describing the four major steps in generating electrical current inside organic solar cells.[21]

Currently, there is a debate on the exciton dissociation step. When excitons reach donor-acceptor interfaces, the electrons from donor species should transfer to the acceptor. Similarly, the hole from the acceptor species should transfer to donors. The result creates positive polarons at donors and negative polarons at acceptors. Nevertheless, since the polaron pairs are in close proximity, they could be bound by Coulomb forces, which are what we call charge-transfer states (CT states). Recent studies make several observations about the CT states:

1) The CT states are intermediate states that occur at interfaces before excitons dissociate. [22]
2) The binding energy of CT states should be less than exciton state to facilitate charge separation.[23]
3) The CT states can be formed directly by sub-gap absorption.[24]
4) Both above gap and below gap absorption can form CT states.[25]
5) The CT states are delocalized with lifetime longer than exciton.[26]

The CT below gap absorption can be categorized into several kinds, as shown in Figure 1.7. All these can be characterized by EQE measurement.

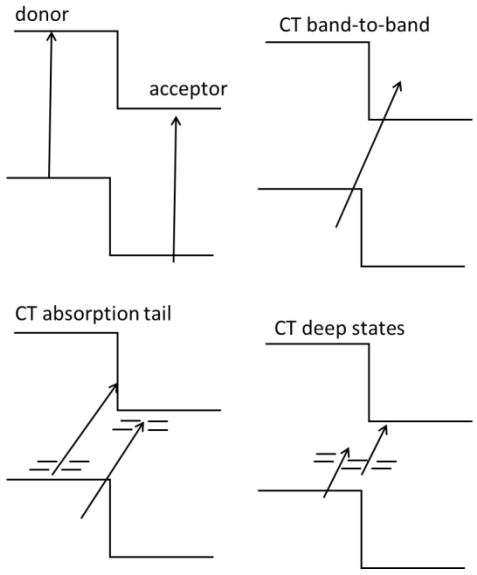

Figure 1.7 Diagrams describing the sub-gap absorption due to CT states: CT band-to-band, CT absorption tail, and CT deep states.[27]

1.5 External quantum efficiency and charge recombination

External quantum efficiency (EQE) is an important parameter in representing solar cell performance related to its light absorption capability. External quantum efficiency represents the actual percentage of photons that are converted to the hole-electron pairs and collected by the external circuit at a given wavelength, λ. It is a ratio between collected charge carriers and incident photons and can be expressed as

$$EQE(\lambda) = \frac{\text{Number of electrons collected at } \lambda}{\text{Amount of incident photons at } \lambda} \quad . \tag{1.2}$$

The external quantum efficiency can also be represented in terms of the efficiency of the four steps of photocurrent generation aforementioned.

$$\eta_{EQE} = \eta_A \eta_{ED} \eta_{CS} \eta_{CC} , \quad (1.3)$$

where η_A is absorption efficiency, η_{ED} is exciton diffusion efficiency, η_{CS} is the charge separation efficiency, and η_{CC} is the charge collection efficiency. Upon the utilization of bulk heterojunction structures for polymer solar cells, the exciton migration and dissociation are believed to be relatively efficient, compared to light absorption and charge migration efficiency. Further discussion on the limitations of single-junction polymer solar cell will be carried out in the next chapter.

Unfortunately, during the process of generating electrical current, charge recombination process also exists and competes with charge generation process. The two major recombination regimes (Figure 1.8) are shown as follows:

1) Geminate recombination where bound electron-hole pairs (or excitons) recombine before dissociation (Fig. 1.8e);
2) Biomolecular recombination where free charge carriers recombine after dissociation (Fig. 1.8f).

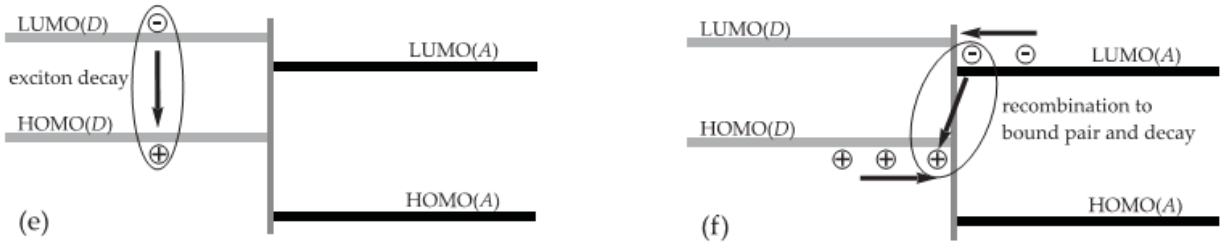

Figure 1.8 Diagrams describing the two major steps in charge recombination.[21]

The biomolecular recombination can be quantified by the Langevin recombination model, where the recombination rate, R is the product of proportionality factor, γ and carrier density of electron, n and hole, p.

$$R = \gamma np \tag{1.4}$$

The proportionality factor γ can be further expressed in terms of mobility, μ

$$\gamma = \frac{q(\mu_e + \mu_e)}{\varepsilon_0 \varepsilon_r}, \tag{1.5}$$

where ε_0 and ε_r are vacuum permittivity and dielectric constant of the material, respectively. Therefore, when density of charge carriers increases, the recombination increases accordingly.

1.6 p-n Junction & equivalent circuit

The current-voltage behavior of a solar cell can be described by the electrical behavior in a PN junction, as shown in Figure 1.9. Upon applying the electric field, E, the contact region between p-type and n-type semiconductor is quickly depleted of free charge carriers, hereafter known as the depletion region. An internal field, known as the built-in potential V_{bi}, is formed within the depletion region. When a solar cell is in the dark state, its current-voltage behavior follows the current voltage behavior like an ideal p-n junction, which is

$$J_{dark} = J_o\left(e^{V/V_T} - 1\right), \tag{1.6}$$

where J_{dark} is the current density in the dark state, V is the voltage, J_o is the saturation current density, and V_T is thermal voltage. The V_T is given by $V_T = nkT/q \simeq 0.026V$, where k is Boltzmann's constant, q is electronic charge, and n is the ideal factor of the diode. Upon solar

illumination, extra charge carriers are generated within p-n junction breaking the original balance. A new term, J_{ph} representing the photocurrent density is added to reflect the new current-voltage relationship in the p-n junction as

$$J(V) = J_{dark} - J_{ph} = J_o\left(e^{V/V_T} - 1\right) - J_{ph}. \tag{1.7}$$

As shown in Figure 1.9, a typical current-voltage curve for solar cell should reside in the fourth quadrant. When the applied voltage is equal to zero ($V = 0$), current output is the greatest and equal to the photocurrent density alone. This particular term is also known as short-circuit current density, J_{SC}.

$$J(V = 0) = J_{ph} = J_{sc} \tag{1.8}$$

In Figure 1.9, it is the intersection point between the current-voltage curve and the y-axis. On the other hand, by setting the current density equal to zero (J = 0), we can obtain a voltage value, which can be expressed as

$$V(J = 0) = V_T \ln\left(1 + \frac{J_{sc}}{J_o}\right) \cong V_T \ln\left(\frac{J_{sc}}{J_o}\right) = V_{oc}. \tag{1.9}$$

This voltage is also known as the open-circuit voltage, V_{OC}, which typically is the intersection point between current-voltage curve and x-axis. The power output given by a solar cell is defined as the product of current and voltage at a given point, which is equal to

$$P(V) \equiv J \times V = J_o V\left(e^{V/V_T} - 1\right) - J_{sc} V. \tag{1.10}$$

The power conversion efficiency, defined by the ratio between the maximum power output by solar cell and incident light power received by solar cell is written as

$$\eta \equiv \frac{P_{\max}}{P_{incident}} \times 100\% \quad . \tag{1.11}$$

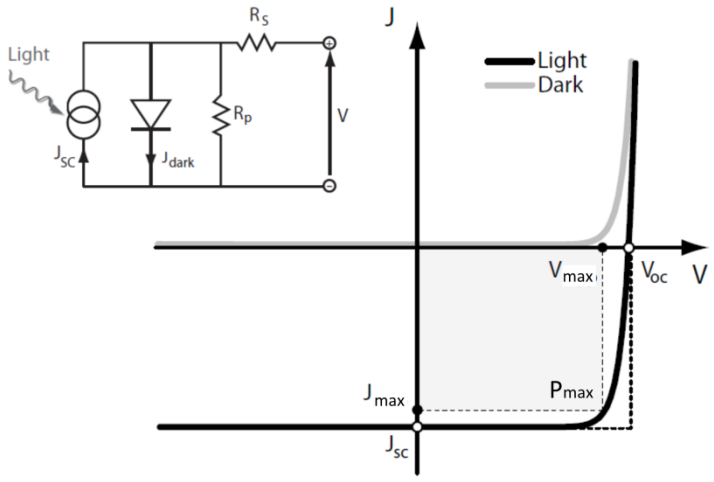

Figure 1.9 The current density-voltage (*J*-*V*) curve for solar cell under illumination with the equivalent circuit showing in the upper left corner.

From Figure 1.9, there are two different rectangles in the fourth quadrant. The larger rectangle, given by the product of J_{SC} and V_{OC}, is the ideal maximum power achievable by the solar cell. The smaller rectangle given by the product of J_{max} (real maximum current output during the operation) and V_{max} (real maximum voltage output during the operation) is the real maximum power output, P_{max}, given by solar cell. Here, we can represent P_{max} in terms of J_{SC} and V_{OC},

$$P_{\max} = J_{\max} \cdot V_{\max} = J_{SC} \cdot V_{OC} \cdot FF \quad . \tag{1.12}$$

A new ratio factor, fill factor (*FF*), defined by the ratio between the maximum output power and the ideal maximum output power is given. *FF* can be seen as the measure of quality of the *J-V* curve measured for the solar cell upon illumination. The power conversion efficiency can therefore be rewritten in terms of *FF*,

$$\eta = \frac{J_{SC} \cdot V_{OC} \cdot FF}{P_{incident}} \times 100\% \quad (1.13)$$

.

The typical incident light intensity from solar simulator is 1000 W/m^2 or 100 mW/cm^2. Furthermore, the summation of the EQE response can also be used to calculate the maximum photocurrent density, which is given as

$$J_{SC} = \int_{\lambda} \frac{hc}{q\lambda} \cdot EQE(\lambda) \cdot I_o(\lambda) \cdot d\lambda \quad (1.14)$$

,

in which λ is the wavelength in nanometer scale, I_o is the intensity of incident light (mW/cm^2).

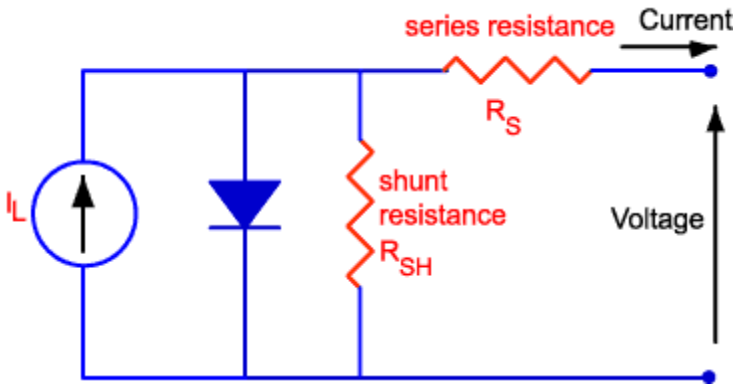

Figure 1.10 The equivalent circuit of a solar cell.

Figure 1.10 is an approximate equivalent circuit used to describe a conventional solar cell. The solar cell is basically a diode connected with a current source in parallel. The parasitic resistors (R_s and R_{sh}) are also incorporated into the equivalent circuit to represent the different parasitic effects inside the solar cell. When current flows through these resistors, partial power is dissipated by $P = V^2/R$ thus reducing the total power output of the solar cells. To account the shunt resistance effect on photocurrent, we can rewrite photocurrent equation as

$$J(V) = J_{dark} - J_{ph} + J_{shunt} = J_o\left(e^{V/V_T} - 1\right) - J_{ph} + \frac{V + J_{SC}R_s}{R_{shunt}} \quad . \tag{1.15}$$

Furthermore, the approximate value of series resistance R_s and shunt resistance R_{sh} can also be extracted from *J-V* curve. Under ideal solar cell conditions, R_s should be as small as possible while R_{sh} should be as close to infinity as possible. In that case, $J_{\max} \times V_{\max} = J_{sc} \times V_{oc}$. On the *J-V* curve, the series resistance (R_s) can be extrapolated from the slope of the *J-V* curve at the open-circuit voltage point, whereas the shunt resistance (R_{sh}) can be extrapolated from the slope of the *J-V* curve at short-circuit current point, as shown in Figure 1.11.

$$\left.\frac{dV}{dJ}\right|_{J=0} = R_s + \frac{R_{sh}}{1 + \left[\frac{J_o R_{sh}}{V_T} e^{(V_{oc}/V_T)}\right]} \cong R_s \tag{1.16}$$

$$\left.\frac{dV}{dJ}\right|_{V=0} = R_s + \frac{R_{sh}}{1 + \left[\frac{J_o R_{sh}}{V_T} e^{(-J_{sc}R_s/V_T)}\right]} \cong R_s + R_{sh} \cong R_{sh} \tag{1.17}$$

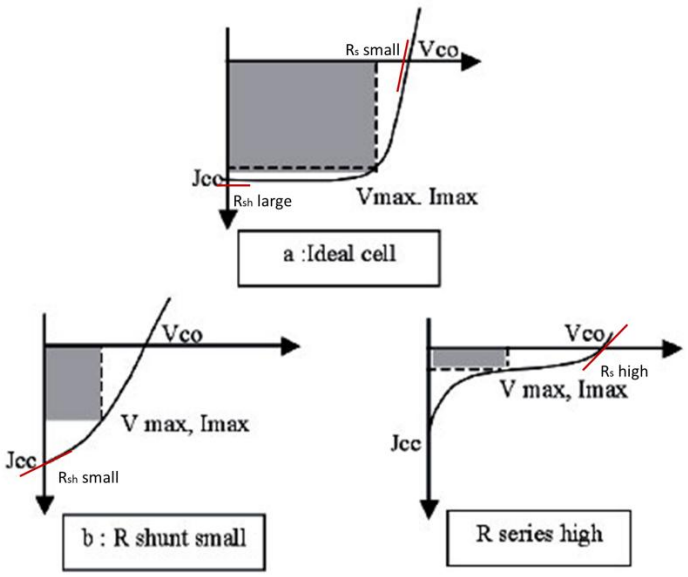

Figure 1.11 The series resistance, R_s and shunt resistance, R_{sh} can be extracted from *J-V* curve.[28]

Chapter 2 Design improvement: Multi-Junction Solar Cells

2.1 Loss mechanism in single-junction solar cells

In 1961, Shockley and Queisser developed a mathematical prediction of the efficiency limitation of solar cell given the thermodynamically limitation of a direct bandgap semiconductor used as perfect solar cell absorber.[29] Following this prediction, there are two main sources of energy loss in single-junction solar cells:

1) Transmission loss: the complete loss of photon energy when the energy of the photon is smaller than the energy bandgap of semiconductor. The low-energy photons are not absorbed;
2) Thermalization loss: the partial loss of photon energy due to hot carriers. When the energy of photon is greater than the energy bandgap of semiconductor, the excess energy above the bangap of the semiconductor is not being used for the power conversion and is usually dissipated as thermal energy, which is so-called thermalization loss.

As a result, the predicated maximum attainable efficiency for single-junction solar is 33.5% with a semiconductor energy bandgap of 1.4 eV.[29]

Another way to examine the maximum attainable efficiency can be done from the efficiency parameters, J_{SC}, V_{OC}, and *FF*, from *J-V* measurements. Ideally, by simultaneously enlarging all three parameters at once, one should be able to achieve the theoretically limitation in efficiency for single-junction solar cells. However, that is not possible, because there is a tradeoff between J_{SC} and V_{OC} when designing the energy bandgap of semiconductors. This relationship can be presented as follows. In general, E_g is inversely correlated to J_{SC}.

$$\eta(E_g) = J_{SC}(E_g) \cdot V_{OC}(E_g) \cdot FF$$
$$E_g \uparrow \Rightarrow V_{OC} \uparrow, J_{SC} \downarrow \quad (2.1)$$
$$E_g \downarrow \Rightarrow V_{OC} \downarrow, J_{SC} \uparrow$$

First, the maximum charge extraction potential at V_{OC} is given by the bandgap of the semiconductor, such as

$$V_{OC}(E_g) = \frac{E_g}{q} - \frac{kT}{q}\ln(\frac{N_{eff}^2}{np}) \ , \quad (2.2)$$

where E_g is the effective bandgap, N_{eff} is the effective density of states, and n, p are electron and hole concentrations. In other words, the high steady state carrier concentrations and low charge carrier recombination are the keys to get V_{OC} close to the effective bandgap. Second, the J_{SC} can be represented in terms of E_g as well, such as

$$J_{SC}(E_g) = q\int_{E_i}^{E_g} N_{ph}(E) \times EQE(E) \times dE \quad (2.3)$$

,

where N_{ph} is the photon density of state ($s^{-1}m^{-2}J^{-1}$), and EQE is the quantum efficiency. So, when reducing the bandgap of semiconductor to increase the coverage of solar spectrum, although J_{SC} should increase accordingly, V_{OC} would decrease due to the effective bandgap of the materials being reduced. Thus, an optimal balance between J_{SC} and V_{OC} has to be achieved in order to obtain maximum efficiency. Nevertheless, all the discussions above are based on the assumption that mobility is infinite and non-radioactive recombinations do not exist in the solar cell. If we take mobility and non-radioactive recombination into consideration, a lower theoretical efficiency was found for crystalline silicon solar cells of 29.4%. [30]

2.2 The special case of organic solar cells

Organic solar cells, on the other hand, would have much lower attainable maximum efficiency due to their relatively low carrier mobility (10^{-4} cm^2/Vs to 10^{-2} cm^2/Vs for holes and 10^{-3} cm^2/Vs to 10^{-1} cm^2/Vs for electrons) and strong bonding forces for excited electron-hole pairs (excitons).[31] The low carrier mobility mainly limits the thickness of the photoactive layer in organic solar cell devices.[32] The electron drift distance, L must be larger than the thickness of the photoactive layer, d, to avoid the device recombination (Figure 2.1). The drift length can be expressed as

$$L = \mu\tau E > d \quad , \tag{2.4}$$

where μ is charge mobility, τ is carrier lifetime, and E is electric field. With limited thickness, the optical absorption of organic photoactive layer sometimes is not sufficient enough to capture all the incident photons.

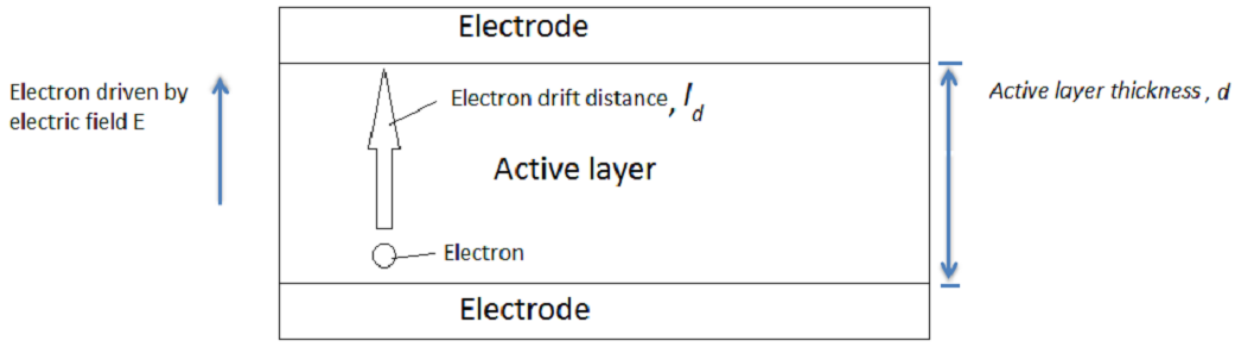

Figure 2.1 Illustration of organic solar cell with thickness limitation due to electron drift distance.

The diffusion length can also be expressed in terms of diffusivity, D and carrier lifetime τ.

$$L = \sqrt{D\tau} \quad . \tag{2.5}$$

The diffusivity can be further expressed in terms of mobility μ

$$D = \mu \frac{kT}{q} \quad (2.6)$$

The J_{SC} can be expressed in terms of diffusion length for electron, L_n and hole, L_p

$$J_{SC} = qG(L_n + L_p) \quad (2.7)$$

where G is the exciton generation rate. Thus, organic photoactive layer with low mobility would lead to low carrier diffusion length, and eventually limit the thickness that can be applied to organic solar cell devices. The conventional thickness for organic solar cell can be ranged from 100 to 200 nm.[33] In some particular case of polymers (e.g., P3HT) with high crystallinity and optimized morphology with PCBM, the thickness tolerance for the organic photoactive layer can extend to 500 nm.[34] [35, 36]

The large exciton binding energy, on the other hand, can cause potential loss in V_{OC}. The binding energy of exciton can be described as

$$E_{exciton-binding} = \frac{2m_{reduce}e^4}{(4\varepsilon\varepsilon_0)^2 h^2} \quad (2.8)$$

where m_{reduce} is the reduced mass of the exciton, ε is the dielectric permittivity, and ε_0 is the permittivity in free space. Since organic semiconductors typically have low ε (2~4), the exciton binding energy are usually found around 0.3 to 0.7 eV, which is far more than the thermal energy at the room temperature.

The origin of V_{OC} for organic solar cells is still not fully understood.[37] Generally, the origin of V_{OC} in solar cell is the result of quasi-Fermi levels, E_f, splitting at the donor (*p*-junction) and acceptor (*n*-junction) molecule in zero current, under light illumination. Assuming there is no potential loss across the donor and acceptor junction, V_{OC} can be express as follows

$$V_{oc} = \frac{1}{q}(E_{\text{HOMO of donor}} - E_{\text{LUMO of acceptor}} - kT\ln(\frac{N_L N_H}{np})), \tag{2.9}$$

where N_L, N_H are the density of states of the LUMO of the acceptor and the density of states of the HOMO of the donor, and *n*, *p* are carrier densities of electrons and holes. From this equation, the V_{OC} loss depends on the density of free charge carriers at quasi-Fermi levels states. Therefore, when low work function interfacial materials (e.g., calcium) or surface dipole layer (e.g., PFN) are applied to the cathode, an increment in V_{OC} is observed.[38] The enhancement of V_{OC} due to interfacial modification can be ascribed to a more balanced electron and hole charge transport and reduced recombination, leading to higher carrier concentration of *n*, *p* inside the solar cell device. Thus, from equation above, V_{OC} would increase with the higher *n*, *p*.[39]

Since in organic heterojunctions, there is no depletion region formed at the contacts between *p*-type and *n*-type materials, we usually draw flat band energy levels of donor and acceptor, as shown in Figure 2.2a.

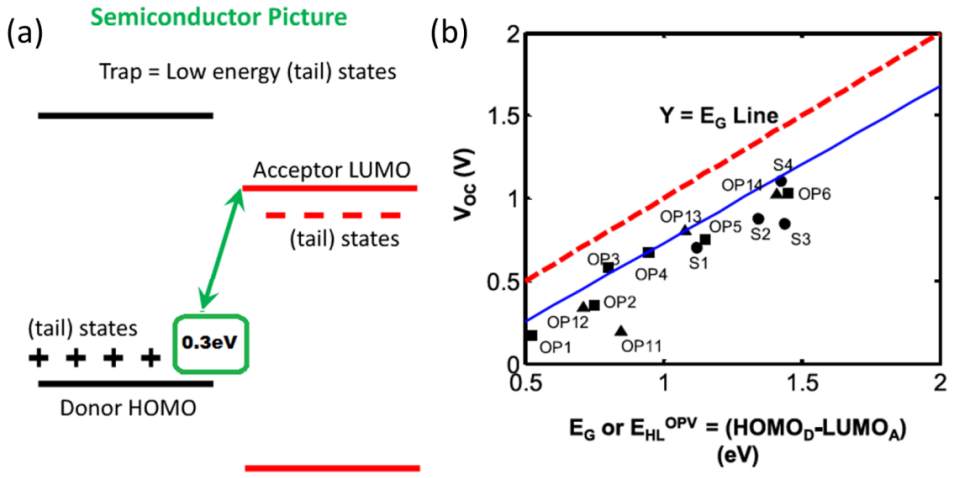

Figure 2.2 (a) The energy level diagram of organic solar cell, where V_{OC} is determined by the LUMO of acceptor and HOMO of donor; (b) A demonstration of the linear relationship between V_{OC} and $HOMO_{donor}$-$LUMO_{acceptor}$.[40]

Assuming interfacial contacts with electrodes are ohmic, the maximum V_{OC} depends on the offset between the donor molecule's HOMO level and the acceptor molecule's LUMO level.[41] A linear relationship can be demonstrated in Figure 2.2b.

$$V_{oc} = \frac{1}{q}(E_{\text{HOMO of donor}} - E_{\text{LUMO of acceptor}} - 0.3eV). \tag{2.10}$$

The 0.3 eV in the equation above is the potential loss due to the exciton binding energy that must be overcome in order to obtain the photovoltage. When interfacial contacts are not ohmic, V_{OC} tends to approach the difference between the work functions of the electrodes.[42]

$$V_{oc} = \frac{1}{q}(E_{\text{cathode}} - E_{\text{anode}}). \tag{2.11}$$

Next, Figure 2.3a represents another way to explore the origin of V_{OC}. Previously, upon light excitation, "excitonic donors" are expected to form and diffuse to the interface where

ultrafast dissociation of the excitons is taken place. Recent studies by different optical spectroscopy methods showed that there could be an intermediate state called the charge-transfer states (CT states) formed at the interface, as previously discussed. One consequence of formation of CT states is that the transition of electron would start from excitonic states higher than the HOMO level of the donor to excitonic state lower than the LUMO level of the acceptor (also known as sub gap absorption).[43] V_{OC} therefore should be correlated with the CT states directly, such as

$$V_{oc} = \frac{1}{q}(E_{\text{CT ground state}} - E_{\text{CT excited state}}). \tag{2.12}$$

From Figure 2.3b, we can see a strong linear relationship between the energy level of CT states and the V_{OC} of organic solar cells. Thus, by enlarging the CT states difference and avoiding the deep CT trap states in the middle of the bandgap, V_{OC} can be maximized. The detailed CT state characterizations can be done by EQE measurement with emphasize on sub-gap absorption.

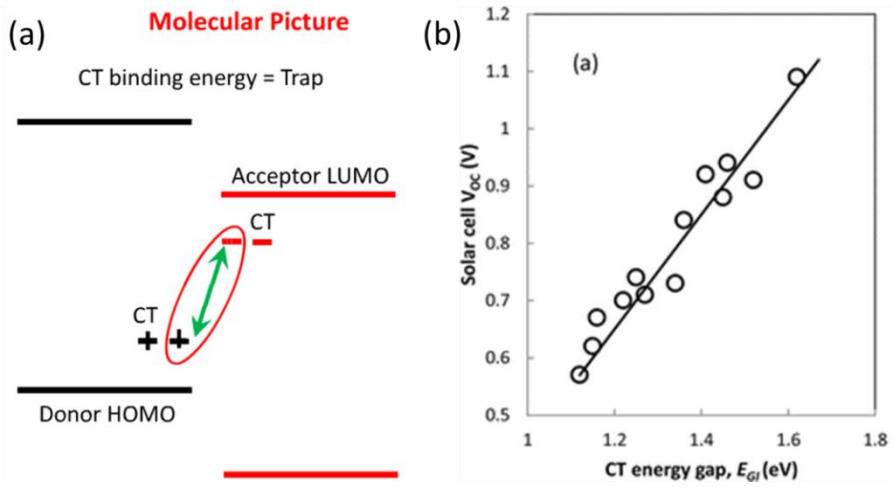

Figure 2.3 (a) The energy level diagram of organic solar cells where V_{OC} is determined by the CT states; (b) a demonstration of the linear relationship between V_{OC} and CT states. [27]

Below, T. Mueller et al. have performed a simulation of the maximum attainable efficiency for single-junction organic solar cell (Figure 2.4) based on two factors:

1) The quasi-Fermi level splitting loss (e.g., exciton binding energy) (y-axis);
2) The energy level difference of $E_{\text{HOMO, donor}} - E_{\text{LUMO, acceptor}}$ (x-axis).

The simulated results are given as follows.

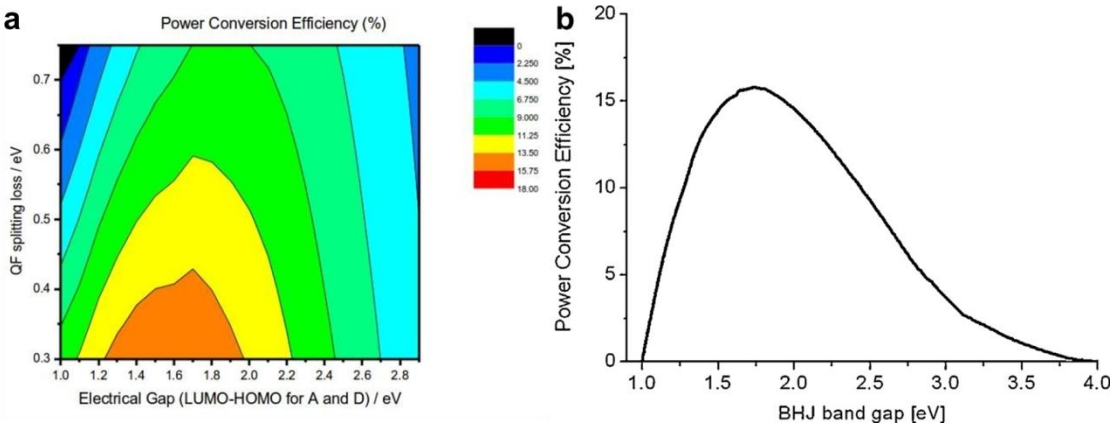

Figure 2.4 The calculated maximum efficiency of single-junction organic solar cells.[44]

The maximum efficiency is about 15% for single-junction organic solar cells, assuming *FF* is 60% and EQE is 60% across the whole absorption spectrum. Assuming that the exciton binding energy is around 0.4 eV, the optimized energy bandgap for organic materials is approximately 1.6 eV. Compared with crystalline silicon solar cell with maximum attainable single-junction efficiencies of 29.4%, organic solar cells with 15% maximum attainable efficiency in single junctions are still quite inefficient.

2.3 Design rules for tandem solar cells

As previously discussed, the maximum attainable efficiency for single-junction solar cells is approximately 31%. The major losses of photon energy are due to thermalization loss (such as loss of high-energy photons) and limited absorption in the long wavelength (such as loss of low-energy photons). In order to overcome this problem, a device structure, the so-called tandem cell, is utilized.

In a tandem-structure solar cell, multiple absorbers with differentiated energy bandgaps are applied to absorb a portion of solar spectrum selectively.[45] From the Figure 2.5 below, Graztel et al. used different colors to represent different absorbers used in tandem solar cells and predicated the theoretical efficiency of multi-junction tandem solar cells based on above-mentioned Shockley and Queisser theory. For example, in double-junction tandem solar cells, one wide-bandgap material with absorption up to 800 nm is combined with one low-bandgap material with absorption mainly from 800 nm to 1200 nm. In that way, the theoretical efficiency is improved from 31% (single-junction) to 42% (double-junction). Similarly for triple-junction solar cells, when three absorbers with cascaded energy bandgaps are applied, the theoretical efficiency improves to 49%. Given an infinite number of junctions with differentiated energy bandgaps, the efficiency limit, in principle, can go up to 68%.[28]

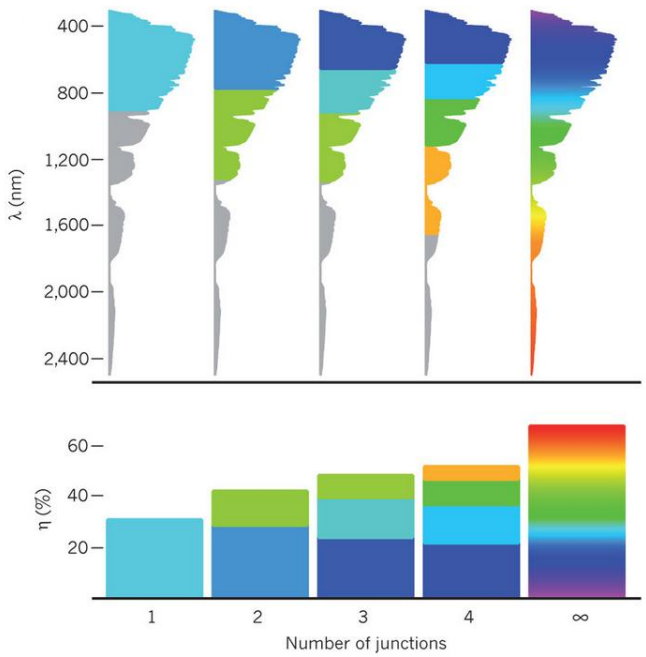

Figure 2.5 The calculated tandem solar cell efficiency depending on the number of subcells.[28] Figure adapted from *Nature*. Copyright © *Nature*.

The design of inorganic tandem solar cells is usually based on III-V semiconductors, such as Ge, GaAs, GaInP, and etc., due to their easily tunable energy bandgaps. The most common forms of tandem structure solar cells are realized through stacking two or three absorbers in one functional device, namely double-junction and triple-junction tandem solar cells. When stacking multiple absorbers in double-junction and triple-junction tandem structures, the order of absorbers is usually as follows. The wide-bandgap absorbers should be placed close to the electrical contact when the light enters, such that the high-energy photons will be absorbed first, leaving low energy photons for low-bandgap absorbers to harvest. Thus, thermalization loss of high-energy carrier is reduced.

Figure 2.6 provides an example of triple-junction tandem solar cell from III-V semiconductors explaining the arrangement of absorbers.[46] The top subcell (GaInP) with the

largest bandgap is placed at the top to absorb the high-energy photons first. The less energetic photons pass through and encounter the middle subcell (GaAs or InGaAs) where more of the photons are absorbed. Last, the remaining low-energy photon energy from the long wavelengths would be utilized by the bottom subcell (Ge) with the smallest energy bandgap of the three absorbers. As a result, the total absorption of the triple-junction solar cell can cover almost the full solar spectrum.

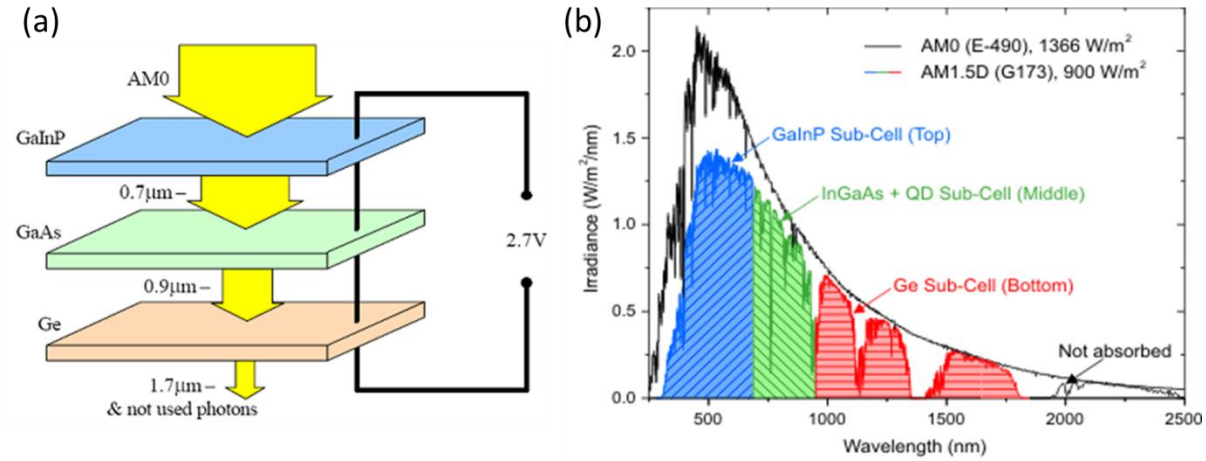

Figure 2.6 (a) The arrangement of the absorbers in triple-junction solar cells; (b) the absorption spectrum of subcells in the triple-junction solar cell.

The monolithic tandem structures typically connect the subcells in series, which means that V_{OC} and J_{SC} of tandem solar cells are determined by the subcells' outputting V_{OC} and J_{SC} through the following relationships:

$$\begin{aligned} V_{\text{OC, tandem}} &= V_{\text{OC, top}} + V_{\text{OC, middle}} + V_{\text{OC, bottom}}, \\ J_{\text{SC, tandem}} &= \min(J_{\text{SC, top}}, J_{\text{SC, middle}}, J_{\text{SC, bottom}}). \end{aligned} \tag{2.13}$$

The potential of tandem solar cells is the sum of potential of the subcells. On the other hand, following Kirchoff's law of series connection, the current density of tandem solar cells is limited by the smallest current output from the subcells. A typical *J-V* curve of tandem solar cell is shown in Figure 2.7b.

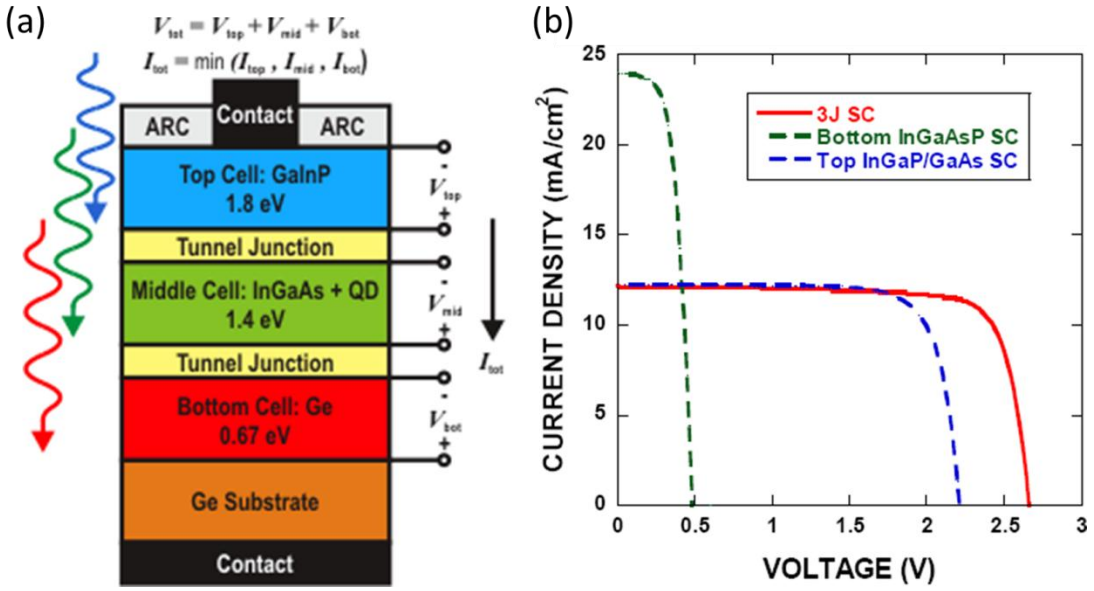

Figure 2.7 (a) A device schematic for triple-junction III-V tandem solar cell; (b) the typical *J-V* curve of triple-junction tandem solar cell.[47]

One of the important factors to be considered in tandem solar cell design is current matching.[48] Following the discussion above, the optimized design of tandem solar cell will require maximum achievable photocurrent from different subcells. Therefore, designing each subcell to produce equal amounts of photocurrent prevents extra photocurrent from turning into leakage current in tandem cells. Typically, several design rules have to be considered as follows:

1) The arrangement of absorbers should follow our earlier discussion, in which $E_{g,top} > E_{g,middle} > E_{g,bottom}$;

2) The difference in energy bandgap among different absorbers should be large enough to avoid absorption spectrum overlap.

In Figure 2.7b, the *J-V* curves of the tandem solar cell and the subcells used in the tandem cells are provided. The tandem solar cell has reduced current density as compared to the subcells in the tandem. Nevertheless, this loss of J_{SC} can be compensated by the increase of V_{OC}, so overall efficiency can be improved. The current best combination of bandgaps for triple-junction tandem solar cells is based on GaInP, (In)GaAs, and Ge, with cascaded bandgaps of 1.8 eV, 1.4 eV, and 0.67 eV. The resulting device performance based on InGaP/GaAs/InGaAs can achieve an averaged efficiency of 37.7 ± 1.2%.[49]

2.4 Efficiency calculation for organic tandem solar cells

In the case of organic tandem solar cells, the efficiency calculation can be carried out as aforementioned. In Figure 2.8, T. Mueller et al. used the same assumption of 60% EQE and 60% FF for each subcell absorber in the tandem structure for simulation.[50] The theoretical calculation for the maximum attainable efficiency of double-junction organic solar cells could be simulated based on 1) the energy bandgap of first cell as x-axis and 2) the energy bandgap of second cell as y-axis.

As result, the maximum efficiency of 22% is found using two organic absorbers as subcells in double-junction tandem structures.[50] In order to reach optimal efficiency, matched photocurrent output from different subcells is required. Several optimized energy bandgap selection for double-junction tandem solar cells are provided in Table 2.1.[51] Compared to the single-junction theoretical efficiency of 15%, the double-junction tandem cell certainly shows a more promising efficiency predication of 22% under the same EQE and FF assumption.

Table 2.1 Calculated efficiencies based on different front and back subcell energy bandgaps.

First cell (E_g / nm)	Second cell (E_g / nm)	Calculated Efficiency
1.9 eV (770 nm)	1.25 eV (1300 nm)	21%
2.1 eV (690 nm)	1.5 eV (1030 nm)	20%
2.2 eV (645 nm)	1.7 eV (890 nm)	19%

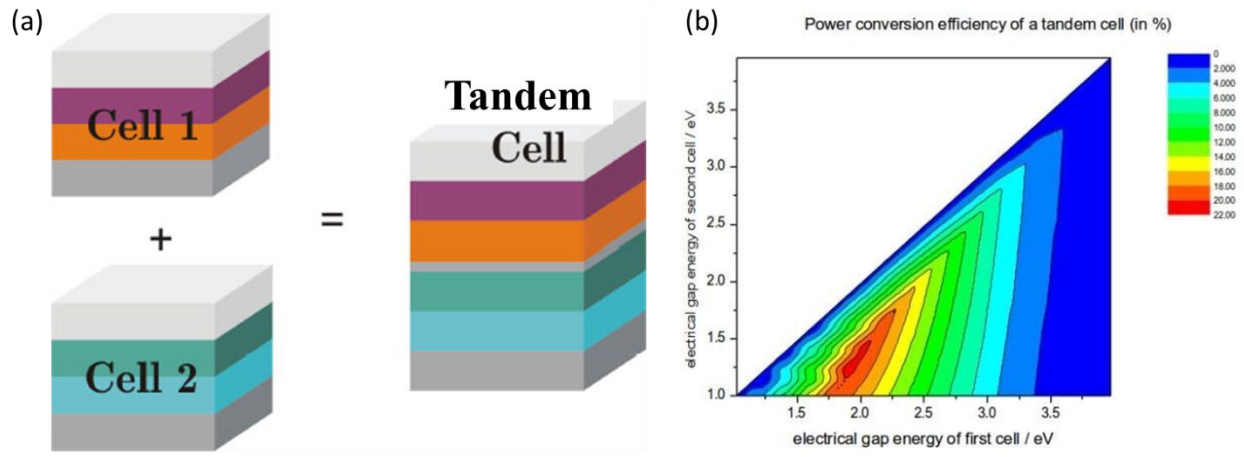

Figure 2.8 (a) The tandem solar cell is based on two subcells connected in series; (b) The calculated maximum efficiency of organic tandem solar cells depends on the different combination of energy bandgaps of first and second subcells.[50]

2.5 Design of interconnecting layers

In the tandem structure for solar cell, there are two ways to construct interconnections between the subcells, as shown in Figure 2.9. Four-terminal tandem devices use external electrical wires to connect the subcells, whereas two-terminal tandem devices stack the subcells in one device via an interconnecting layer. In general, two-terminal tandem cells present more challenges in device design and fabrication. Nevertheless, two-terminal tandem can provide

better system integration with other electrical components in one device. Thus, hereafter we will focus only on two-terminal tandems.

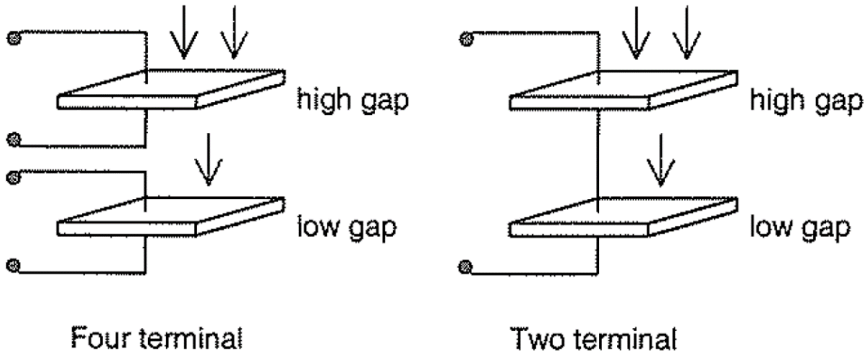

Figure 2.9 Tandem solar cells connected by two terminals and four terminals.

In monolithically integrated tandem cells, the two cells are series-connected by interconnecting layers (ICL). The interconnecting layers are the interfacial layers sandwiched in between the two subcells. The first organic tandem solar cell was demonstrated in 1990 by Hiramoto et al., as shown in Figure 2.10a.[52] This tandem device was consisted of two subcells connected by a thin metallic layer of gold. Figure 2.10b shows the similar tandem designs using a thin metal interconnecting layer which was realized by Forrest el al. in 2002.[53] The single metallic layer, because it is very thin, is highly transparent and at the same time highly conductive for both electron and hole transport. Thus, when charge carriers migrate to the ICL at the center (Figure 2.10c), the recombination of opposite charges can take place. Canceling out of excess charge carriers with opposite charges from different subcells is critical in maintaining charge neutrality inside the tandem. At the current matched state, the recombination of excess charges is complete. Under this situation, the quasi-Fermi levels of the front subcell will align with the quasi-Fermi level of the back subcell, resulting in a shift of vacuum levels (Figure

2.10d). Thus, the V_{OC} is the sum of V_{OC} of the subcells. Under unfavorable conditions in which current is not matched from different subcells, the charge carriers not canceled out at the ICL can flow into other subcells, which is known as leakage current, and can cause severe device performance degradation.

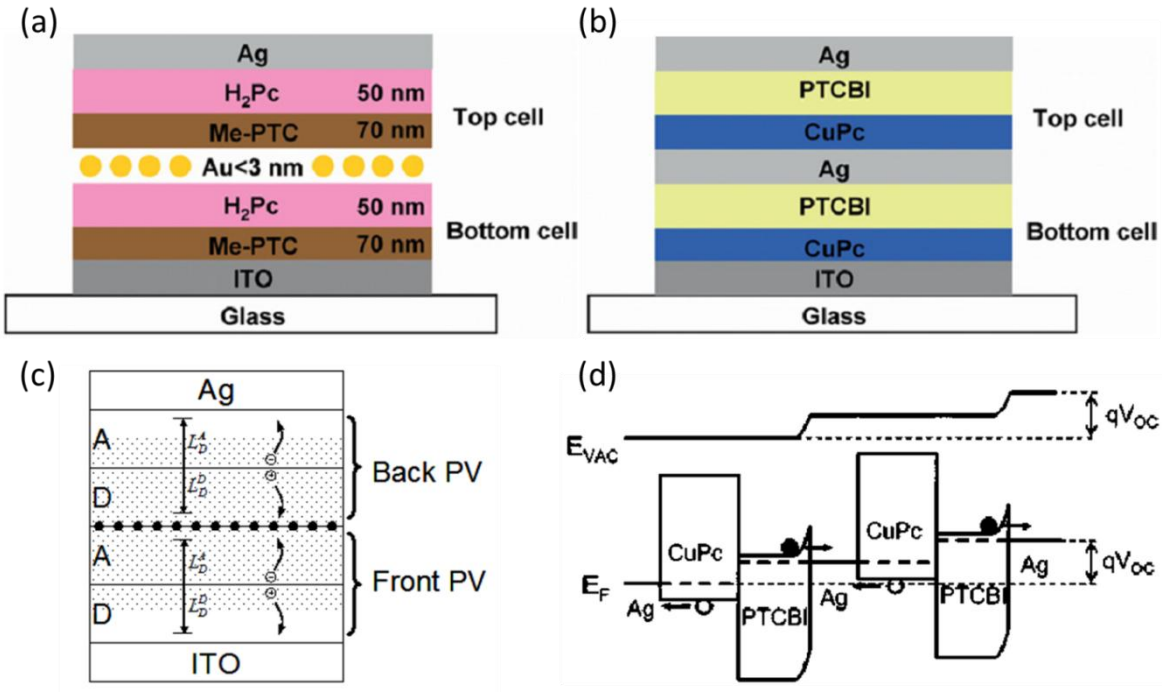

Figure 2.10 Device schematic of (a) the first organic tandem solar cell by Hiramoto,[52] and (b) another similar demonstration by Forrest;[54] (c) illustration of charge recombination at the ICL inside tandem cells; (d) energy level diagram of organic tandem solar cells.[53]

The second ICL design involves one highly doped *p*-type and one highly doped *n*-type interfacial layer. Often in organic solar cells, the highly doped *p*-type layer is called the hole transporting layer (HTL) and the highly doped *n*-type layer is called the electron transporting layer (ETL). Utilization of this more complicated ICL design can improve the charge selectivity at the contact and block unwanted charge carriers while transporting the other. For example, from Figure 2.11a, by placing an *n*-type interface layer on top of photoactive layer, we can

selectively control the upward migration of charge from the bottom subcell to be only electrons. Besides the charge selectivity, both the HTL and the ETL have to be highly doped to minimize the resistance for charge carriers to tunnel. From Figure 2.11b, the energy level diagram represents band bending at the position of the ICL. When both HTL and ETL are highly doped, the depletion width can be narrow and bent in the energy level diagram, which is favorable for charge transport and charge recombination in tandem cells. Below, an equation of depletion width is provided.

$$W = \sqrt{\frac{2 \cdot \varepsilon \cdot (N_D + N_A) \cdot V_{bi}}{q \cdot N_D \cdot N_A}}, \tag{2.14}$$

where ε is permittivity, N_D and N_A are dopant concentration in *n*- and *p*-type materials, and V_{bi} is the built-in potential. In the unfavorable condition where HTL and ETL are absent, the direct contact of the photoactive layers from two junctions would result in a charge depletion region formed at the center of contact. The width of the depletion layer will be large since neither of the organic semiconductors in photoactive layers is highly doped. In the equivalent circuit, the absence of the ICL will form a reverse diode in the middle of the connection, canceling out the voltage addition. The above scenario can be found in Figure 2.11c and Figure 2.11d.

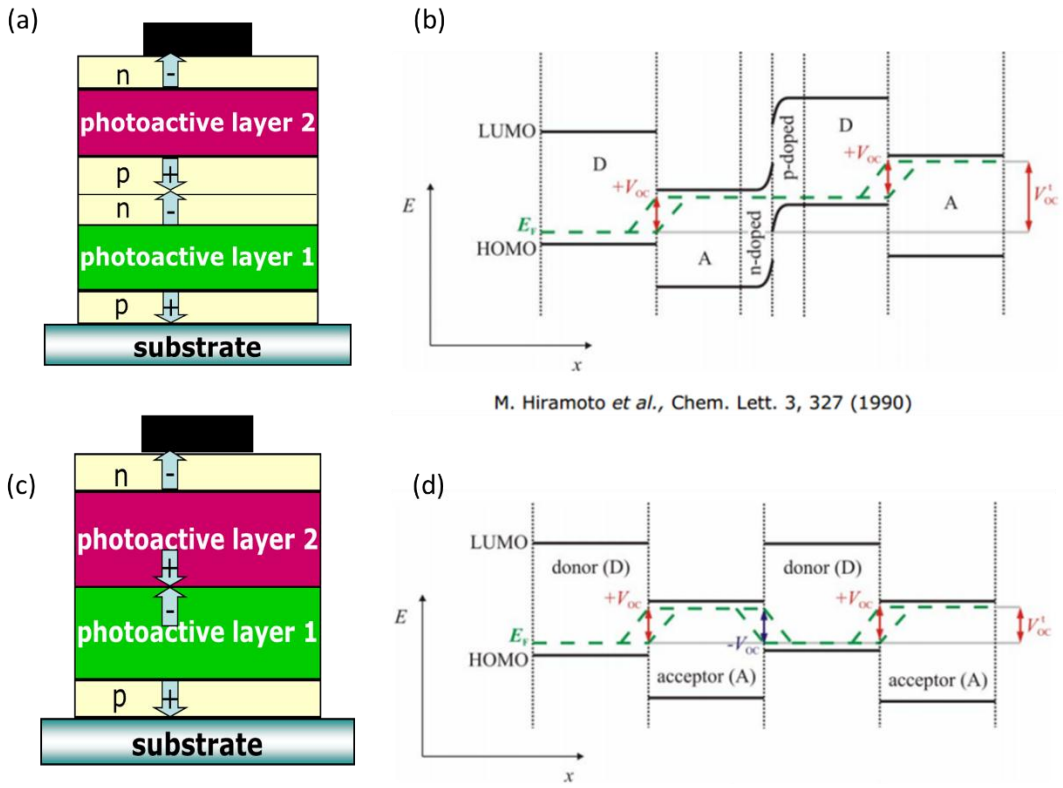

Figure 2.11 (a) The device structure of tandem solar cells with ICL; (b) energy level diagram of a tandem solar cell with ICL;[52] (c) device structure of tandem solar cells without ICL; (d) energy level diagram of tandem solar cells without ICL.[55]

Concluding from the discussion above, in order to design tandem solar cell for high performance, there are several basic rules to follow:

1) The arrangement of the absorbers should follow a cascaded order in forms of energy bandgaps;
2) The difference in the energy bandgap of different absorbers should be considered for current matching;
3) The ICL should consist of either a highly conductive and transparent conductor or two highly doped *p*-type and *n*-type charge transporting layers;
4) The charge transporting layers (e.g., HTL, ETL) should have proper work functions and low resistance in order to extract charges from photoactive layers efficiently.

2.6 Regular vs. inverted tandem solar cells

In the device engineering of organic tandem solar cells, depending on the direction of charge flow, there are two types of structures, as shown in Figure 2.12.

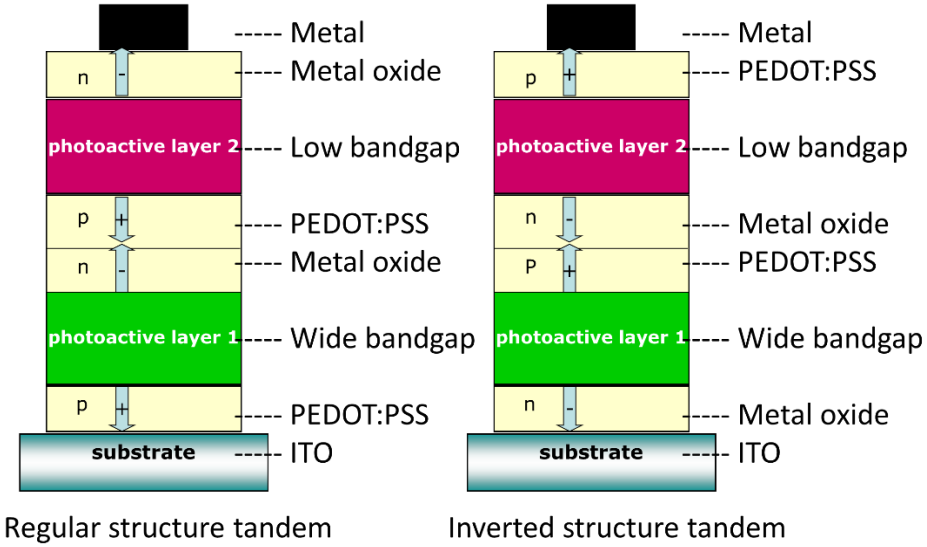

Figure 2.12 Example of two organic tandem structures: regular and inverted tandem devices.

The regular structure for tandem solar cell is mainly based on using the bottom ITO electrode as the anode and the top metal electrode as the cathode. The common metal oxides used for ETL are titanium oxide (TiO_2) and zinc oxide (ZnO). In 2007, Kim et al. reported an regular-structure organic tandem solar cell with TiO_2 as the ETL and PEDOT:PSS as the HTL.[56] It was a major breakthrough at that time with a power conversion efficiency of 6.5%. The device design is provided in Figure 2.13.

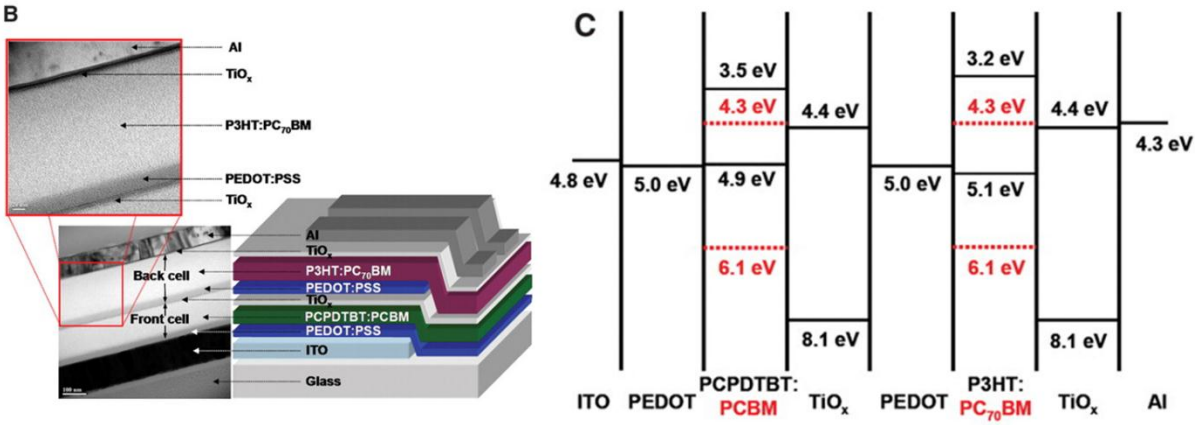

Figure 2.13 Regular tandem device structure and energy level diagram. Figure adapted from *Science*.[56] Copyright © *Science*.

This tandem solar cell in regular structure uses PEDOT:PSS as the HTL and TiO_2 as the ETL. PEDOT:PSS is stacked on top of TiO_2 to form the ICL between the subcells. Here, the work function of TiO_2 (4.4 eV) is close to the LUMO (4.3 eV) of PCBM, thus electron injection into TiO_2 is adjusted with a low energy barrier. The work function of PEDOT:PSS (5.0 eV) is close to the HOMO of P3HT, which plays a similar role in extracting hole carriers out with minimized resistance. Another important aspect of this study is the demonstration of full solution-based processing, which helps maintain the processing advantages of organic solar cell.

The inverted structure for tandem solar cells is based on using bottom ITO electrodes as the cathode and top metal electrodes as the anode. In 2011, Dou et al. reported an inverted organic tandem solar cell with ZnO as the ETL and PEDOT:PSS as the HTL on *Nature Photonics*.[57] It was another major breakthrough with a certified power conversion efficiency of 8.6%. The design is given in Figure 2.14.

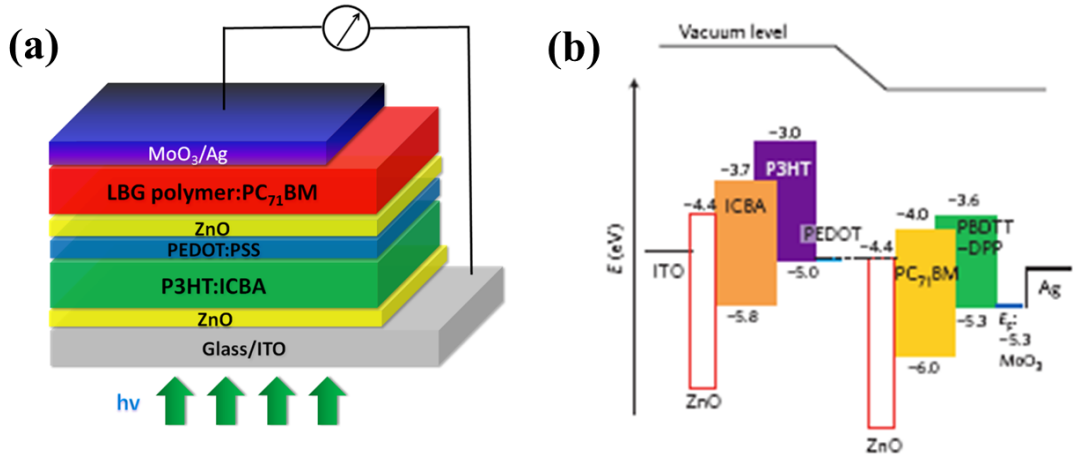

Figure 2.14 Inverted tandem device structure and energy level diagram. Figure adapted from *Nature Photonics*.[57] Copyright © *Nature Photonics*.

Comparing the two device structures on the basis of interconnecting layers, some preliminary results show that inverted-structure tandems outperform the regular-structure tandems. Although there are no solid conclusions for such observations yet, some potential explanations are given by various research groups:

1) Exposing the low work function ETL as the top covering layer may raise stability issues;[58]
2) The charge extraction efficiency may be more efficient at the side close to the ETL due to the morphology of the bulk heterojunction. Thus, when light enters the solar cell from the side of the ETL first, more free charge carriers are generated;[59]
3) The built-in potential is larger in the inverted structure, favorable for charge extraction efficiency;[60]
4) The inverted structure usually uses MoO_3 as the HTL. MoO_3 has better charge selectivity than PEDOT:PSS.[61]

In our work presented in this study, both regular- and inverted-structure tandem solar cells will be introduced and studied. Chapter 4 is based on regular-structure tandem cells, whereas Chapter 5 and 6 are based on inverted-structure cells.

2.7 Building integrated photovoltaics (BIPV)

Building integrated photovoltaics (BIPV) is a new application for organic solar cell technology. In this dissertation, we also demonstrate the potential to integrate organic solar cell devices into BIPV applications. Since the main installation of BIPV is on windows and other exterior materials outside buildings, BIPV requires photovoltaic cells to be highly transparent, if possible, to have color rendering capabilities at least. Such requirements are meant to maintain the exterior look of the building while collecting solar energy. Here, a survey on the current BIPV technology is provided.

The current crystalline or amorphous silicon solar cell can achieve semitransparency through the following methods:

1) Reducing the silicon layer to be less than 20 μm via dicing and transfer printing;[62]
2) Creating a gap between cell connection and lowering the area coverage rate.[63]

The first method was demonstrated by Roger et al. using silicon microcells from bulk wafer and transfer printing to ITO glass.[62] Below, efficiency *vs.* thickness plot (Figure 2.15) is provided from the original paper. The low current density arises from insufficient absorption due to the insufficient thickness. The second method is currently utilized by industry. A demonstration diagram can also be found in Figure 2.16 below. One major disadvantage of this method is that the look of the solar cell affects the overall aesthetic properties of the building, which ultimately limits its utilizations. More details will be elaborated in Chapter 3 and 4.

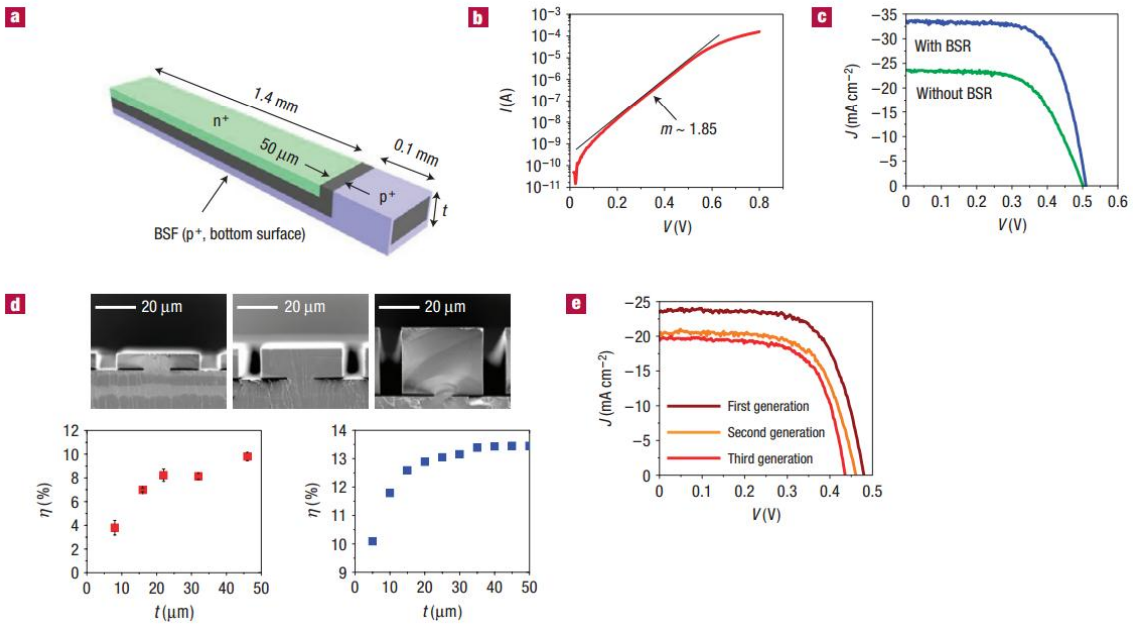

Figure 2.15 Demonstration of semi-transparent silicon solar cell by method 1. Figure adapted from Nature Materials.[62] Copyright © *Natural Materials*.

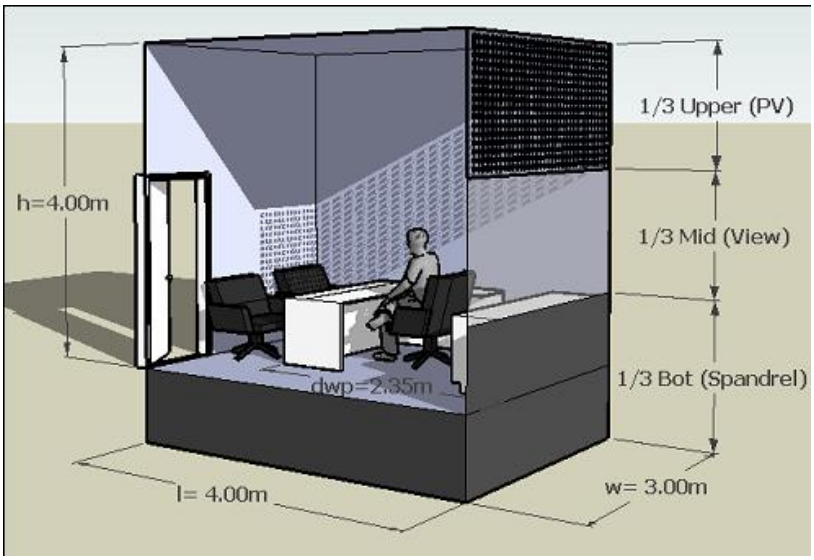

Figure 2.16 Demonstration of semi-transparent silicon solar cell by method 2.[64]

Chapter 3 Design of Visibly Transparent Organic Solar Cells

3.1 Introduction

Polymer solar cells (PSCs) have drawn intense attention due to their advantages over competing solar cell technologies.[65-67] Current progress in the power-conversion efficiency (PCE) of PSCs has reached a new record of 10.6% based on tandem architecture,[68] demonstrating the promising future of PSCs as low-cost and efficient photovoltaic (PV) candidates for solar energy harvesting. In addition to the pursuit of high device efficiency, PSCs have also been intensely investigated for their potential in making unique advances for broader applications.[69, 70] Several such applications would be enabled by high-performance *visibly transparent* PV devices, including building-integrated photovoltaics (BIPV) and integrated PV-chargers for portable electronics.[71, 72]

From the PV materials point of view, an ideal photoactive layer material for visibly transparent PSCs needs to harvest most of the photons from the ultraviolet (UV) and near-infrared (near-IR) wavelengths in the solar spectrum, while the photons in the visible range should be transmitted. Since high PCE is strongly dependent on the fraction of photons absorbed, there is often a compromise between captured photons and polymeric film transparency that limits materials development for visibly transparent PSCs. For example, a poly(3-hexylthiophene) (P3HT) : [6,6]-phenyl-C61- butyric acid methyl ester (PCBM) blend is the most commonly used photoactive layer material in visibly semi-transparent PSCs.[73, 74] However, due to its efficient photon harvesting in the visible wavelength region, P3HT:PCBM (and many other) devices often have low visible transparency.

On the other hand, the transparent conductor is another key factor that determines the performance of visibly transparent PSCs. An ideal transparent conductor for visibly transparent PSCs must simultaneously have high transparency and low resistance together with ease of processing and effective charge collecting. However, a tradeoff is often found with these electrode materials, as high conductivity often sacrifices transparency.[75] For example, thermally evaporated thin metallic films are commonly used as semi-transparent electrodes for PSCs, but this conductivity is significantly compromised by the film transparency.[76, 77]

Previously, many attempts have been made towards demonstrating visibly transparent or semi-transparent PSCs.

a) PV materials, such as P3HT,[78] PCDTBT,[79] and PTB7,[80] have been used as photoactive layers with strong absorption in the visible.
b) Transparent conductors, such as thin metal films,[81] metallic grids,[82, 83] metal nanowire networks,[84, 85] metal oxides,[86, 87] conducting polymers,[88] and graphene,[89] have been deposited onto photoactive layers as top electrodes to achieve semi-transparent PSCs.

However, these demonstrations often result in low visible light transparency and/or low device efficiency, because suitable polymeric PV materials and efficient transparent conductors were not well deployed in device design and fabrication.

In Chapter 3, we demonstrate a solution to overcome the aforementioned challenges for semi-transparent PSCs. High-performance visibly transparent PSCs are achieved by combining 1) polymeric PV materials sensitive to near-IR light but highly transparent to visible light, together with 2) solution-processed high-performance AgNW-based composite transparent conductors. Both visible light transparency and PCE are addressed simultaneously.

3.2 Device structure

Figure 3.1 shows the schematic structure of a visibly transparent PSC. An UV and near-IR light-sensitive photoactive layer is sandwiched between two transparent electrodes. The photoactive layer is a bulk heterojunction (BHJ) blend consisting of a near-IR light-sensitive PV polymer: poly(2,6'-4,8-di(5-ethylhexylthienyl)benzo[1,2-b;3,4-b]dithiophene-alt-5-dibutyloctyl-3,6-bis(5-bromothiophen-2-yl)pyrrolo[3,4-c]pyrrole-1,4-dione) (PBDTT-DPP, Figure 3.3) as the electron donor and PCBM as the electron acceptor.

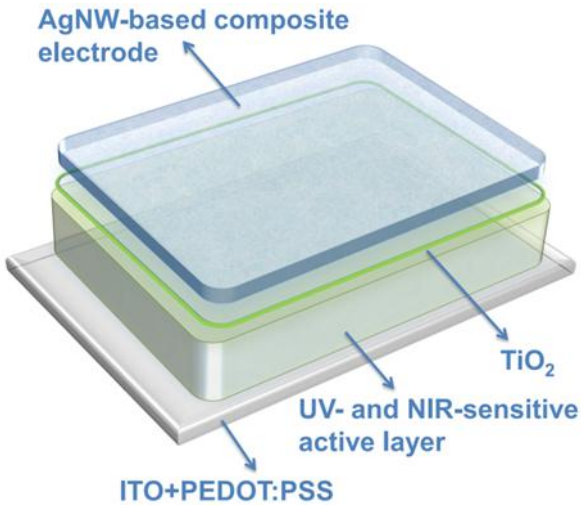

Figure 3.1 Device structure of visibly transparent solar cell.

3.3 Materials and device fabrication

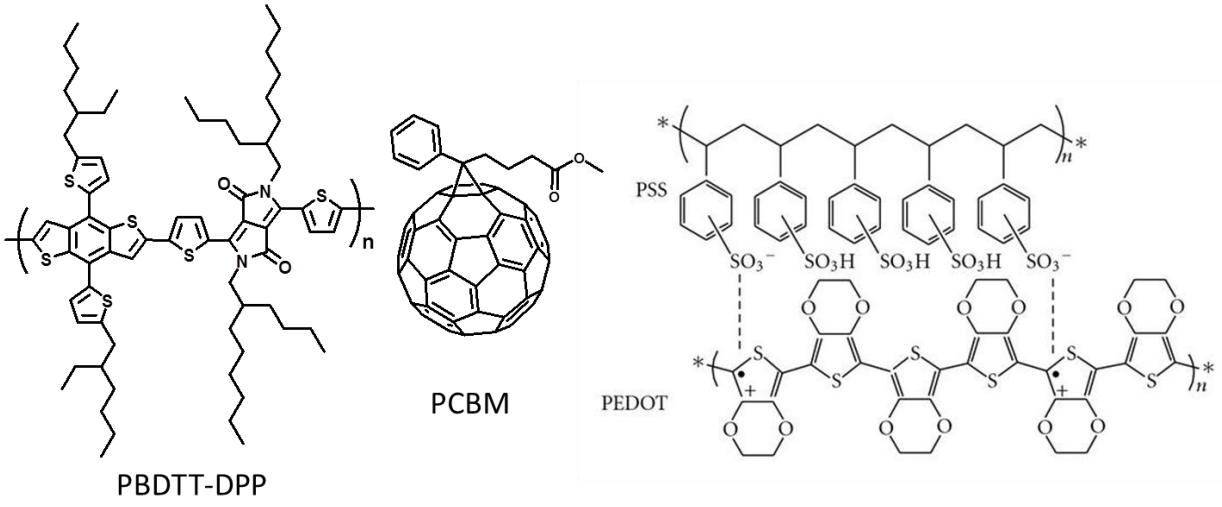

Figure 3.2 Chemical structures of PBDTT-DPP, PCBM, PEDOT:PSS.

Materials

The near-infrared light-sensitive active polymer PBDTT-DPP was developed in our lab.[57] [6,6]-phenyl C_{61}-butyric acid methyl ester ($PC_{61}BM$, aka PCBM) was purchased from Nano-C (Westwood, MA, USA). Poly(3,4-ethylenedioxythiophene)/poly(styrenesulfonate) (PEDOT:PSS, *CLEVIOS*™ P VP Al 4083) was purchased from H. C. Starck (Newton, MA, USA). TiO_2 nanoparticle solutions were prepared according to a previous report.[90] Silver nanowires were purchased from BlueNano Inc. (Charlotte, NC, USA). Indium-tin-oxide nanoparticle dispersions were purchased from Aldrich (Milwaukee, WI, USA).

Fabrication of photovoltaic cells

Visibly transparent polymer solar cells were fabricated on patterned indium tin oxide (ITO)-coated glass substrates with a sheet resistance of 15 Ω/□. The PEDOT:PSS layer was spin-cast at 4000 rpm for 60 s and annealed at 120 °C for 15 min in air. The PBDTT-DPP:PCBM

blend with a weight ratio of 1:2 in dichlorobenzene solution (0.7 wt.%) was spin-cast at 2500 rpm for 80 s on top of the PEDOT:PSS layer to form a ~100-nm-thick active layer. TiO_2 sol-gel solution was then spin-coated onto the active layer at 2500 rpm for 30 s and annealed at 100 °C for 1 min to form the *n*-type interface layer. For the deposition of the AgNW-based composite electrode, the silver nanowire dispersion in isopropyl alcohol (IPA) was spin-coated (2 mg/mL dispersion, 2500 rpm, 10 drops) or spray-coated (0.05 mg/mL dispersion) onto the TiO_2 layer to form the AgNW conducting networks.[29]

The fusing process of the silver nanowire network was then carried out by applying diluted TiO_2 sol-gel solution in ethanol at 3000 rpm and baking at 100 °C for 10 s. The ITO nanoparticle dispersion (10 wt.%) was used as a transparent conductive filler, and was spin-coated onto the fused AgNW matrix to form the composite electrode. Mild heating at 80 °C for 1 min removed the residual solvent. The thickness of the transparent composite electrode is around 400 nm. The device electrode fingers were formed by cutting the films with a blade and blowing the devices with N_2 to avoid possible short circuits between the top AgNWs and the bottom ITO substrate. The active area is 10 mm^2, which is defined by the overlap between bottom ITO substrate and the top fingers.

Optical characterization

The transmission spectra were recorded using a Hitachi ultraviolet-visible U-4100 spectrophotometer (Hitachi High-Technologies Corporation, Tokyo, Japan).

Electrical characterization

Current density-voltage characteristics of the photovoltaic cells were measured using a Keithley 2400 source unit (Keithley Instruments, Inc., Cleveland, OH, USA) under a simulated AM1.5G spectrum with an Oriel 91191 solar simulator (Newport Corporation, Irvine, CA, USA). The light intensity was ~100 $mW \cdot cm^{-2}$, as calibrated using a Si photodiode. The surface resistance (<100 Ω/□) was measured using the four-point probe method with a surface resistivity meter (Guardian Manufacturing, Cocoa, FL, USA, Model: SRM-232-100, range: 0~100 Ω/□). External quantum efficiency (EQE) was measured on a custom-made incident photon-to-current conversion efficiency (IPCE) system.

SEM characterization

The scanning electron microscopy images were taken using an FEI Nova NanoSEM 650 (FEI Corporation, Hillsboro, OR, USA).

3.4 Low-bandgap polymer: PBDTT-DPP

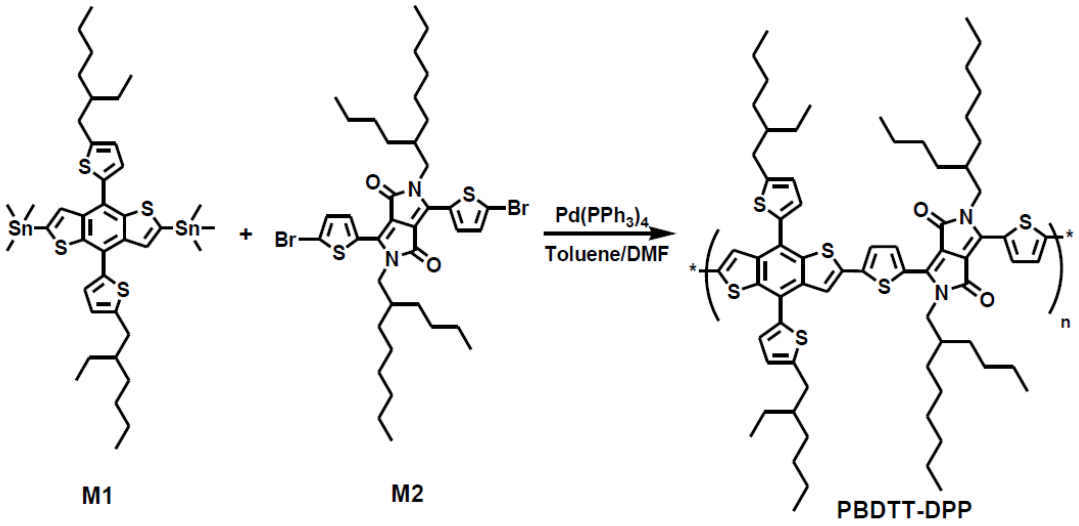

Figure 3.3 Synthetic routes to PBDTT-DPP.

PBDTT-DPP was synthesized according to reported methods.[91] M1 (0.2360 g, 0.2456 mmol) and compound M2 (0.1952 g, 0.2456 mmol) were dissolved into 10 mL toluene and 1 mL DMF in a flask protected by argon. The solution was flushed by argon for 10 minutes, then 10 mg of $Pd(PPh_3)_4$ was added into the flask. The solution was flushed by argon again for 20 minutes. The oil bath was heated to 110 ºC gradually, and the reactant was stirred for 10 hours at 110 ºC under argon atmosphere. Then, the reactant was cooled down to room temperature and the polymer was precipitated by addition of 100 ml methanol, and the precipitated solid was collected and purified by Soxhlet extraction. The title polymer was obtained as dark green-purple solid, yield 30%. The polymer can be readily dissolved into THF, chloroform, chlorobenzene or dichlorobenzene, etc. The polymer was thermally stable up to 290 ºC (3% weight loss by thermogravimetric analysis). ^{1}H NMR (400 MHz, $CDCl_3$): d=6.7-8.6 (br, 10H), 1.8-4.9 (br, 14H), 0.6-1.5 (br, 78H). Mn=40.7 k; polydispersity=2.2.

3.5 Near-infrared absorption of polymer

Figure 3.4 shows the film absorption of PBDTT-DPP, PCBM, and their blend. PBDTT-DPP is a low-bandgap polymer with strong photosensitivity in the range 650-850 nm, while the absorption of PCBM is located below 400 nm. With these two materials in combination, the PBDTT-DPP:PCBM photoactive layer has a maximum transmission of 73% at ~550 nm and an average transmission of 68% over the entire visible range (400 to 650 nm), but is strongly absorbing in the near-IR range (from 650 to 850 nm), as shown in Figure 3.4. This spectral coverage of PBDTT-DPP:PCBM film ensures the harvesting of UV and near-IR photons while most visible photons are transmitted, making PBDTT-DPP:PCBM an excellent candidate for the visibly transparent PSCs.

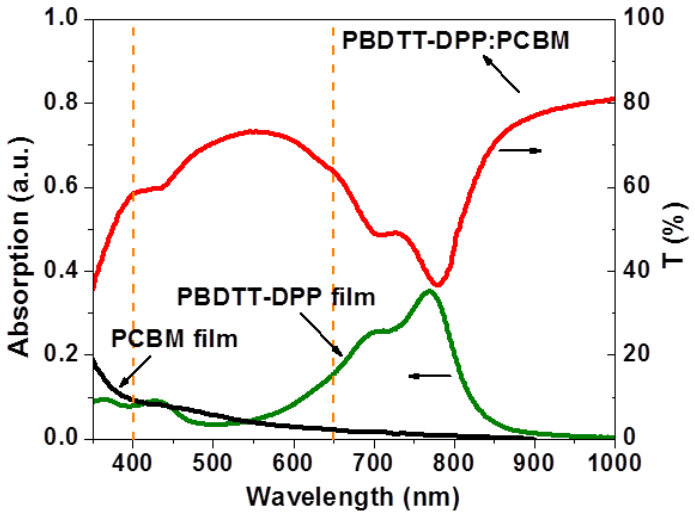

Figure 3.4 Transmission and absorption spectra of PBDTT-DPP, PCBM, and their blend.

3.6 Silver nanowire composite electrode

Some recently developed solution-processable conductive materials, such as carbon nanotubes,[92, 93] graphene,[94, 95] poly(3,4-ethylenedioxythiophene):poly(styrene sulfonate) (PEDOT:PSS),[96, 97] and silver nanowires (AgNWs),[98, 99] have opened up a new era for transparent conductors. Despite the unique advantages of these candidates, they all have drawbacks limiting their applications in visibly transparent PSCs. For example, one major drawback is the damage caused by these transparent conductors to the underlying, soft polymeric photoactive layers during their deposition. Other issues include the chemical, physical, mechanical, or energetic incompatibility between the polymeric photoactive layer and the transparent conductor that can lead to the low performance or low transparency of the visibly transparent PSCs reported to date.

Here, we define the electrode deposited onto the photoactive layer as the top electrode and the electrode on which the photoactive layer is coated as the bottom electrode. Commercial

indium-tin-oxide (ITO) substrates can be chosen as the bottom anode electrode, which is often covered by PEDOT:PSS as an anode-modification layer. However, great challenges remain for the high-performance transparent top cathode that is to be deposited on top of the photoactive layer. The dominant reason is the aforementioned compatibility issue, because polymer or organic films are often too thin and soft to survive the deposition processes required for most transparent conductors.

To solve this problem, a spray-coated AgNW-based composite is applied in our approach to fabricate the high-performance top transparent cathode. The AgNWs can be spray-coated onto the photoactive layer through alcohol-based solvents, which are compatible with common PSC materials. Figure 3.5 shows the scanning electron microscopic (SEM) image of the top surface of the AgNW network. As we can see from the SEM images, the connecting spots between AgNW are loosely bounded with lots of gaps.

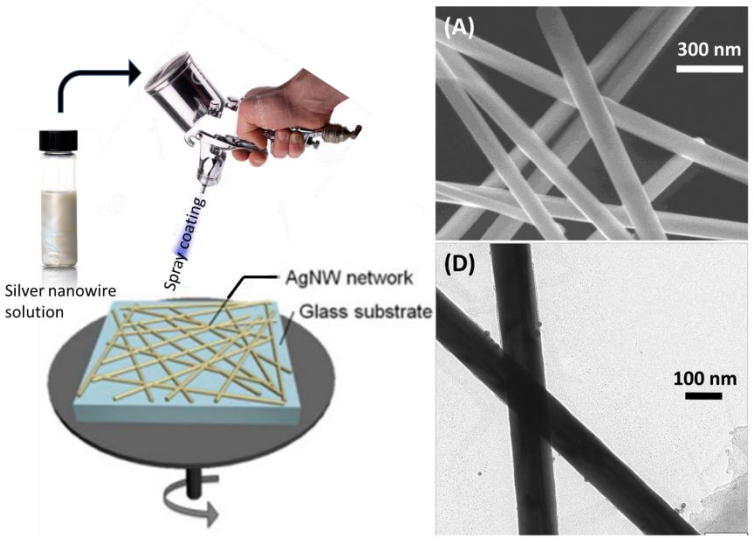

Figure 3.5 Demonstration of AgNW by spray-coating. SEM images of pure AgNW without any treatment.[100]

The AgNW network is then fused using a TiO_2 sol-gel solution to enhance the connection between AgNWs and the adhesion of AgNWs to the underlying photoactive layers. Due to the TiO_2 solvent evaporation, the capillary force induced by solution volume shrinkage tightens up the contacts across AgNWs thus improving film conductivity. This step only requires mild processing conditions of 100 °C for a few seconds, and can achieve the same excellent low resistivity as high temperature sintered AgNW does.[99]

Furthermore, since the morphology of organic bulk heterojunction is typically sensitive to the temperature, our method also demonstrates a good compatibility with the organic photoactive layer. Figure 3.6 shows the SEM image of the top surface of the AgNW modified by TiO_2. TiO_2 nanoparticles (diameter size 3~5 nm) are glued to the surface of AgNW, thus the connecting spots between AgNWs are now fused by the TiO_2.

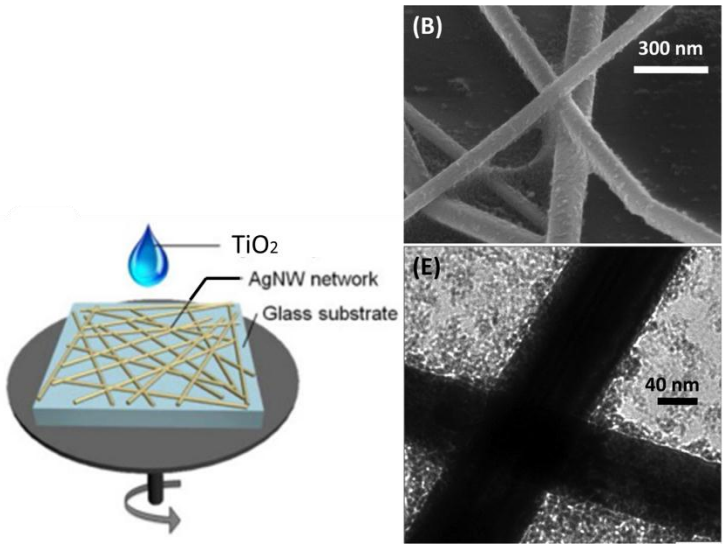

Figure 3.6 Demonstration of AgNW network fused by TiO_2. SEM images of AgNW + TiO_2.[100]

Next, transparent conductive fillers are placed in the empty space in the crossed AgNW conducting network. The conductive filler is designed to extract the charges generated from the

areas that are not covered by AgNWs and transport these charges to the AgNW matrix. Here, we chose indium tin oxide nanoparticles (ITO NP) as the filler for the AgNW network to form the AgNW-based composite transparent conductor. The ITO-based filling material also contains polymeric binder that can improve the adhesion of AgNW networks onto the photoactive layer and form a continuous film with good contact with the underlying active layer.

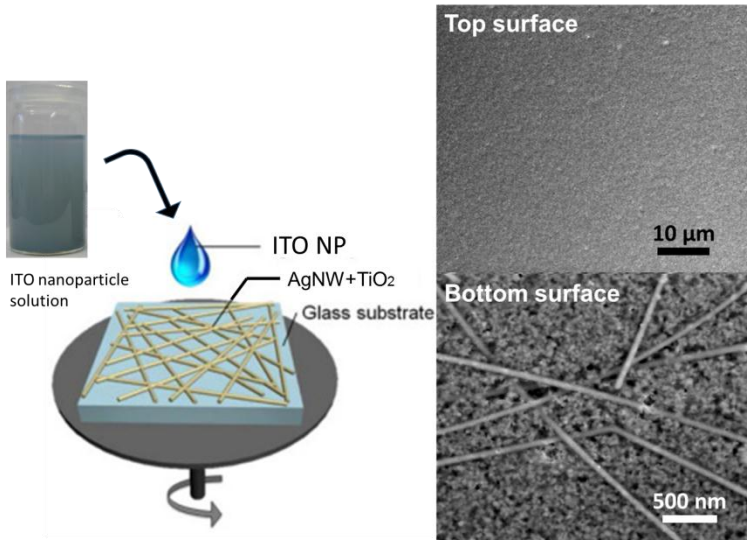

Figure 3.7 Demonstration of AgNW + TiO_2 network filled by ITO NP. SEM images of AgNW + TiO_2 + ITO NP.

Figure 3.7 shows a SEM image of the top surface of the AgNW-TiO_2-ITO NP composite electrode. The AgNW networks are completely buried in the ITO nanoparticle-based conductive filling material, resulting in a smooth top surface. By using a "floating-off" technique,[101] the composite transparent electrode can be flipped to expose the bottom surface, which is in contact with the underlying photoactive layer. Figure 3.7 also shows a SEM image of the bottom surface of the composite transparent conductor. The AgNWs from the bottom surface are exposed to the

active layer, which indicates that ITO nanoparticles did not diffuse into the contact area between AgNWs and the active layer, but only filled the hollow space between the AgNWs.

Figure 3.8 shows the transmittance spectra of the ITO nanoparticle film alone and the AgNW-based composite film containing ITO nanoparticle fillers. The ITO nanoparticle film (thickness ~400 nm) alone has high transparency within the visible and near-IR ranges and low sheet resistance of ~100 kΩ/□ measured *via* four-point probe measurements. The pristine AgNWs films prepared by spray-coating methods have resistances of >1 MΩ/□ initially. After being treated with the TiO_2 sol-gel solution and further coated by the ITO nanoparticle fillers, the resulting AgNW composite films have an average transmittance of ~87% from 400 to 1000 nm with sheet resistances of ~30 Ω/□. These results have met the requirements for the top cathode of a visibly transparent PSC.

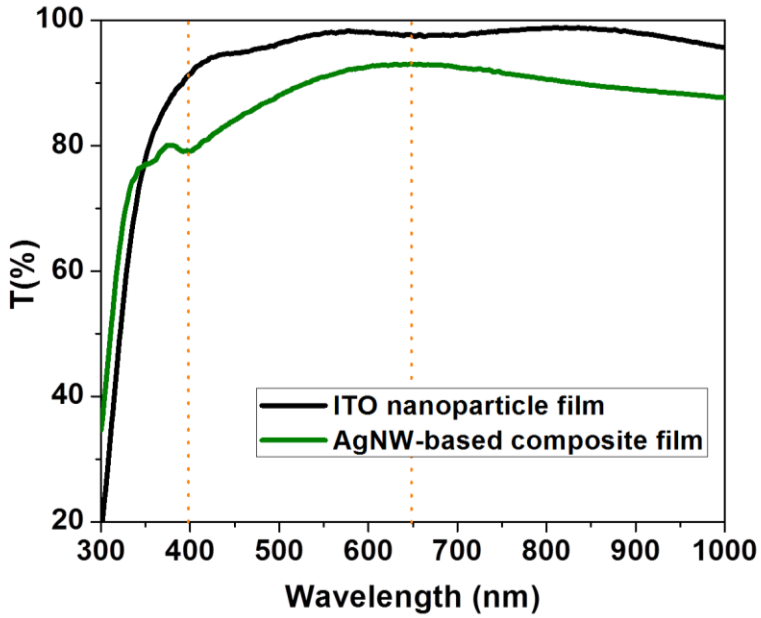

Figure 3.8 Transmission spectra of AgNW composite electrode and ITO nanoparticle.

3.7 TiO_2 as protective layer

Between the active layer and top electrode, a suitable interface modification layer is also critical. The interlayer not only acts as a protective film on the soft photoactive layer, but also reduces the energy barrier for carrier transport from photoactive layer to top electrode. Here, we deposited a 20-nm-thick TiO_2 nanoparticle from a sol-gel solution on top of the photoactive layer to act as cathode interfacial layer.[90, 102] The TiO_2 nanoparticle layer prevents the silver nanowire from damaging the underlying soft films. Moreover, owing to its photoconductivity and proper work function alignment with the photoactive polymer material, the TiO_2 nanoparticle layer serves as an efficient electron-transporting layer and allows electrons to tunnel through the energy barrier into the AgNW-based electrode.

3.8 Visible transparency of device

In terms of transmission, based on the above device structure we produced solution-processed and visibly transparent PSCs with an average light transmission of 61% over the 400 to 650 nm range and a maximum transmission of 66% at ~550 nm (Figure 3.9b). Figure 3.9a shows a photograph of a highly transparent PSC where the buildings behind can be clearly seen through the device. The yellow and blue brackets indicate the edge of the top AgNW-based composite electrode and the bottom ITO electrode, respectively.

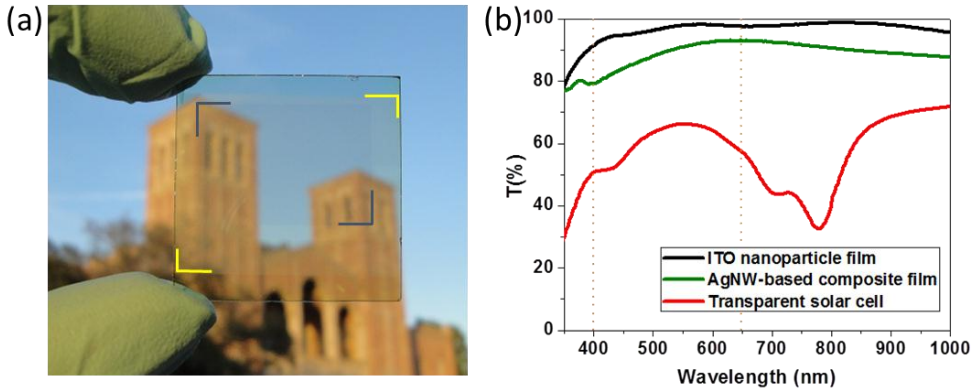

Figure 3.9 (a) Photograph of a visibly transparent polymer solar cell. The yellow and blue brackets indicate the top AgNW-based composite electrode and the bottom ITO electrode, respectively; (b) Transmission spectra of the pristine ITO nanoparticle film, the AgNW-based composite transparent electrode and a visibly transparent polymer solar cell.

3.9 Photovoltaic performance

Figure 3.10a demonstrates the current density-voltage (*J-V*) curves of this visibly transparent PSC measured under simulated AM 1.5G illumination with an intensity of 1000 $W \cdot m^{-2}$. The performance of a control device is also shown in Figure 3.10a, which uses evaporated Al as a reflective top electrode. For the control device, a power conversion efficiency (PCE) of 6.03% was obtained with a short-circuit current density (J_{SC}) of 13.0 $mA \cdot cm^{-2}$, an open-circuit voltage (V_{OC}) of 0.78 V, and a fill factor (*FF*) of 59.5%. In the testing of the visibly transparent PSCs, we measured the device performance with illumination from either the ITO substrate side or the top AgNW-composite transparent conductor side.

When illuminated from the ITO substrate side, a PCE of 4.02% was achieved with V_{OC} = 0.77 V, J_{SC} = 9.3 $mA \cdot cm^{-2}$ and *FF* = 56.2%. When the device test was performed with illumination from the top AgNW-composite electrode side, similar performance was obtained: V_{OC} = 0.76 V, J_{SC} = 8.7 $mA \cdot cm^{-2}$, *FF* = 57.8% and *PCE* = 3.82%. Both measurements show

similar V_{OC} and *FF*. The only difference comes from the J_{SC}, which is due to the slightly lower transparency of the AgNW-based composite electrode films as compared to the commercial ITO substrates. To understand the reproducibility of the results obtained, 40 transparent PSCs were prepared and consistent results of PCE in between 3.6-4% were obtained with illumination from ITO substrate side.

Figure 3.10c shows the external quantum efficiency (EQE) characterization of the visibly transparent PSCs. J_{SC} can be calculated by integrating the EQE results with the solar spectrum. The J_{SC} obtained by EQE illumination from the ITO and AgNW side are 8.99 and 8.32 $mA \cdot cm^{-2}$, respectively. These values are roughly consistent with the results obtained from the *J-V* characterization. Moreover, a reflective mirror can be placed at the back of the visibly transparent PSC to reflect the transmitted photons back to the device, as illustrated in tests C and D of Figure 3.10b. The J_{SC} measured from EQE of tests C and D are 12.16 and 11.01 $mA \cdot cm^{-2}$, respectively. Table 3.1 summarizes the *J-V* characterization of different measurements described in Figure 3.10a. The J_{SC} of 12.60 $mA \cdot cm^{-2}$ obtained from test C is comparable to that of our control devices (13.0 $mA \cdot cm^{-2}$ with conventional TiO_2/Al electrode). These results show that the photons transmitted through the visibly transparent PSCs can still be utilized for the energy generation or other optical applications, indicating the broad applications of visibly transparent PSCs.

Table 3.1 Summary of device performance under different testing conditions as described in Figure 3.10.

Testing conditions	V_{OC} (V)	J_{SC} (mA/cm^2)	*FF* (%)	*PCE* (%)
A. From the ITO side, no mirror	0.77	9.30	56.2	4.02
B. From the AgNW side, no mirror	0.76	8.70	57.8	3.82
C. From the ITO side, with reflective mirror	0.77	12.60	54.4	5.28
D. From the AgNW side, with reflective mirror	0.76	11.63	55.7	4.92

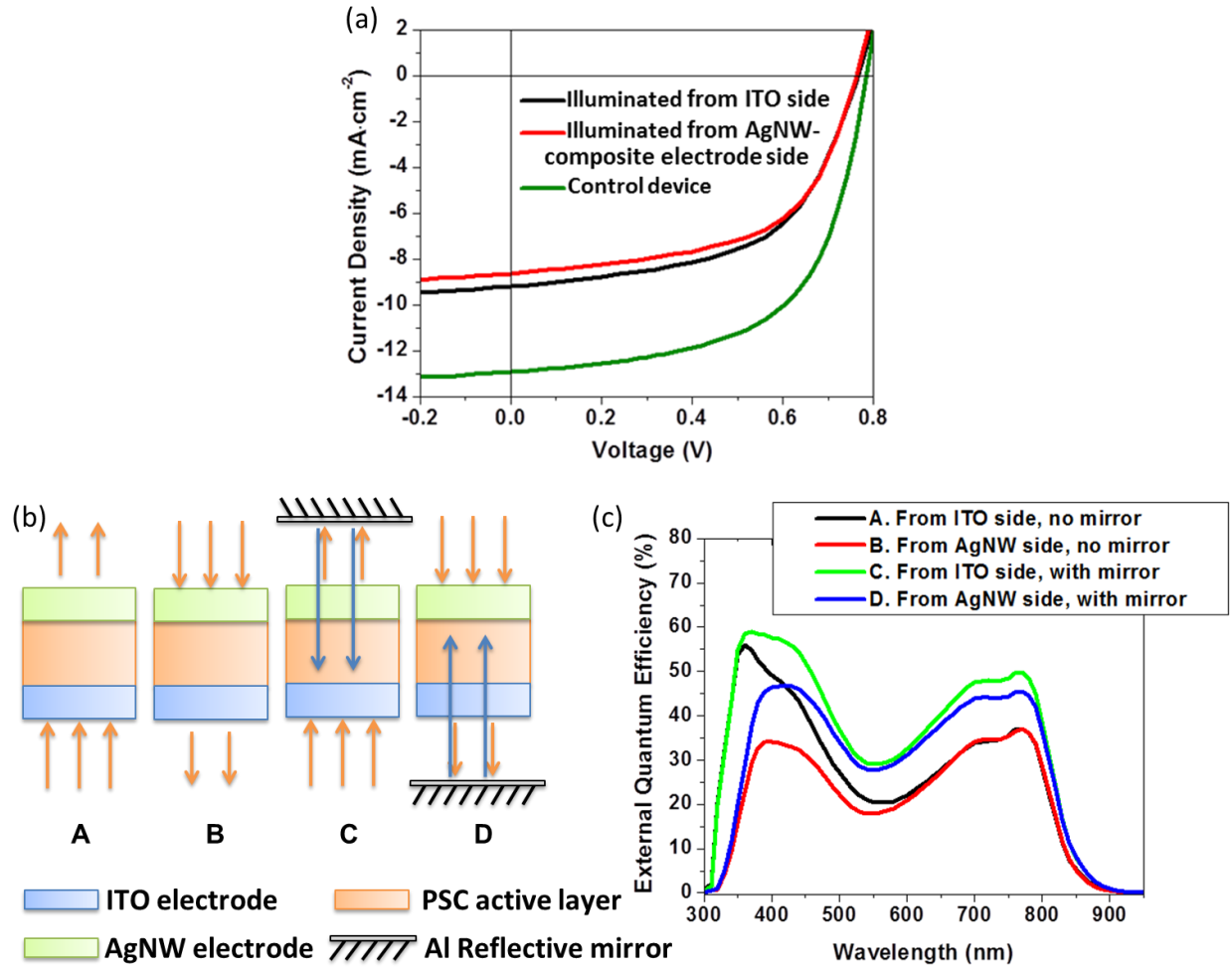

Figure 3.10 (a) *J-V* characterization of the transparent device (illuminated from ITO side or AgNW composite electrode side) and the control device (using reflective thermal-evaporated Al as top electrode); (b) External quantum efficiency (EQE) characterization of the visibly transparent PSC with different testing methods. The incident light beam illuminated from both ITO (A) and AgNW (B) electrode sides were investigated. An Al-based reflective mirror was then placed at the back of the transparent device to reflect the transmitted photons back to the device (C and D) and the EQE spectra were also collected. The calculated J_{SC} values based on the EQE results for these tests are: (A) 8.99 mA·cm^{-2}; (B) 8.24 mA·cm^{-2}; (C) 12.16 mA·cm^{-2}; (D) 11.01 mA·cm^{-2}.

3.10 Summary

In single-junction devices, we have demonstrated high-performance, solution-processed, visibly transparent polymer solar cells through the incorporation of near-infrared light-sensitive polymer and using silver nanowire composite films as the top transparent electrode. The near-infrared photoactive polymer, PBDTT-DPP, absorbs more near-infrared light but is less sensitive to visible light, balancing solar cell performance and transparency in the visible wavelength region. The transparent top electrode is a fully solution-processed silver nanowire-based composite film, which is compatible with common PSC materials. With this combination, we have achieved ~4% power-conversion efficiency for the solution-processed and visibly transparent solar cells, while the devices have high transparency, 66% at 550 nm. These results open the potential for visibly transparent polymer solar cells as add-on components of multi-junction photovoltaic devices, smart windows, building-integrated photovoltaics, and in other applications.

Chapter 4 Semi-Transparent Organic Solar Cells via Tandem Structure

4.1 Introduction

In the previous chapter, we attempted to optimize both photovoltaic performance and optical transparency simultaneously through the fabrication of an infrared-absorbing solar cell featuring a silver nanowire (AgNW) composite electrode. We obtained high visible transmission and a PCE of 4% in a single-junction device. However, the photocurrents of these transparent PSC remained poor as a result of the optical loss through the transparent electrodes that only allowed polymer film to capture the incident light in a single pass.

Ideally, we wish to increase the degree of absorption by escalating the thickness of polymer films, however, thin polymer films are often required for the active layer to suppress charge recombination.[53] Similar observations were reported by Kim et al. indicating that when the thickness of the single-junction organic solar cell exceeds its estimated electron drift distance, the average EQE drops to 30%.[56]

To reach a balance between maximum absorption and sufficient charge extraction, it was necessary for the photoactive layer in our previously demonstrated single-junction transparent PSC to have a thickness less than 120 nm.[103] One way to enhance the effective absorption is to stack polymer films in serial connection in a tandem architecture.[51] Accordingly, multiple photoactive materials can readily be introduced into one PSC device, allowing fine adjustment of its absorption and, thus, its external color.

In this chapter, we stack two IR-absorbing organic bulk heterojunctions as subcells in tandem structures to increase the absorption efficiency of solar energy in the IR range and, thereby, obtain semi-transparent solar cells exhibiting greater photovoltaic performance.

4.2 Tandem device structure

Figure 4.1 shows the schematic structure of a tandem-structure, semi-transparent PSC. In this section, we report semi-transparent PSC, possessing a tandem structures featuring:

a) Two new low-bandgap polymers, PBDTT-FDPP-C12 and PBDTT-SeDPP, that sensitize well in different regions of IR spectrum. Through the variation of chemical structures, we could differentiate the photoresponse of IR-sensitive polymer from 900 to 950 nm thus improve the current in the tandem solar cell.

b) Two different fullerene derivatives, $PC_{61}BM$ and $PC_{71}BM$, which have different strengths in harvesting visible photons. Therefore, they can be used to tune the visible transparency of devices.

c) A new interconnecting layer (ICL) design that is solution-processed, and low-temperature derived. We also found that the conjugated polyelectrolyte as the interfacial dipole layer could lead to improved electrical connections between the two subcells.

Figure 4.1 introduces two designs of semi-transparent tandem structure PSC, depending on the combination of front and back subcell materials. Semi-transparent tandem 1 focuses on high visible transparency and uses $PC_{61}BM$ in both front and back subcells. Semi-transparent tandem 2 focuses on high photovoltaic performance and uses $PC_{71}BM$ in the back subcell.

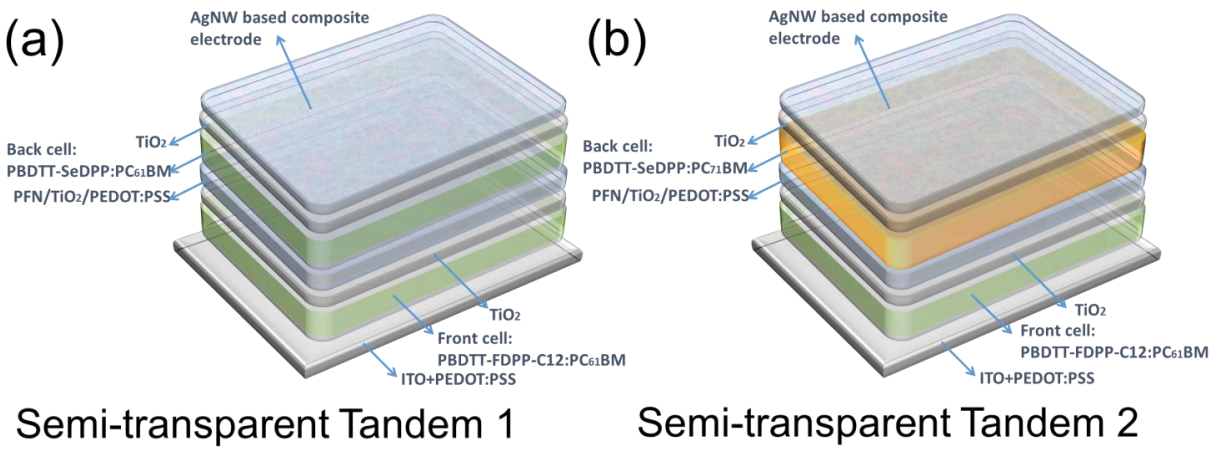

Figure 4.1 Device structure of semi-transparent organic solar cell in tandem structure.

4.3 Materials and fabrication method

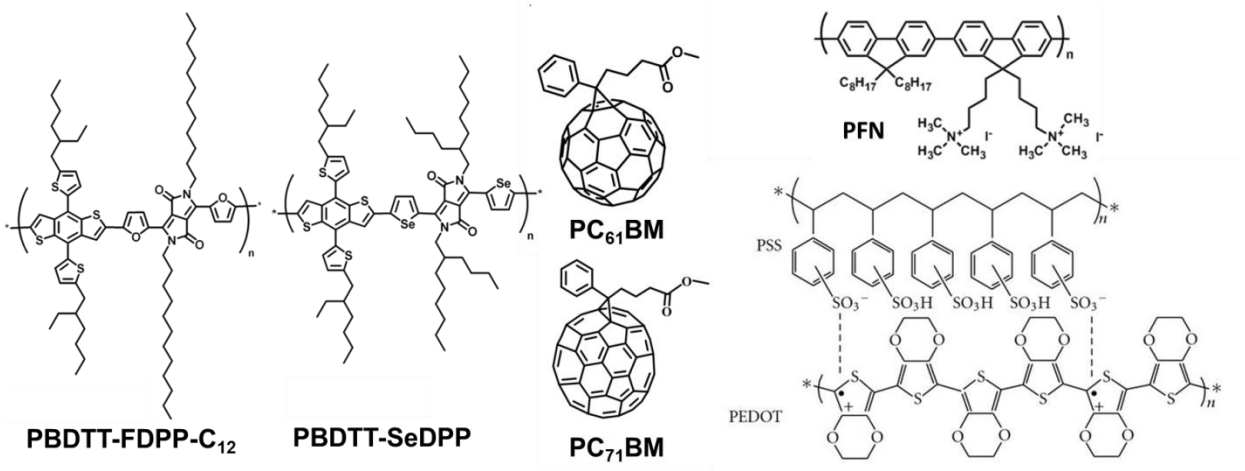

Figure 4.2 Chemical structures of PBDTT-FDPP-C12, PBDTT-SeDPP, $PC_{61}BM$, $PC_{71}BM$, PEDOT:PSS, and PFN.

Materials

The near-infrared light-sensitive active polymer PBDTT-SeDPP and PBDTT-FDPP-C12 was developed in our lab.[36, 104] [6,6]-phenyl C_{61}-butyric acid methyl ester ($PC_{61}BM$) and

[6,6]-phenyl C_{71}-butyric acid methyl ester ($PC_{71}BM$) was purchased from Nano-C (Westwood, MA, USA). Poly(3,4-ethylenedioxythiophene): poly(styrenesulfonate) (PEDOT:PSS, *CLEVIOS*™ P VP Al 4083) was purchased from H. C. Starck (Newton, MA, USA). TiO_2 nanoparticle solutions were prepared according to a previous report.[103] Poly[(9,9-dioctyl-2,7-fluorene)- alt -(9,9-bis(3'-(N, N dimethylamino)propyl)-2,7-fl uorene)] (PFN) was purchased as ADS180BE from American Dye Source Inc (Quebec, Canada). Silver nanowires (AgNW) were purchased from BlueNano Inc. (Charlotte, NC, USA). Indium-tin-oxide nanoparticle dispersions were purchased from Aldrich (Milwaukee, WI, USA).

Single-junction device fabrication

Pre-cleaned indium tin oxide (ITO) substrates (sheet resistance of 15 Ω/□) were first treated with UV-ozone for 15 min. A PEDOT:PSS layer was spin-coated (4000 rpm, 60 s) and then annealed (120 °C, 15 min) in air. A solution of the polymer (PBDTT-FDPP-C12, PBDTT-SeDPP):fullerene ($PC_{61}BM$, $PC_{71}BM$) blend (weight ratio, 1:2) in dichlorobenzene (0.7 wt.%) was spin-coated (2500 rpm, 80 s) on top of the PEDOT:PSS layer to form the active layer (thickness: ca. 100 nm). A TiO_2 sol–gel solution was spin-coated (2500 rpm, 30 s) onto the active layer and then it was annealed (100 °C, 30 s) to form the *n*-type interfacial layer. A dispersion of AgNW in isopropyl alcohol (IPA) was diluted to 2 mg/mL and dropped onto TiO_2 layer rotating at 2500 rpm to form a 100-nm-thick conducting network of AgNW. A diluted ITO nanoparticle (ITO NP) dispersion (10 wt.% in IPA; Sigma–Aldrich) was dropped onto the AgNW matrix rotating at 4000 rpm to form the composite electrode. Each device was formed by cutting the films with a razor blade and blowing N_2 onto the devices to avoid short circuits between the top AgNW network and the bottom ITO substrate. The active area, defined by the

overlap between bottom ITO substrate and the top fingers, was 10 mm^2; it was calibrated using an optical microscope.

Tandem device fabrication

The fabrication of the front subcell followed the procedure for the preparation of the single-junction device until the active layer was deposited, at which point the diluted PFN solution (0.02 wt.% in methanol) was spin-coated at 4000 rpm.[105] The thickness of the PFN interlayer was approximately 10 nm. A TiO_2 sol–gel solution was spin-coated at (2500 rpm, 30 s) onto the PFN layer and then it was annealed (100 °C, 10 s) to form the *n*-type dual interfacial layer. A conductive PEDOT:PSS (85 vol.% Clevios PH1000, 10 vol.% IPA, 5 vol.% DMF) was spin-coated onto the TiO_2 surface at 4000 rpm. The second resistive PEDOT:PSS (100 vol.% Clevios AI 4083) was spin-coated at 4000 rpm to form double PEDOT:PSS layer structure. The back subcell was fabricated in the same manner as the front cell, with the rate of spin coating ranging from 2000 to 3500 rpm. Finally, the remaining TiO_2 buffer layer, AgNW electrode, and ITO NP as conductive fillers were deposited using the same procedures as those described for the preparation of the single-junction cells.

Device characterization

The current density–voltage (*J–V*) characteristics of the photovoltaic cells were recorded with a 0.1 cm^2 mask using a Keithley 2400 source-measurement unit under a simulated AM1.5G illumination from an Oriel 9600 solar simulator. A KG-5 filter silicon photodiode (traceable to NREL calibration) was used as the reference cell to calibrate the light intensity to 1 sun (100 mW/cm^2). To avoid parasitic current during measurement, each device (finger) was isolated completely by scratching the surrounding films around the device. The transmission and

absorption of the devices were measured using a Hitachi U-4100 UV-Vis-NIR double beam spectrophotometer. External quantum efficiencies (EQEs) were measured using an Enlitech QE-R spectral response measurement system to calibrate the current density of devices.

4.4 Low-bandgap polymer: PBDTT-FDPP-C12

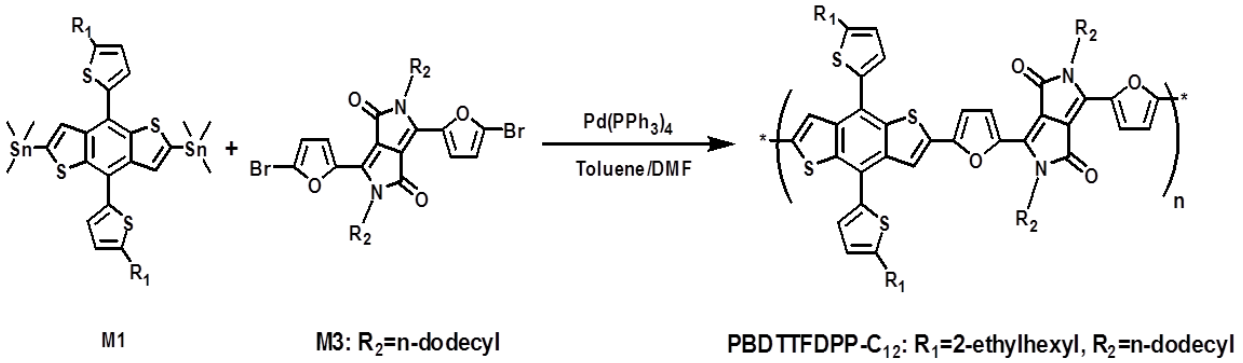

Figure 4.3 Synthetic route to PBDTT-FDPP-C12.

Synthesis of PBDTT-FDPP-C12: All monomers (M1 and M3) were synthesized according to reported methods.[91] The polymerization of the polymers is shown in Figure 4.3. PBDTTFDPP-C12 was synthesized as follows: M1 (0.2222 g, 0.2456 mmol) and compound M3 (0.1742 g, 0.2451 mmol) were dissolved into 10 mL toluene and 1 mL DMF in a flask protected by argon. The solution was flushed by argon for 10 minutes, then 10 mg of Pd $(PPh_3)_4$ was added into the flask. The solution was flushed by argon again for 20 minutes. The oil bath was heated to 110 ºC gradually, and the reactants were stirred for 8 hours at 110 ºC under argon atmosphere. Then, the mixture was cooled down to room temperature and the polymer was precipitated by addition of 100 ml methanol, and the precipitated solid was dissolved in ~10 mL $CHCl_3$ and then passed through a short column with silica gel. The solution was then concentrated to 5~10 mL and precipitated in hexane. The polymer was thermally stable up to 270 ºC (3% weight loss by

thermogravimetric analysis). ^{1}H NMR (400 MHz, $CDCl_3$): d=6.7-8.6 (br, 10H), 1.8-4.9 (br, 14H), 0.5-1.5 (br, 62H). Mn=42.4 k; polydispersity=2.2.

4.5 Low-bandgap polymer: PBDTT-SeDPP

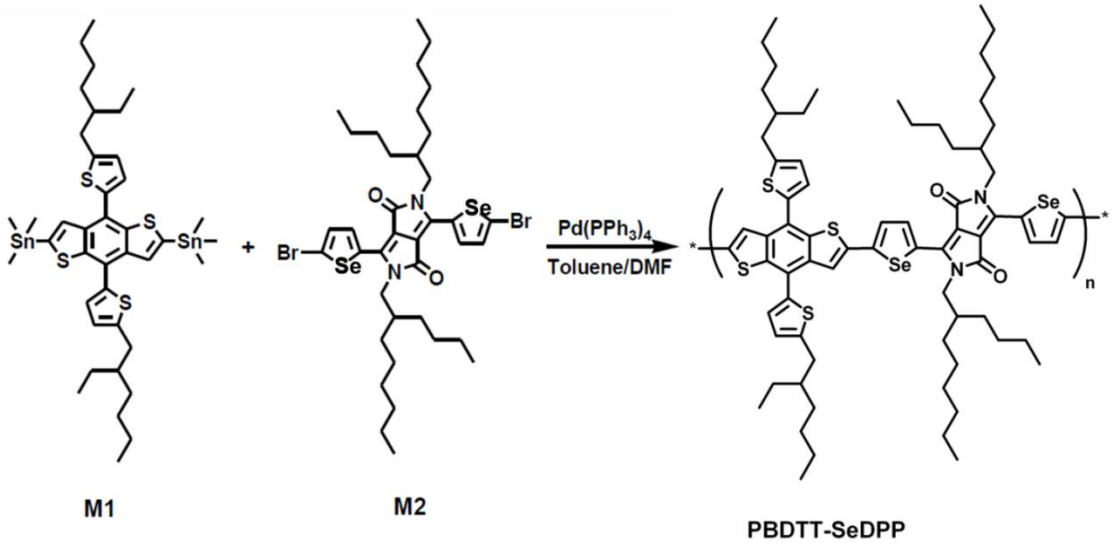

Figure 4.4 Synthetic route to PBDTT-FDPP-C12.

Synthesis of PBDTT-SeDPP: All monomers (M1 and M2) were synthesized according to reported methods.[104] M2 (0.1760 g, 0.1981 mmol) and compound M1 (0.1810 g, 0.2001 mmol) were dissolved into 10 mL toluene and 1 mL DMF in a flask protected by argon. The solution was flushed with argon for 10 minutes, then 10 mg of $Pd(PPh_3)_4$ was added into the flask. The solution was flushed with argon again for another 10 minutes. The oil bath was heated to 115 ºC gradually, and the reaction mixture was stirred for 8 hours at 115 ºC under argon atmosphere. Then, the mixture was cooled down to room temperature and the polymer was precipitated in 100 ml methanol and the precipitated solid was collected and purified by silica gel chromatography using chloroform as eluent. The polymer was obtained as dark green-purple solid, yield 56%. The polymer can be readily dissolved into chloroform, chlorobenzene or

dichlorobenzene, etc. ^{1}H NMR (400 MHz, $CDCl_3$): d=6.4-9.0 (br, 10H), 2.5-4.0 (br, 12H), 0.6-1.6 (br, 72H). Mn=38.0 k; polydispersity=2.1.

4.6 Optical absorption tunability by fullerene

Figure 4.5 displays the absorption spectra. Unlike conventional tandem solar cells that usually incorporate one visible-sensitive polymer and one IR-sensitive polymer,[57] in our present approach we used two IR-sensitive polymers to minimize optical absorption in the visible spectrum. To avoid complete overlap of the absorption spectra of the two polymers in the IR range, PBDTT-FDPP-C12, a new IR-sensitive polymer, was created. In Figure 4.5, we observe a 50-nm blue-shift of the spectral signal of PBDTT-FDPP-C12, together with a narrower absorption band, as compared to PBDTT-SeDPP. The optical energy bandgaps of PBDTT-FDPP-C12 and PBDTT-SeDPP were 1.49 and 1.38 eV, respectively. The relatively wide bandgap of PBDTT-FDPP-C12 was critical for improving the current gain in the tandem structure.

Figure 4.5 also displays the structures of the fullerene derivatives $PC_{61}BM$ and $PC_{71}BM$, which we used as electron acceptor materials in the active layer. We observe that the absorbance spectrum of $PC_{61}BM$ exhibits very limited photo-response in the visible, whereas that of $PC_{71}BM$ displays a broad, strong signal from 400 to 700 nm. As a result, we chose to combine:

a) *IR-sensitive polymer and $PC_{61}BM$* as the **transparent absorber** for the solar cell devices that requires high visible transparency, since $PC_{61}BM$ allows most of visible photons to pass through;
b) *IR-sensitive polymer and $PC_{71}BM$* as **semi-transparent absorber** that can be used to tune the visible transmittance of solar cell devices to visibly semi-

transparent. The use of $PC_{71}BM$ can also increase the photocurrent (J_{SC}) owing to more visible absorption.

Therefore, we found that owing to the differences in absorption variation of fullerene derivatives ($PC_{61}BM$ and $PC_{71}BM$), the visibly transparency of transparent PSC can be fine tuned.

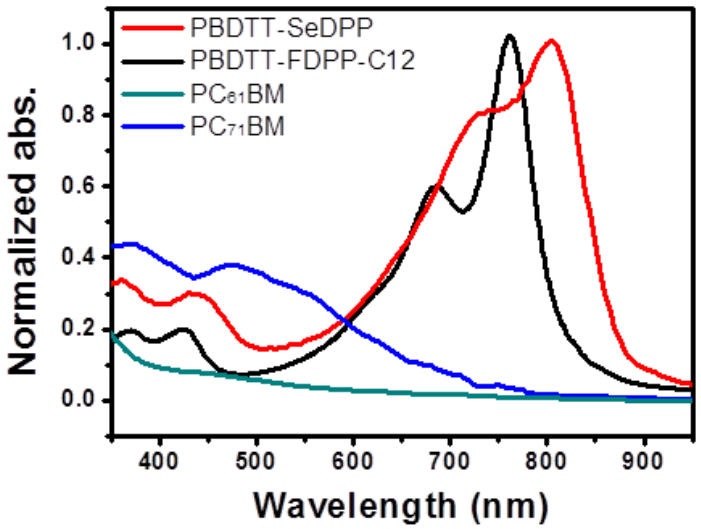

Figure 4.5 Absorption spectra of PBDTT-FDPP-C12, PBDTT-SeDPP, $PC_{61}BM$, $PC_{71}BM$.

4.7 Transmission of semi-transparent tandem 1

When building a semi-transparent PSC having a tandem structure, a major concern is the degree to which visible transparency is compensated to ensure effective IR absorption, and vice versa. In Figure 4.6, the front subcell incorporating the transparent absorber PBDTT-FDPP-C12:$PC_{61}BM$ exhibits an average visible transmission ($T_{average}$) from 400 to 650 nm of approximately 60% and an IR transmission (T_{IR}) of 52% from 650 to 800 nm. Therefore, approximately half of the IR energy was not fully captured for energy conversion in the single-junction cell, in good agreement with quantum efficiency measurements.

The back subcell featuring PBDTT-SeDPP:$PC_{61}BM$ as the absorber exhibits a similar T_{IR} of 53% with extended IR response from 650 to 900 nm. By stacking these two transparent absorbers in a tandem structure, T_{IR} dropped to 26%. In other words, the photon absorption efficiency in the IR range increased nearly twofold. The value of $T_{average}$ for the transparent tandem PSC decreased to 43% with a high maximum transparency of 51% at 550 nm—still very competitive with previously reported systems.[77, 106-110]

In terms of visual effect, semi-transparent tandem 1 was highly transmissive in the range 500–550 nm, giving a green color slightly darker than that of the transparent single-junction devices (Figure 4.8). Thus, through use of the tandem structure, the IR energy was harnessed more completely, while transmitting half of the visible photons. These optical properties make such structures viable candidates for a variety of applications requiring high efficiency and outstanding visible transmission.

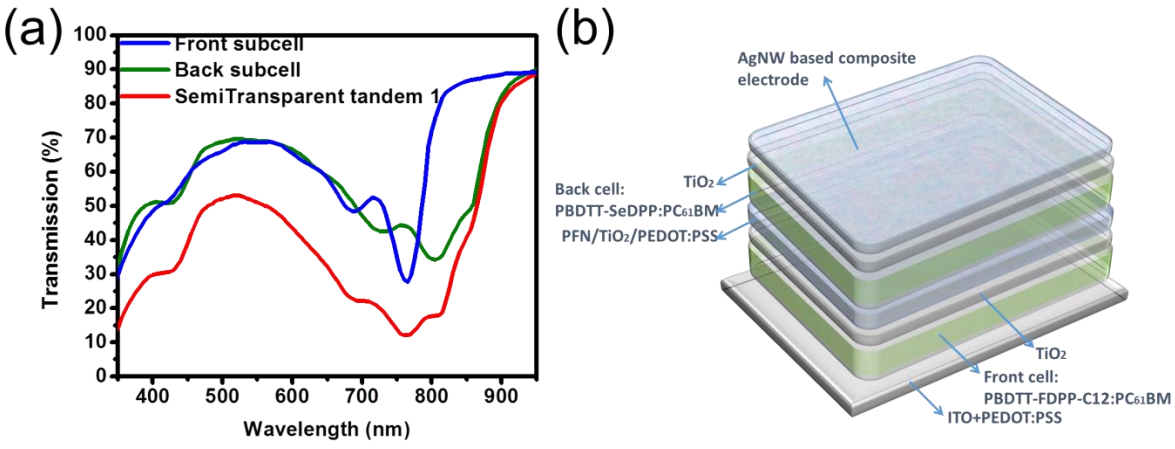

Figure 4.6 (a) Transmission spectra and (b) the device structure of semi-transparent tandem 1.

4.8 Transmission of semi-transparent tandem 2

As mentioned above, replacing $PC_{61}BM$ with $PC_{71}BM$ as the electron acceptor in the active layer allowed us to increase the photocurrent of the single-junction device. Figure 4.7 presents the transmission spectrum of $PC_{71}BM$ based polymer:fullerene blend films denoted as the back subcell. The presence of $PC_{71}BM$ in the semi-transparent absorber tuned the color of the exterior of the solar cell to a semi-transparent gray because of increasing optical absorption in the range 450–600 nm. These devices exhibited a neutral brownish color as a result of the maximal transmission band being flatter and having red-shifted to 600–650 nm. The value of $T_{average}$ (48%) was 12% lower than that of its corresponding transparent absorber.

In the design of semi-transparent tandem 2, we connected, in series, one transparent absorber as the front subcell and one semi-transparent absorber as the back subcell. This design provided us with the ability to obtain a balanced photocurrent between the two subcells, because the semi-transparent back subcell, which captured only the remaining light that passed through the front subcell, now had additional visible sensitivity to deliver a higher photocurrent matching that of the front subcell. In Figure 4.7, we observe that the transmission spectrum of the semi-transparent tandem PSC was simply the superposition of the transmission spectra of the two subcells, providing a value of $T_{average}$ of 30%.

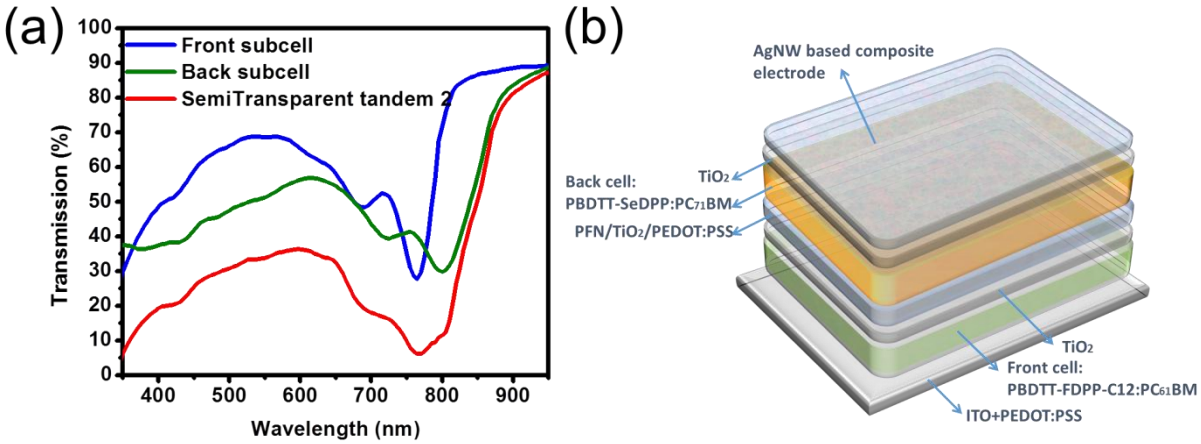

Figure 4.7 (a) Transmission spectra and (b) the device structure of semi-transparent tandem 2.

Figure 4.8 displays a photograph of the single-junction and tandem devices incorporating different absorbers with the Ag NW composite. The simple method we adapted to prepare the tandem structure allowed us to control the visible transparency and thus the color of the solar cell. In terms of their visible transparency, we obtained devices ranging from highly transparent ($T_{average}$ = 63% for the transparent absorber, single-junction device), to mildly transparent ($T_{average}$ = 48% for the semi-transparent absorber, single-junction device), to highly semi-transparent ($T_{average}$ = 43% for semi-transparent tandem 1), and finally to mildly semi-transparent ($T_{average}$ = 30% for semi-transparent tandem 2). In terms of color-tunability, the maximal transmission band could also be shifted, from 500–550 nm (greenish) to 600–650 nm (brownish). The corresponding CIE diagram is also provided in Figure 4.9. Thus, the preparation of tandem structures is an effective approach toward adjusting the optical properties of organic solar cells.

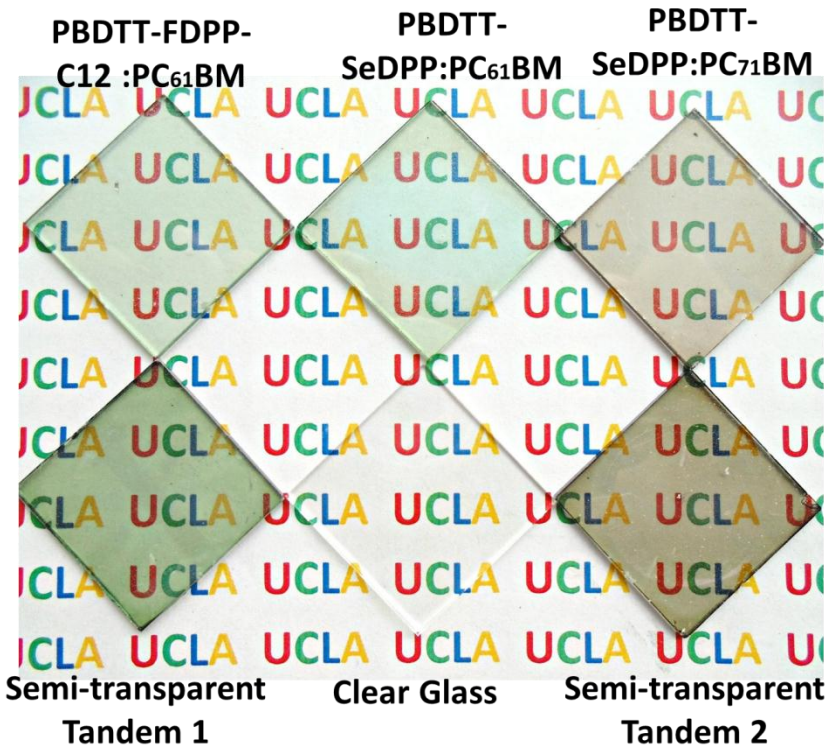

Figure 4.8 Photograph of the subcells and tandem devices, revealing their various colors and shades of gray.

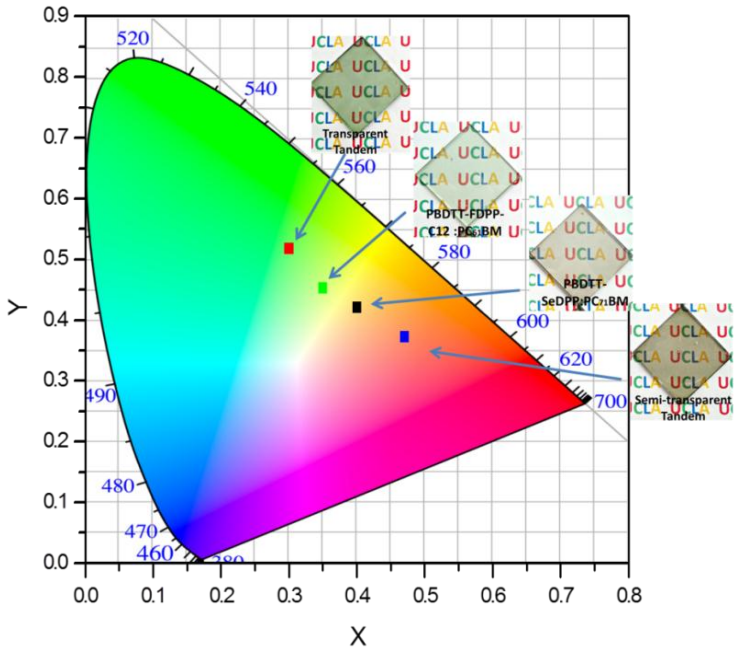

Figure 4.9 The CIE 1931 color space representing the color coordinates of different transparent and semi-transparent solar cells when illuminated with standard AM 1.5G solar spectrum.

4.9 Performance of single-junction solar cells

Prior to preparing tandem solar cells, we first evaluated the transparent (e.g., with $PC_{61}BM$) and semi-transparent (e.g., with $PC_{71}BM$) absorbers in single-junction devices. Figure 4.10a presents the structure of a single-junction device. Using a AgNW composite as the top transparent electrode, we sandwiched three different absorbers between the TiO_2 NPs and the PEDOT:PSS buffer layer. Table 4.1 summarizes the PCEs. Figure 4.10b displays the corresponding current density–voltage (*J*–*V*) curves. First, the transparent absorber prepared from PBDTT-FDPP-C12 (optical bandgap: 1.49 eV) and $PC_{61}BM$ provided a single-junction device with an optimized PCE of 4.2%. The transparent absorber prepared from PBDTT-SeDPP, which had a smaller optical bandgap of 1.38 eV, resulted in a device exhibiting a similar PCE of 4.5%, but with an improved short-circuit current density (J_{SC}) of 10.9 mA/cm^2. Hence, by decreasing the bandgap of the IR-sensitive polymers, we might, in return, expect a higher photocurrent through the harvesting of energy farther into the IR range. When combining PBDTT-SeDPP as the donor with $PC_{71}BM$ as the acceptor in the semi-transparent absorber, we improved the PCE further to 5.6%, with a value of J_{SC} as high as 13.4 mA/cm^2; this enhancement in J_{SC} arose from absorption of visible photons by $PC_{71}BM$.[13, 111]

Figures 4.10c and 4.10d present the EQEs and internal quantum efficiencies (IQEs), respectively, of the single-junction devices. In tandem solar cells, an absorber with high quantum efficiency is required to ensure complete conversion of the absorbed photons. Here, the relatively low EQE peaks presumably resulted from either limited absorption or a poor rate of charge extraction. The relatively high and constant efficiency in the IQE spectrum suggests that the limiting factor was insufficient absorption, due to its low thickness. Based on this observation,

the stacking of multiple IR-sensitive polymers with thin thickness in a tandem device should increase the absorption of the whole device while maintaining high IQE for each subcells.

Table 4.1 Device performance of single-junction PSCs incorporating different polymer blends measured with bottom-illumination.

Single-junction	V_{OC} (V)	J_{SC}(mA/cm^2)	FF (%)	PCE (%)	$T_{average}$
PBDTT-FDPP-C12:$PC_{61}BM$	0.76 (0.75)[a]	9.1 (8.6)	61 (55)	4.3 (3.6)	62
PBDTT-SeDPP:$PC_{61}BM$	0.73 (0.72)[a]	10.9 (10.2)	58 (56)	4.6 (4.1)	63
PBDTT-SeDPP:$PC_{71}BM$	0.73 (0.72)[a]	13.0 (12.5)	58 (55)	5.5 (5.0)	48

[a] Numbers in parentheses indicate average values determined from 10 devices

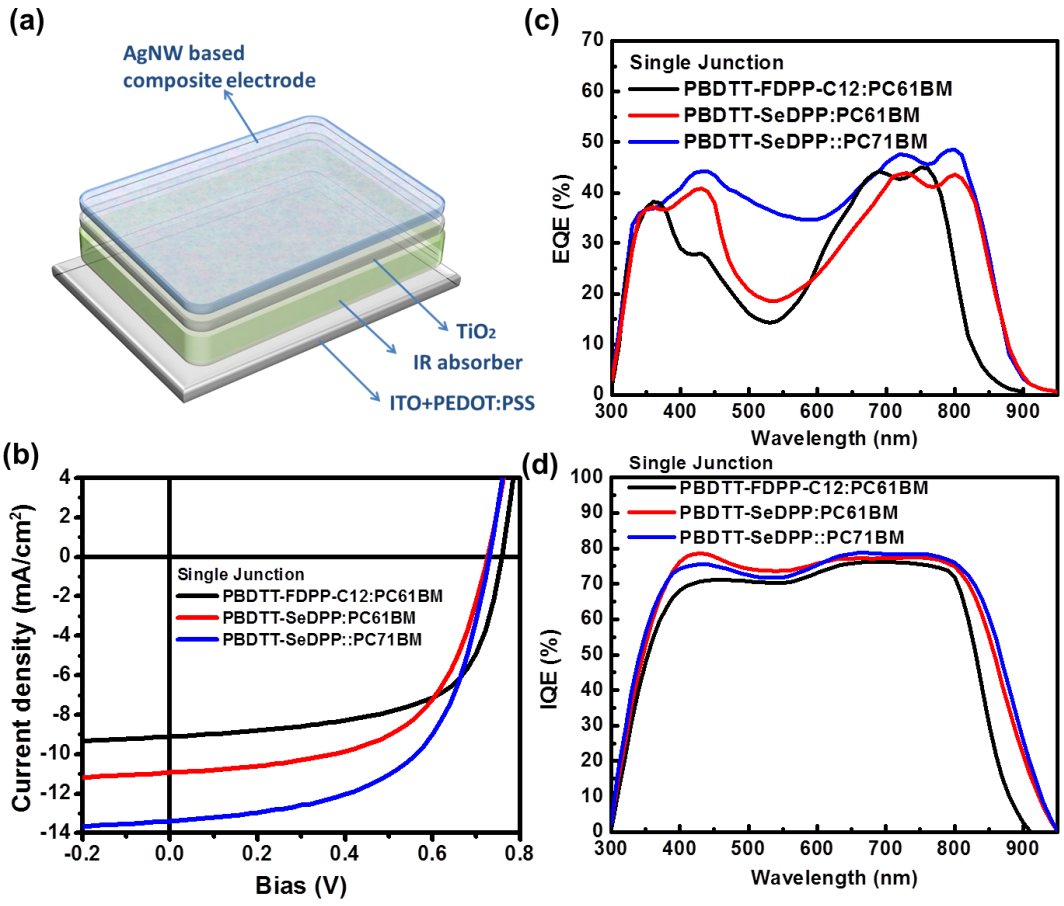

Figure 4.10 (a) Device structure, (b) *J–V* curves, (c) EQE spectra, and (d) IQE spectra of single-junction devices incorporating PBDTT-FDPP-C12:$PC_{61}BM$, PBDTT-SeDPP:$PC_{61}BM$, and PBDTT-SeDPP:$PC_{71}BM$ with AgNW top electrodes, and illuminated with standard AM 1.5 solar spectrum.

4.10 All-solution-processed interconnecting layers

Next, we employed a new design of robust interconnecting layers (ICLs), consisting of multiple interlayers of poly[(9,9-di(3,3'-N,N'-trimethylammonium)propylfluorenyl-2,7-diyl)-alt-(9,9-dioctylfluorenyl-2,7-diyl)] diiodide salt (PFN)/TiO_2/PEDOT:PSS, for low-temperature, solution processing of organic tandem solar cells. Earlier examples of ICLs have typically involved one *n*-type layer (e.g., TiO_2) serving as an electron injection interlayer and one *p*-type layer (e.g., PEDOT:PSS) serving as a hole injection interlayer.[112] In previous studies, we have found that TiO_2 may require UV light excitation for few seconds to form ohmic contact at the interface with the photoactive layer, due to a relatively low carrier density (Figure 4.11).[113] The low carrier density will form a relative wide depletion region at the contact, which is not favorable for charge tunneling. The same observation of light soaking issue of TiO_2 is also reported by Kwanghee Lee et al.[114]

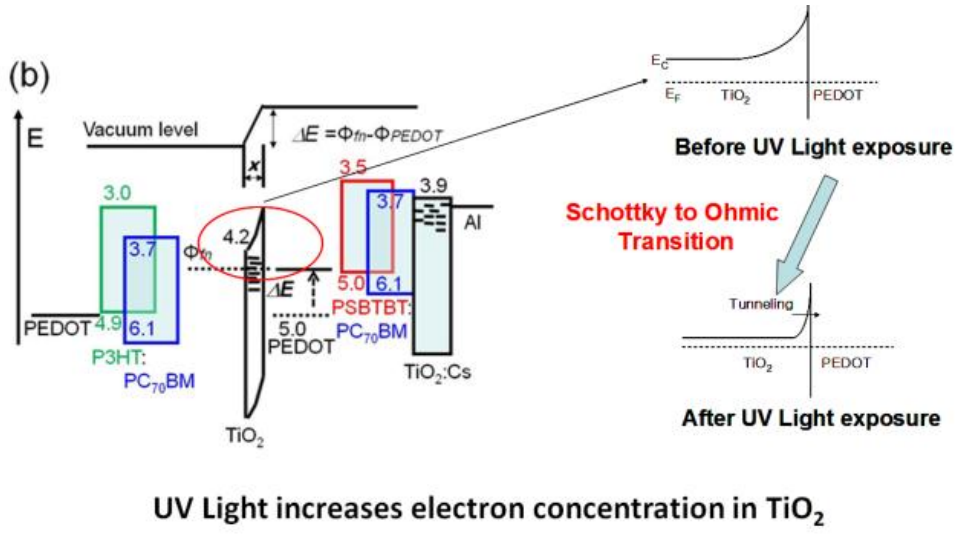

Figure 4.11 Schematic illustrating the UV soaking effect of TiO_2.[113]

Here, we used PFN, a solution-processed conjugated polyelectrolyte, to form dual electron transporting layers (dual ETL) with TiO_2 in the ICLs. PFN as an electron-transporting

layer can outperform those prepared from low-work-function metals (e.g., Ca) in single-junction devices.[105] In our ICLs, we sandwiched PFN between the polymer and TiO_2. The positively charged amino groups of PFN lead to the formation of a positive interface dipole, increase charge density, and lower the energy barrier for electron injection at interface, thereby improving the degree of electron extraction from the front subcell (Figure 4.12d). In addition, the presence of PFN can passivate the hydroxyl-terminated surfaces of metal oxides and minimize charge trapping at the interface.[115] Recently, Show-An Chen et al. used similar polymer electrolyte materials with ZnO as dual ETL and improved the performance of single-junction PSC to over 10% PCE.[14]

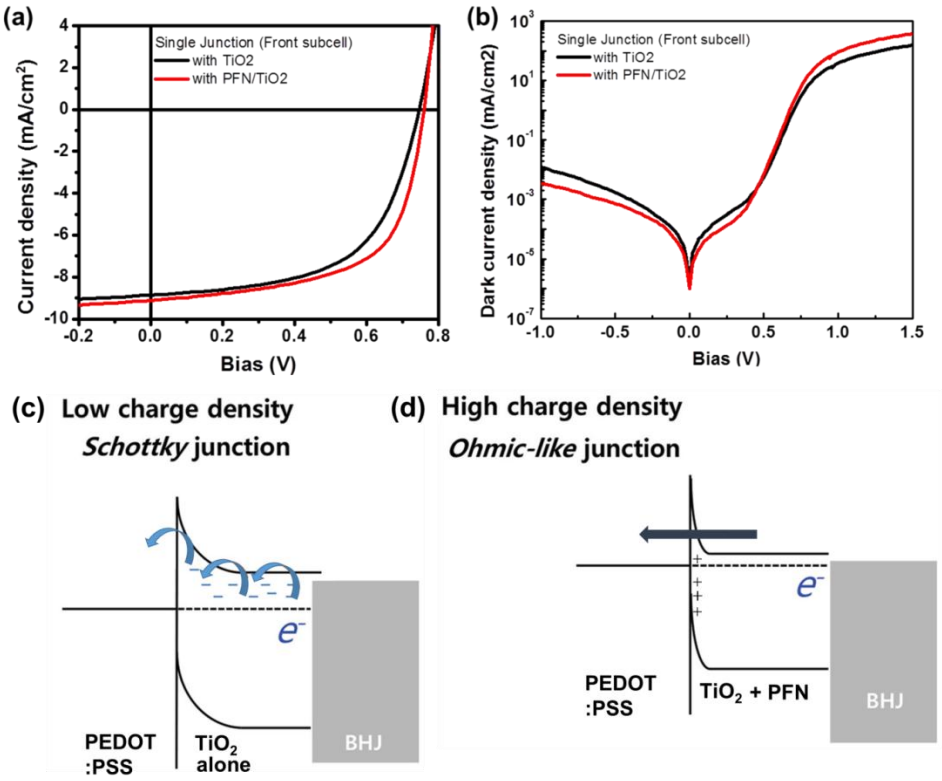

Figuer 4.12 (a) Light *J–V* curves and dark *J–V* curves of the single-junction transparent PSCs with either TiO_2 or PFN/TiO_2 double ETL layer; (c) and (d) are schematics depicting the contact barriers for electron injection via TiO_2 or PFN/TiO_2.

Similarly, the hole injection layer in our ICLs comprised two layers of distinct PEDOT:PSS formulations. For the first PEDOT:PSS layer, which came into contact with TiO_2, we chose Clevios PH1000, which has the metal-like conductivity required to form an ohmic contact with TiO_2. For the second layer of PEDOT:PSS, we employed the highly resistive formulation Clevios AI 4083 to provide a deeper work function and to minimize the energy level offset with the IR-sensitive polymer of the back subcell.[88, 116, 117] The high ratio of PSS in Clevios AI 4083 formulation also blocked electron injection and reduced the dark leakage current contributing to an improved device performance in the back subcell (Figure 4.13). This approach of dual HTL was later adapted by Frederik C. Krebs et al. to manufacture roll-to-roll printed organic tandem solar cells.[118]

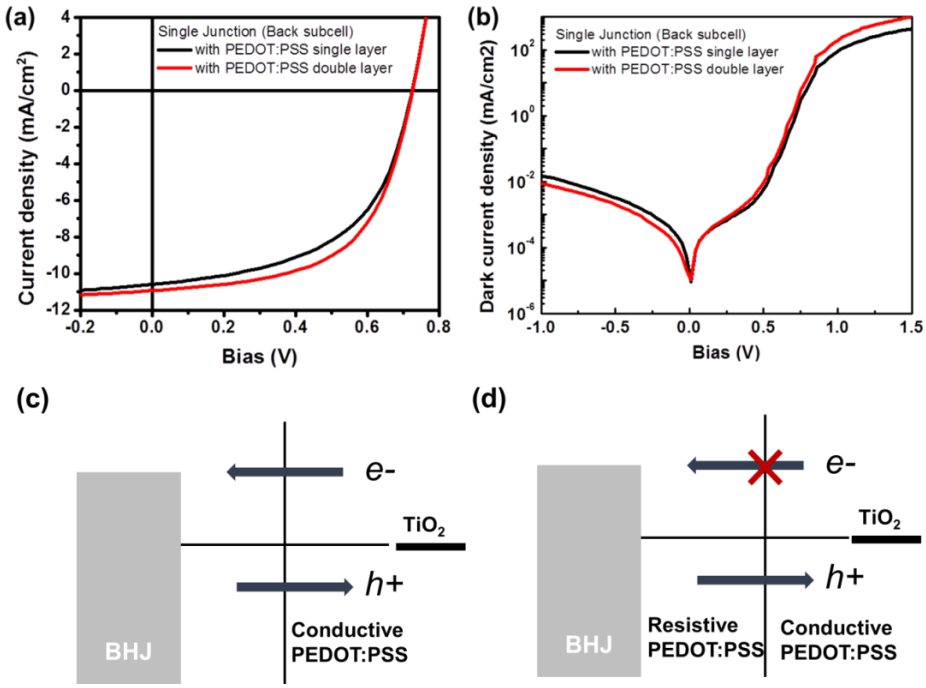

Figure 4.13 (a) Light *J–V* curves and dark *J–V* curves of the single-junction transparent PSCs with either AI4083 or AI4083/PH1000 double HTL layer; (c) and (d) are schematics depicting the contact barriers for electron injection via AI4083 or AI4083/PH1000.

Fig. 4.14 displays the energy level landscape for our present ICLs design, which we prepared through all-solution processing at low temperature requirement (ca. 100 °C).

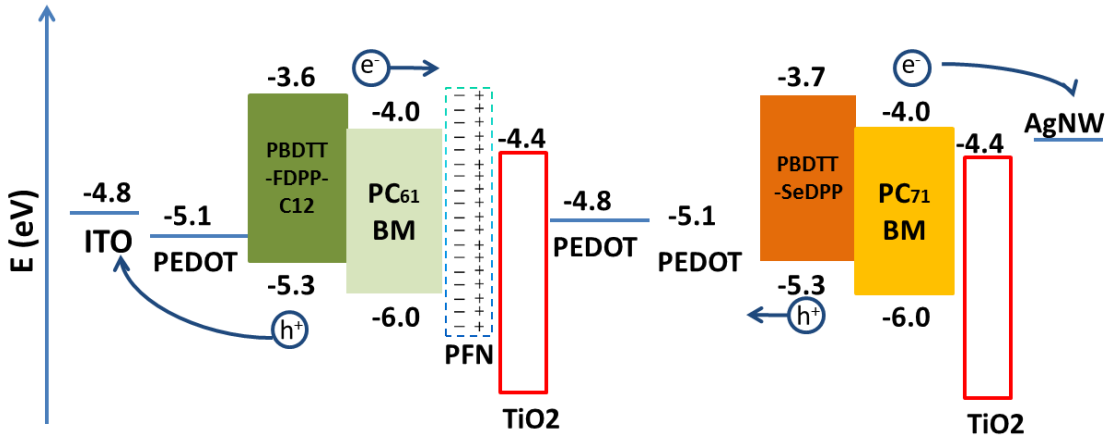

Figure 4.14 Energy level landscape of all-solution-processed, low temperature derived ICLs.

4.11 Performance evaluation of tandem solar cells

Figures 4.15 and 4.16 present the *J*–*V* curves of the semi-transparent tandem 1 and semi-transparent tandem 2 under AM1.5G illumination (100 mW/cm^2) entering from the bottom ITO electrode. For a light beam to pass through our tandem solar cell in a single journey without any interference, the optimal design to achieve high visible transparency would be a transparent tandem PSC featuring two transparent absorbers in the subcells.

Our semi-transparent tandem 1 (featuring high transparency) provided a PCE of 6.4% with a value of J_{SC} of 7.22 mA/cm^2, a value of V_{OC} of 1.46 V, and a fill factor (*FF*) of 61.2%. When we replaced the back subcell with PBDTT-SeDPP:PC$_{71}$BM, the PCE of the newly formed semi-transparent tandem 2 (featuring high performance) reached 7.3% with values of J_{SC}, V_{OC}, and *FF* of 8.41 mA/cm^2, 1.47 V, and 59.1%, respectively. Clearly, the improvement in PCE

arose from the enhancement in the value of J_{SC}. The back subcell incorporating $PC_{71}BM$ provided a higher current density to better match that of the front subcell incorporating $PC_{61}BM$.

The *FF* (59–61%) of the tandem cell is comparable with those of its corresponding single-junction subcells, indicating that an efficient series connection existed between the subcells—presumably a result of our robust polyelectrolyte-containing ICLs. In addition, the value of V_{OC} of each of our tandem cells was consistent with the sum of the values of V_{OC} of its two subcells, indicating that nearly no parasitic loss occurred as a result of the presence of the ICLs. Compared with the single-junction subcells, the tandem solar cells produced twice the voltage output at a similar current density—a potentially useful property for low-power electronics applications.[119]

Overall, the PCEs were greatly enhanced in the semi-transparent tandem 1 and semi-transparent tandem 2 structures, reaching 6.4 and 7.3%, respectively—the mark of high-performance PSCs. *J-V* characteristics are summarized in Table 4.2.

Table 4.2 Device performance of double-junction tandem PSCs possessing various subcell configurations, measured with bottom-illumination.

Double-junction Tandem		V_{OC} (V)	J_{SC}(mA/cm^2)	*FF*(%)	PCE(%)	$T_{average}$
Front subcell	Back subcell					
PBDTT-FDPP-C12:$PC_{61}BM$	PBDTT-SeDPP:$PC_{61}BM$	1.46 (1.45)[a]	7.2 (6.9)	61 (56)	6.4 (5.8)	43
PBDTT-FDPP-C12:$PC_{61}BM$	PBDTT-SeDPP:$PC_{71}BM$	1.47 (1.46)[a]	8.4 (8.0)	59 (55)	7.3 (6.6)	30

[a] Numbers in parentheses indicate average values determined from 10 devices

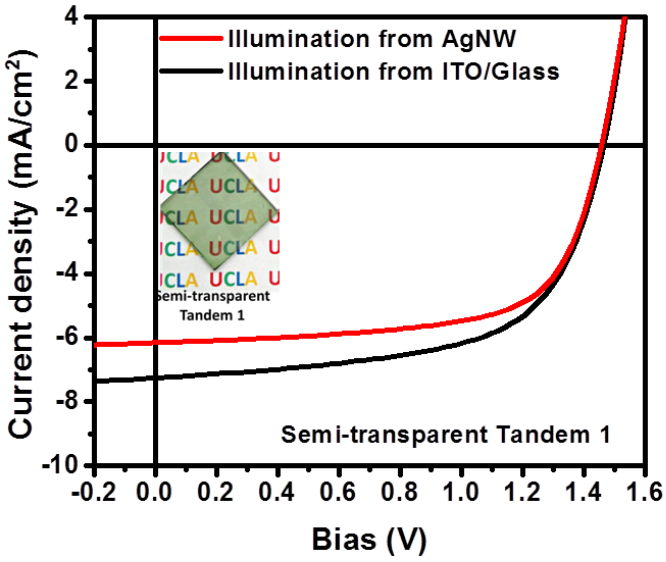

Figure 4.15 Light *J–V* curves of the semi-transparent tandem 1 device, illuminated from AgNW side and ITO/glass side.

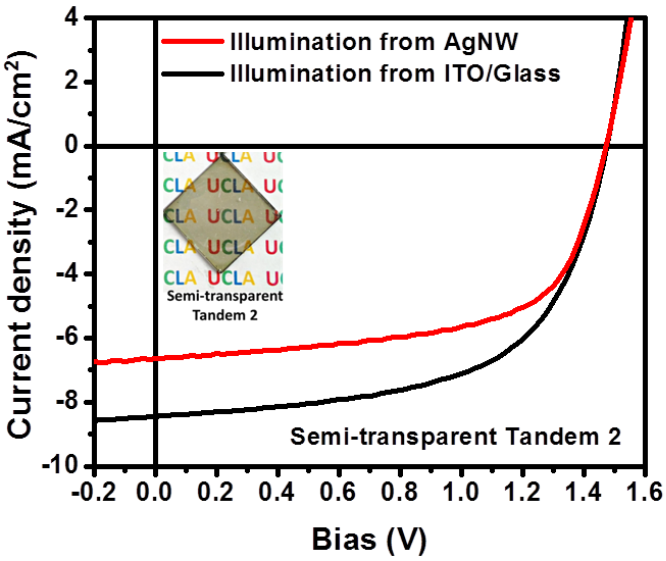

Figure 4.16 Light *J–V* curves of the semi-transparent tandem 2 device, illuminated from AgNW side and ITO/glass side.

4.12 Top side harvesting capability

Likewise, we recorded the *J–V* curves of the tandem solar cells when illuminating from the top (from the AgNW electrode). For the semi-transparent tandem 2 device that exhibited a

PCE of 7.3% when illuminated from the bottom (from the ITO/glass), we measured a PCE of 6.1% with a value of J_{SC} of 6.65 mA/cm^2 when illuminated from the top.

Similarly, the semi-transparent tandem 1 cell that provided a PCE of 6.4% when illuminated from the bottom exhibited a PCE of up to 5.7% when illuminated from the top. We ascribe the loss of output current to unbalanced current generated from the subcells. In the top-illumination setup, light was first harnessed by the back subcell, leaving the unharnessed energy for the front subcell to utilize.

Because we originally designed the front subcell absorber to exhibit a lower photocurrent output, the performance of the tandem PSC, limited by the front subcell, would result in a lower photocurrent. We also found that the tolerance (insensitivity) toward the illumination direction of the semi-transparent tandem 1 device was better than that of the semi-transparent tandem 2 device. Despite the differences in photocurrent upon changing the illumination direction, our results suggest that these tandem solar cells have great potential for use with top-, bottom-illumination, or both.[120, 121]

4.13 External quantum efficiency measurement

We measured the EQEs of the subcells in the tandem structure to ensure the accuracy of our measurements of device performance. Here, we simulated the EQE of only the back subcell, assuming that the performance of the front subcell was almost identical to that of its analogous single-junction device. The front subcells in the tandem devices received no optical interference from the back subcells; therefore, their performances were similar to those of the corresponding single-junctions devices. Here, we simulated the EQE spectra of the back subcells by measuring the single-junction devices with a layer of front-subcell material—serving as an optical filter—

coated on the back of the ITO/glass. The details of the experimental setup and results are provided as following:

a) Figure 4.17 (a): EQE spectra of PBDTT-SeDPP:$PC_{61}BM$ in the single-junction device with coating of PBDTT-FDPP-C12:$PC_{61}BM$ to mimic the back subcell in the semi-transparent tandem 1 device under ITO/glass illumination
b) Figure 4.17 (b): EQE spectra of PBDTT-SeDPP:$PC_{71}BM$ in the single-junction device with coating of PBDTT-FDPP-C12:$PC_{61}BM$ to mimic the back subcell in the semi-transparent tandem 2 device under ITO/glass illumination
c) Figure 4.17 (c): EQE spectra of PBDTT-FDPP-C12:$PC_{61}BM$ in the single-junction device with coating of PBDTT-SeDPP:$PC_{61}BM$ to mimic the front subcell in the semi-transparent tandem 1 device under AgNW illumination.
d) Figure 4.17 (d): EQE spectra of PBDTT-FDPP-C12:$PC_{61}BM$ in the single-junction device with coating of PBDTT-SeDPP:$PC_{71}BM$ to mimic the front subcell in the semi-transparent tandem 2 device under AgNW illumination.

For the semi-transparent tandem 1 device, we simulated the back subcell absorber (PBDTT-SeDPP:$PC_{61}BM$) and calculated a value of J_{SC} of 7.0 mA/cm^2 from the EQE curve; this result is close to the value of 7.2 mA/cm^2 that we measured from the *J*–*V* curve (Figure 4.17a). Using the same method to analyze the semi-transparent tandem 2 cell featuring PBDTT-SeDPP:$PC_{71}BM$ in the back subcell, we calculated a value of J_{SC} (ca. 8.1 mA/cm^2) from the EQE curve, in good agreement with that (8.3 mA/cm^2) measured from the *J*–*V* curve (Figure 4.17b). These results reveal that the back subcell was the factor limiting the performance of the tandem solar cells when illuminated from the bottom ITO. The same measurement is also carried for simulating the top-illumination condition where the light is entering from AgNW side. In this

condition, the light will enter back subcell (PBDTT-SeDPP:$PC_{61}BM$) first. The front subcell (PBDTT-FDPP-C12:$PC_{61}BM$) is now having optical interference, thus we characterize front subcell instead. These results are shown in Figures 4.17c and 4.17d.

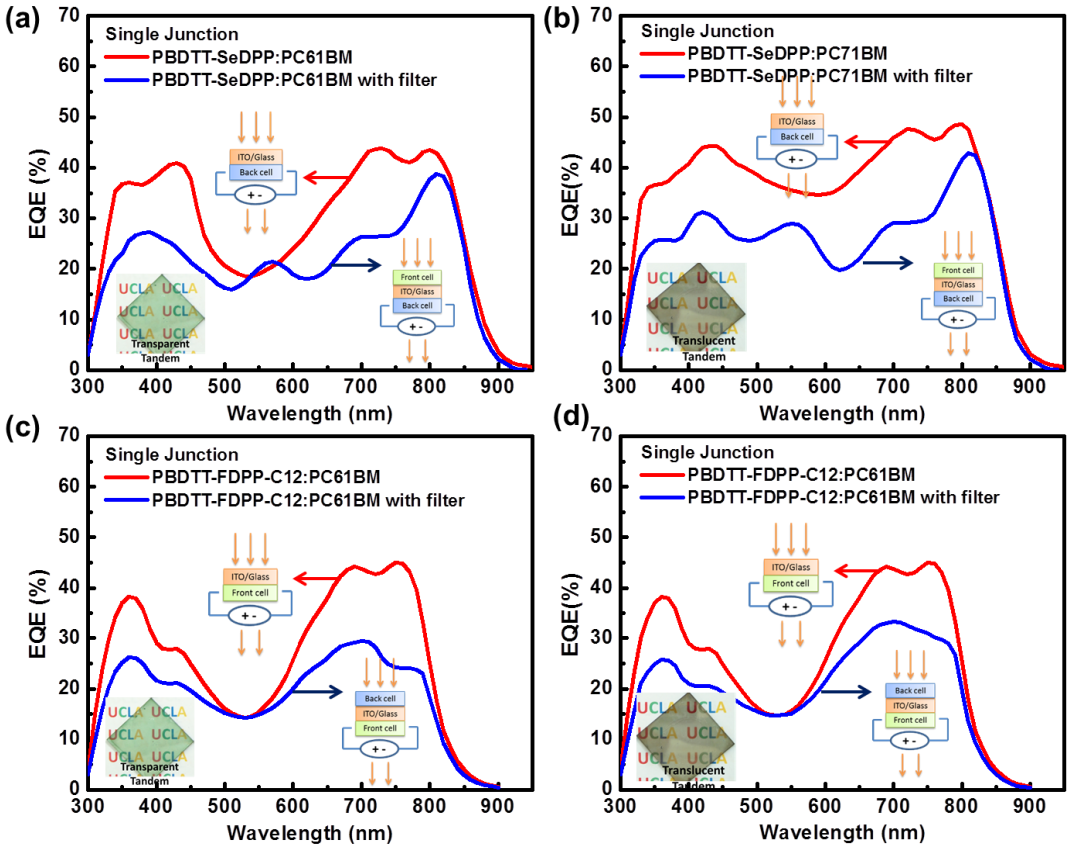

Figure 4.17 EQE spectra of single-junction devices mimicking (a, b) the back subcells in the (a) semi-transparent tandem 1 and (b) semi-transparent tandem 2 devices under bottom-illumination and (c, d) the front subcells in the (c) semi-transparent tandem 1 and (d) semi-transparent tandem 2 under top-illumination.

4.14 Summary

In tandem structures, we have constructed high-performance semi-transparent PSCs possessing effective tandem architectures. The two subcells in tandem devices are connected by a new solution-processed, low-temperature processed ICLs featuring low ohmic loss achieved by

embedded interface dipoles using PFN/TiO_2/PEDOT:PSS/PEDOT:PSS. By synthesizing a new polymer of PBDTT-FDPP-C12, we could enlarge energy bandgap and narrow the absorption band of IR polymer used in the front subcell, thereby creating a small spectrum mismatch between two IR polymers used for front and back subcells in the tandem PSC.

Given two transparent absorbers (IR-sensitive polymers:$PC_{61}BM$) in the subcells, we obtained semi-transparent tandem 1 devices optimized for visible transparency, along with improved efficiency: an average PCE of 6.4% under AM1.5G illumination with a maximum transmission of 51% at 550 nm and a value of T_{average} of 43%.

Given one semi-transparent absorber (IR-sensitive polymers:$PC_{71}BM$) in the back subcell, semi-transparent tandem 2 devices were introduced. This design optimized for efficiency could achieve a PCE of 7.3% with T_{average} of 30%. Furthermore, we have also demonstrated that these tandem solar cells can be used in either top- or bottom-illumination modes without any major differences in their device performances.

Finally, with judicious choice of the donor and acceptor materials, the preparation of tandem structures can also be used to adjust the external appearance of PSCs from greenish (transmission maxima at 500–550 nm) to a shade of gray (transmission maxima at 600–650 nm). These results suggest that tandem structures can refine the optical and electronic properties of transparent photovoltaic devices allowing their implementation in a diverse range of optical applications—from windows to privacy screens to structural accents in future architectural designs.

Chapter 5 Design of Inverted-Structure Organic Tandem Solar Cells

5.1 Introduction

Organic solar cells have been the subject of much research interest over the past decade.[15, 122] A major attraction of organic solar cells is that their solution-based fabrication can allow the formation of multiple layers with rapid, continuous roll-to-roll printing.[123-125] To date, organic single-junction solar cells based on narrow bandgap materials (E_g < 1.7 eV) have exhibited power conversion efficiencies (PCEs) exceeding 7%.[126] Nonetheless, single-junction PSCs usually suffer from the two inherent disadvantages:

1) Limited absorption range, which restricts the utilization of the full solar spectrum;[127]
2) Relatively low carrier mobility, which requires the use of thinner films for efficient charge extraction and compromises the effective absorption.[128]

Thus, the external quantum efficiency (EQE) of PSC usually is below 80% and photocurrent (J_{SC}) rarely goes beyond 20 mA/cm^2 for single-junction PSCs. In Figure 5.1, F. C. Krebs et al. summarized the J_{SC} and PCE values from the recent reported literatures. [129]

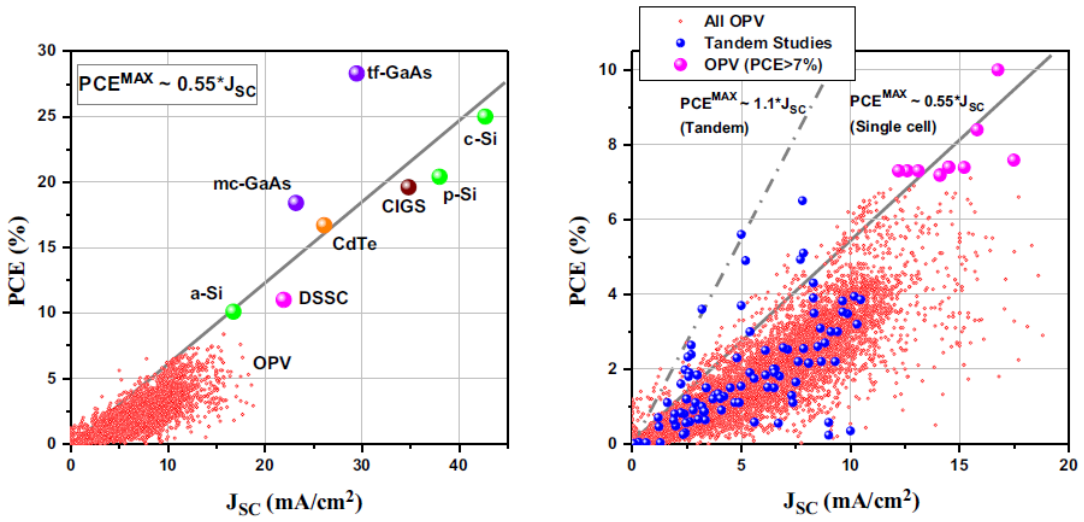

Figure 5.1 A plot of reported OPV efficiency *vs.* J_{SC} in comparison to other inorganic solar cell competitors up to 2014. Due to limited J_{SC}, the reported PCE for OPV is 10% or less.[129] Copyright © 2014 Elsevier B.V.

To utilize solar radiation more effectively, one possible solution is to stack multiple photoactive layers with complementary absorption in series to make a tandem PSC. Typically, a successive tandem structure consists of a front subcell, interconnecting layer (**ICL**), and a back subcell.

a) The front subcell usually requires its absorber to have wide bandgap (E_g > 1.7 eV). **P3HT** (E_g ~ 1.9 eV),[130] is one of the most frequently used front subcell material due to its excellent thermal stability reducing the processing difficulties. The other promising wide bandgap polymers reported with tandem applications are **PCDTBT (**E_g ~ 1.9 eV),[131] and **PFTBT (**E_g ~ 1.95 eV).[132]

b) The back subcell usually needs the low bandgap (E_g < 1.5 eV). **PCPDTBT** (E_g ~ 1.46 eV),[56] **PSBTBT** (E_g ~ 1.45 eV),[112] and **pBBTDPP2** (E_g ~ 1.40 eV),[133] have been applied into tandem solar cells as back subcell. The corresponding chemical structures are shown in Figure 5.2.

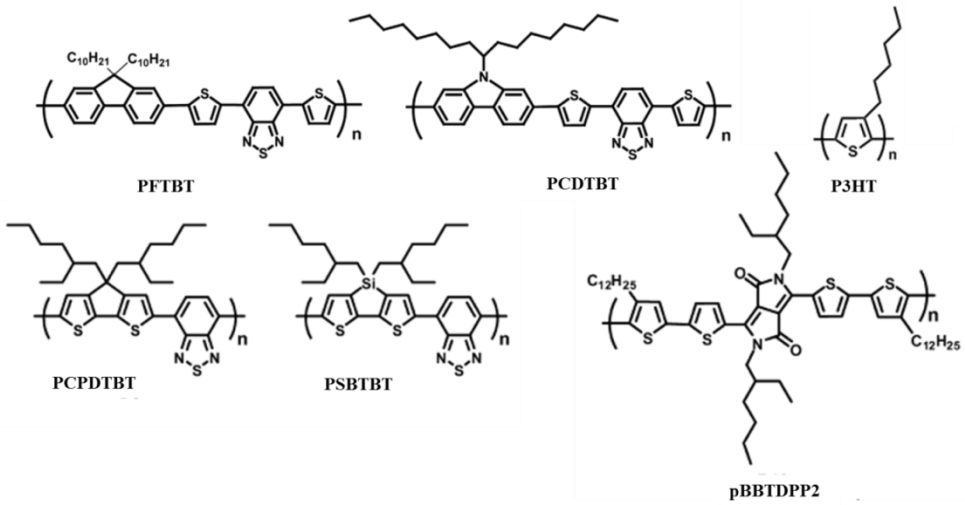

Figure 5.2 The chemical structures of commonly used wide-bandgap and low-bandgap polymers in double-junction tandem structures.

In Chapter 5, we introduce three polymers to be incorporated into the double-junction structure. P3HT (E_g = 1.9 eV) is used as wide-bandgap donor, PTB7-Th (E_g = 1.58 eV) is used as medium-bandgap donor, and PDTP-DFBT (E_g = 1.4 eV) is used as low-bandgap donor. Depending on the combination of energy bandgaps in the front and back subcells, three different double-junction tandem solar cells can be employed to explore the spectrum overlapping and current matching issues inside the organic tandem solar cells.

In Chapter 6, we introduce the triple-junction structure using the three aforementioned polymers (P3HT, PTB7-Th, PDTP-DFBT). The study of different double-junction tandem configurations here are critical in realizing the triple-junction solar cells.

5.2 Device structure

In Figure 5.3, different double-junction configurations can be visualized as a part of triple-junction solar cells. Configuration 1, featuring P3HT and PTB7-Th (hereafter denoted as **PTB**) as the donors in the subcells, can be seen as the bottom portion (E_{g1}, E_{g2}) of the triple-

junction tandem cell, assuming no optical coupling from the back subcell (E_{g3}). Configuration 2, featuring PTB and PDTP-DFBT (hereafter denoted as **LBG**) as the donors in the front and back subcells, can be seen as the top portion (E_{g2}, E_{g3}) of the triple-junction tandem cell. Configuration 3, featuring P3HT and LBG as donors in the subcells, is the case in which the middle junction (E_{g2}) is absent in triple-junction tandem cell.

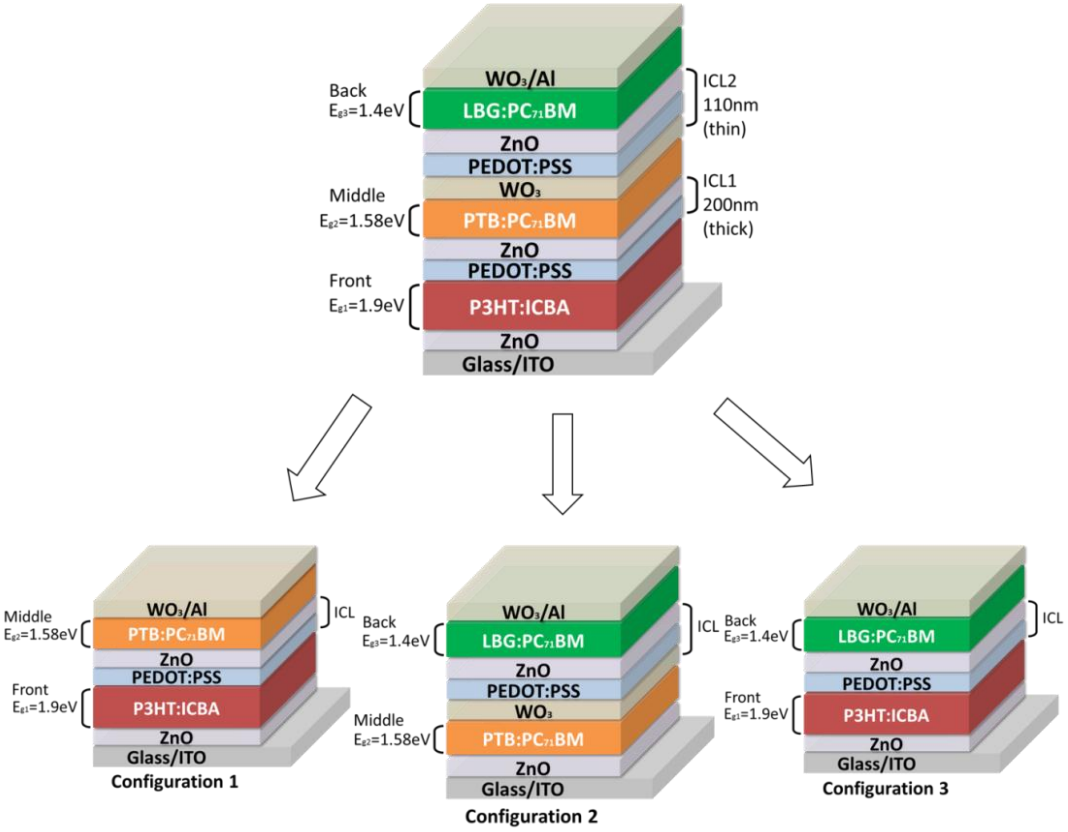

Figure 5.3 Device configurations (front subcell/back subcell) of double-junction tandem solar cells in the inverted architecture. Configuration 1: P3HT:ICBA/PTB:$PC_{71}BM$; configuration 2: PTB:$PC_{71}BM$/LBG:$PC_{71}BM$; configuration 3: P3HT:ICBA/LBG:$PC_{71}BM$.

5.3 Material and device fabrication

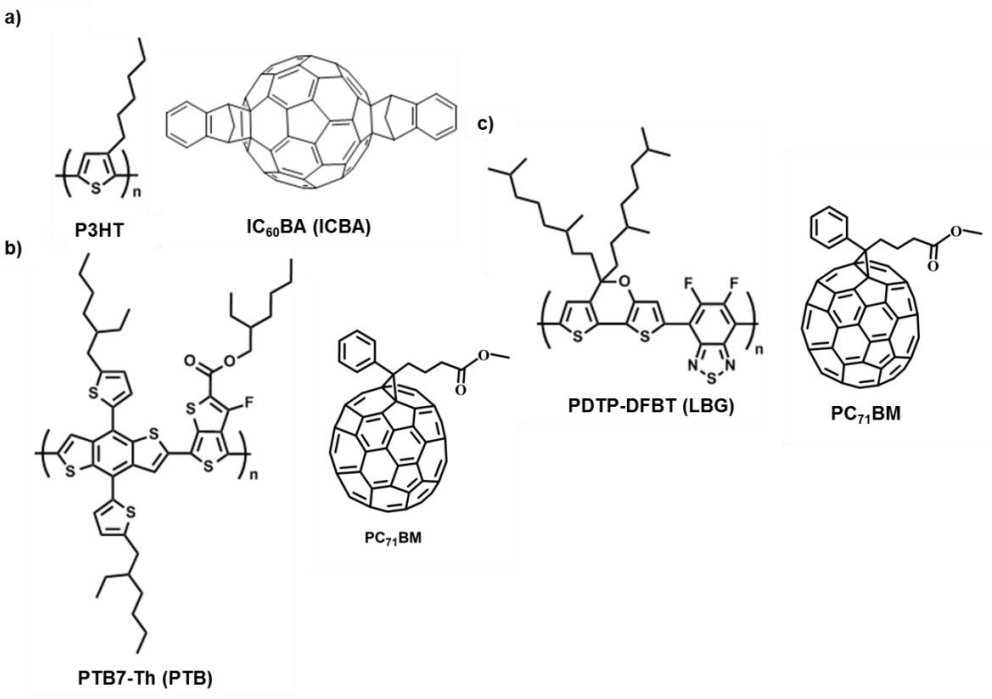

Figure 5.3 Chemical structures of the polymer:fullerene blends used in the double-junction polymer solar cell in which (a) P3HT:ICBA, (b) PTB7-Th:$PC_{71}BM$, and (c) PDTP-DFBT:$PC_{71}BM$.

Solution preparation and coating recipe: The polymer PTB7-Th (hereafter known as PTB) was synthesized according to a previously reported method.[134] The polymer P3HT and PDTP-DFBT (hereafter known as LBG) were received from Rieke Metals and Sumitomo Chemical Co., Ltd, respectively. P3HT:ICBA (1:1) were dissolved in dichlorobenzene at a concentration of 20 mg mL^{-1} and spin-coated at 700 rpm (200 nm) or 850 rpm (160 nm).[135] LBG:$PC_{71}BM$ (1:2) were dissolved in dichlorobenzene with a concentration of 8 mg mL^{-1} and spin-coated at 2000 rpm (100 nm) or 3000 rpm (85 nm). PTB:$PC_{71}BM$ (1:1.5) were dissolved in 97% chlorobenzene with 3% 1,8-diiodooctane, DIO, at a concentration of 10 mg mL^{-1} and spin-coated at 1400 rpm (110 nm) or 1500 rpm (100 nm).[11] The PEDOT:PSS (Clevios PH500) was modified with the addition of 5% dimethylformamide, DMF, and 5% poly(styrene sulfonate),

PSS, from 10 wt.% solution in H_2O, and 1% Zonyl FSO fluorosurfactant and spin-coated at 4000 rpm (80 nm) or 2000 rpm (160 nm). Stable, OH-free ZnO nanoparticles were synthesized using the hydrothermal method and spin-coated at 2500 rpm (40 nm) or 4000 rpm (20 nm).[136] WO_3 nanoparticles (2 wt.% in EtOH, nanograde) were used as received.

Double-junction tandem fabrication: ZnO nanoparticles were spin-coated on ITO substrates and annealed at 150 °C for 60 s to form a 20-nm-thick condensed layer. The active layer of the front subcell was then spin-coated on the ZnO surface. For P3HT:ICBA as the front subcell, thermal annealing treatment at 150 °C for 10 min was applied. For PTB:$PC_{71}BM$ as the front subcell, the sample was left idle for 1 h in a glove box before an additional layer of WO_3 nanoparticles was spin-coated to form a 10-nm buffer layer. Next, 50 mL PEDOT:PSS was drop-casted on the rotating samples to form a 150-nm-thick layer and baked for 150 °C for 10 min (on top of P3HT:ICBA) or 100 °C for 10 s (on top of PTB:$PC_{71}BM$). Drop-casting can reduce the exposure time to water and minimize the unwanted moisture damage. A 20-nm-thick ZnO layer was deposited using the previous solution; and the sample was annealed at 100 °C for 30 s. The active layer of the back subcell was spin-coated on the ZnO surface. Finally, a 20-nm-thick WO_3 layer was deposited on the back subcell using the same solution, and then 100-nm-thick Al was deposited through thermal evaporation. All steps were carried out inside N_2-filled glovebox.

Device characterization: The *J–V* characteristics of the photovoltaic cells were recorded using a Keithley 2400 source measure unit under a simulated AM1.5G spectrum with an Oriel 9600 solar simulator, adjusted using a monocrystalline silicon solar cell equipped with a KG5 filter and calibrated by the National Renewable Energy Laboratory (NREL). During measurements, to avoid parasitic current, each device (fingers) was absolutely isolated by

scratching the films surrounding the devices and measured with a 0.1 cm^2 mask. EQE measurements were taken using an integrated system (Enlitech, Taiwan) and a lock-in amplifier with a current preamplifier under the short-circuit conditions. The light spectrum was calibrated using a monocrystalline photodetector of known spectral response. Light bias of 550, 650, and 800 nm was selected to excite the front, middle, and back subcells in the tandem devices.[137] The unexcited subcell was then measured using a Xe lamp passing through a monochromator with a typical intensity of 10 μW. The optical parameters *n* and *k* were obtained through spectroscopic ellipsometry. Energy levels were obtained through UPS measurements performed within an Omicron XPS/UPS system.

5.4 Medium-bandgap polymer: PTB7-Th

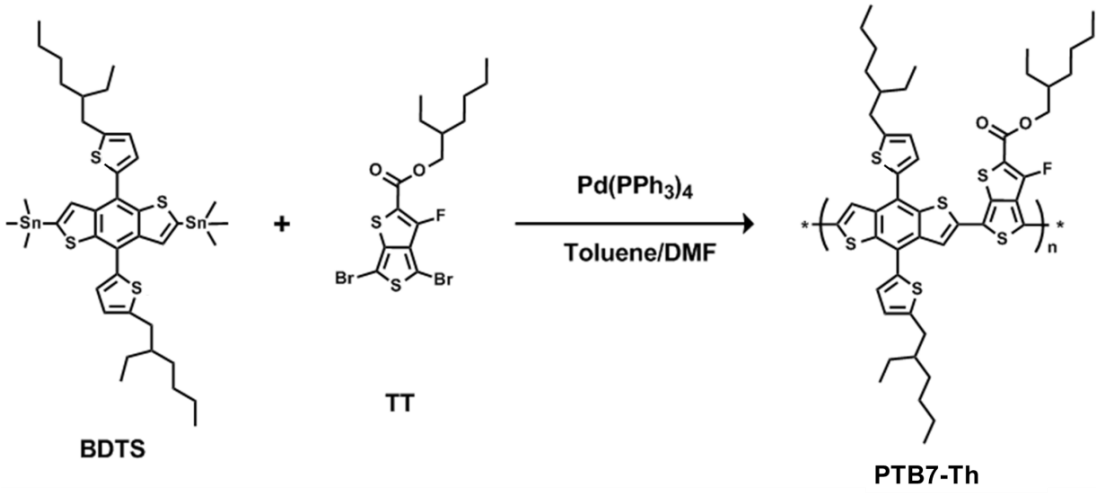

Figure 5.4 Synthetic route to PTB7-Th.

Synthesis of PTB7-Th: All monomers were synthesized according to reported methods.[134, 138] PTB7-Th is also known as PBDTTT-EFT. Figure 5.4 shows the polymerization of PTB7-Th. BDTS (0.2496 g, 0.2504 mmol), TT (0.1185g, 0.2509 mmol) were dissolved into 7.5 mL anhydrous toluene and 1.5 mL anhydrous DMF in a flask protected by argon. The solution was

flushed with argon for 10 minutes, then 14.5 mg of $Pd(PPh_3)_4$ was added into the flask. The solution was flushed with argon again for another 10 minutes. The oil bath was heated to 105 ºC gradually, and the reaction mixture was stirred for 10 hours at 105 ºC under argon atmosphere. Then, the mixture was cooled down to room temperature and the polymer was precipitated in ~100 mL methanol and the precipitated solid was collected. The crude polymer was subjected to soxhlet extraction by methanol (6 h), hexane (12 h), and acetone (6 h). Finally, the polymer was purified by silica gel chromatography using chloroform as eluent and then slowly precipitated in ~75 ml acetone. The polymer was collected as dark green-black solid, yield 30%. The polymer can be readily dissolved into chloroform, chlorobenzene or dichlorobenzene, etc**.** GPC result: Mn=16.0 k; polydispersity=2.2.

5.5 Low-bandgap polymer: PDTP-DFBT

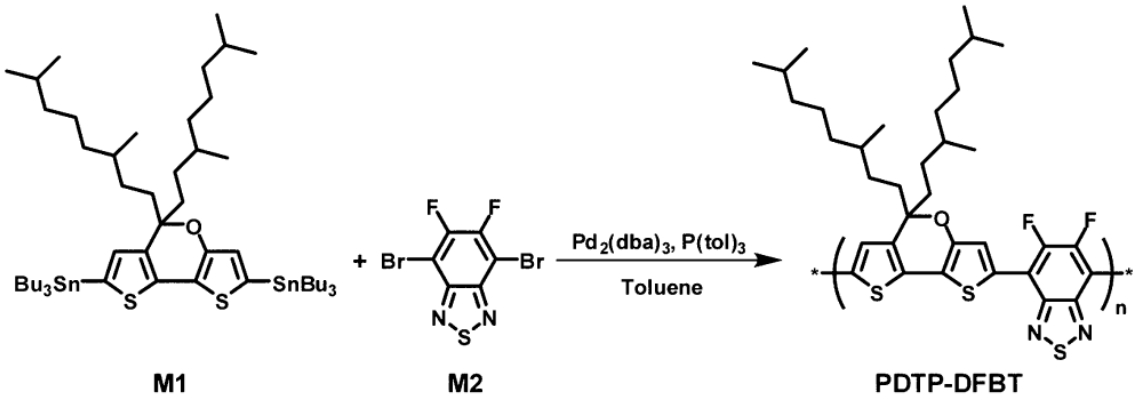

Figure 5.5 Synthetic route to PDTP-DFBT.

Synthesis of PDTP−DFBT: All monomers (M1 and M2) were synthesized according to reported methods.[139] Figure 5.5 shows the polymerization of PDTP-DFBT. M1 (0.431 g, 0.410 mmol) and M2 (0.131 g, 0.397 mmol) were dissolved into 20 mL of toluene in a flask protected by argon. The solution was flushed with argon for 10 min, and then 7 mg of $Pd_2(dba)_3$ and 14 mg of $P(o\text{-}tol)_3$ were added into the flask. The oil bath was heated to 100 °C gradually, and the

reaction mixture was stirred for 4 h at 100 °C under an argon atmosphere. The 400 mg of bromobenzene was added, and the mixture was stirred for 4 h. Then, the mixture was cooled down to room temperature, and the polymer was precipitated in 100 mL of methanol and the precipitated solid was collected. Low molecular weight portion was removed by Soxhlet extraction using acetone (6 h) and hexane (12 h). The polymer was further purified by silica gel chromatography using chlorobenzene as eluent. Then the polymer was precipitated in 100 mL of methanol and obtained as dark purple solid; yield ~70%. The polymer can be dissolved chlorobenzene or dichlorobenzene, etc. ^{1}H NMR (400 MHz, $CDCl_3$): d = 6.8−7.8 (br, 2H), 0.6−2.0 (br, 42H). Mn = 28.5 kDa; polydispersity = 2.2.

5.6 Optical absorption

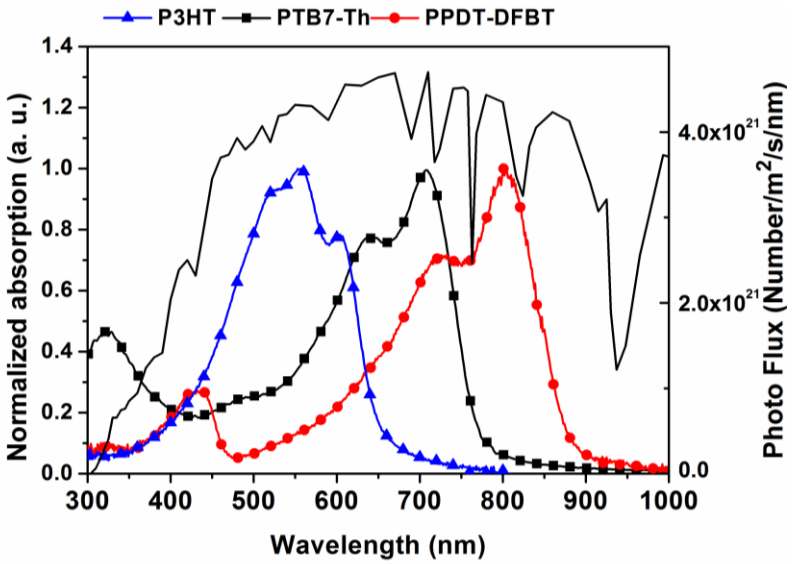

Figure 5.6 Normalized absorption spectra of the polymers used in the study.

Figure 5.6 presents the normalized absorption spectra of the absorber materials tested in this study. In double-junction tandem structure, the mismatched absorption spectra between the polymer absorber materials are favorable for generating high photocurrent gain in tandem

structure. Since there are only two subcells in this tandem design, the optical interference effect can be simplified for study.

In the configuration 1, double-junction tandem, P3HT, the front subcell (E_{g1}) donor and PTB, the middle subcell (E_{g2}) donor are selected. Since both P3HT (E_{g1} = 1.9 eV) and PTB (E_{g2} = 1.58 eV) have an absorption window for visible light that extends to 650 nm and 800 nm respectively, their absorption spectra is mismatched by 150 nm which may not be sufficiently enough.

In the configuration 2, double-junction tandem, PTB, the middle subcell (E_{g2}) donor and LBG, the back subcell (E_{g3}) donor are selected. Since PTB (E_{g2} = 1.58 eV) has an absorption window for visible light that extends to 800 nm and LBG (E_{g3} = 1.4 eV) has sensitivity to near-IR photons up to 950 nm, their absorption spectra is also mismatched by 150 nm.

In the configuration 3, double-junction tandem, P3HT, the front subcell (E_{g1}) donor and LBG, the back subcell (E_{g3}) donor are selected. Since P3HT (E_{g1} = 1.9 eV) has an absorption window for visible light that extends to 650 nm and LBG (E_{g3} = 1.4 eV) has sensitivity to near-IR photons up to 950 nm, their absorption spectra are complementary and the difference in bandgap is 0.5 eV.

5.7 Photovoltaic performance of single-junction cells

To understand the photovoltaic properties of various polymeric absorbers, we first studied single-junction configurations featuring these donor materials. In a double-junction tandem cell, the subcells in the back are operating under reduced light conditions because the high energy photons of the incident light are harvested first by the subcells in the front.

Therefore, much higher photocurrent densities are required for the back and middle subcells (E_{g3}, E_{g2}) to avoid their becoming the current-limiting subcells.

Figure 5.7 presents the photocurrent density–voltage (*J*–*V*) curves measured under standard AM1.5G solar illumination for P3HT:ICBA, PTB:$PC_{71}BM$, and LBG:$PC_{71}BM$ in single-cell configurations. Table 5.1 summarizes their detailed performance parameters. As the bandgap energy of a donor decreases, the short-circuit current density (J_{SC}) increases in response to more photons being harvested at longer wavelengths. Here, we observed an improvement in the values of J_{SC} from 9.9 mA·cm^{-2} for P3HT, to 14.5 mA·cm^{-2} for PTB, and to 17.5 mA·cm^{-2} for LBG. This consistent improvement in the values of J_{SC} resulted from the comparable and high external quantum efficiencies (EQEs) of the individual cells.

Figure 5.8 displays EQE measurements of single cells of P3HT:ICBA, PTB:$PC_{71}BM$, and LBG:$PC_{71}BM$ prepared with optimized thicknesses of 200, 100, and 100 nm, respectively. The maxima in the EQE spectra of the PTB- and LBG-based cells (ca. 67% and 64%, respectively) were comparable with that of the P3HT-based cell (65%). Thus, while donor materials with decreasing bandgap energies are crucial for a tandem design, comparably high EQEs are also required to ensure that the broader spectral response can be transformed efficiently into additional charge carriers.

Table 5.1: Properties of single-junction cells (ITO/ZnO/active layer material/anode).

Active Layer	**Anode**	V_{OC} **(V)**	J_{SC} **(mA·cm^{-2})**	***FF***	**PCE (%)**
P3HT:ICBA	PEDOT:PSS/Al	0.84	9.93	69.23	5.79
PTB:$PC_{71}BM$	WO_3/Al	0.78	14.51	67.81	7.68
LBG:$PC_{71}BM$	WO_3/Al	0.70	17.49	64.35	7.82

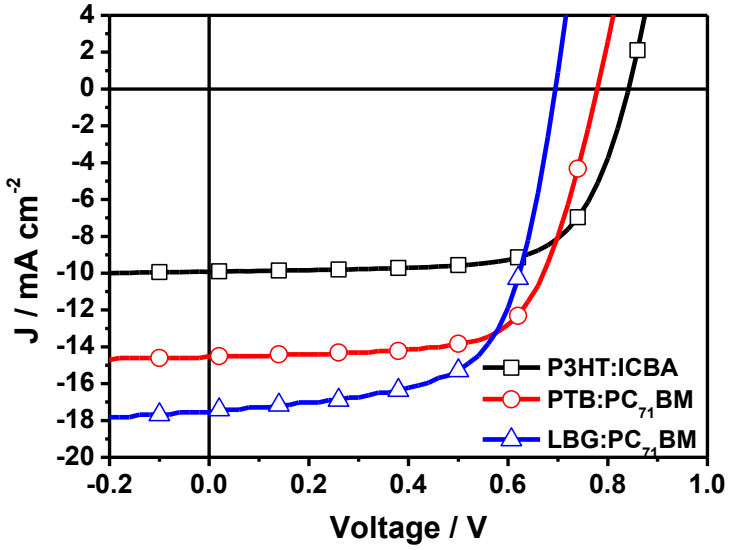

Figure 5.7 *J–V* characteristics of single-junction cells having P3HT:ICBA (200 nm), PTB:$PC_{71}BM$ (100 nm), and LBG:$PC_{71}BM$ (100 nm) as active layer materials.

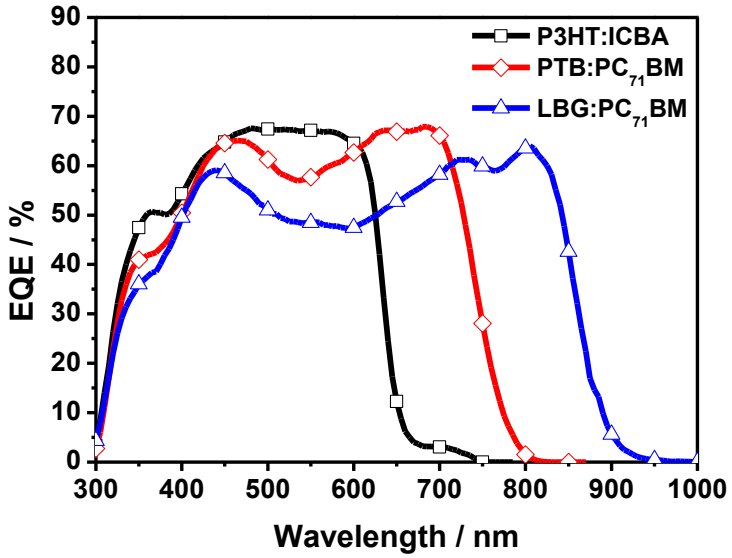

Figure 5.8 EQE spectra of single-junction cells having P3HT:ICBA (200 nm), PTB:$PC_{71}BM$ (100 nm), and LBG:$PC_{71}BM$ (100 nm) as active layer materials.

5.8 Design of interconnecting layers

In addition to optimizing the arrangement of the absorbers, we also wished to improve the compatibility of the interconnecting layers. Depending on the HOMO level of polymer donor materials, there are different corresponding ICL designs.

Figure 5.9 demonstrates the design of ICL consisted of PEDOT:PSS/ZnO. The HOMO level of P3HT is at -5.0 eV, which is same as the work function of PEDOT:PSS. Therefore, when P3HT is used as the subcell in the front, PEDOT:PSS can be applied directly on top of P3HT without much problems in hole transport. ZnO, on the other hand, is the electron transporting layer that extracts the electrons from the subcell in the back. Since ZnO has a strong electron affinity and blocks off hole transport efficiently, its compatibility with *n*-type materials, such as PC61BM and $PC_{71}BM$, is universal.

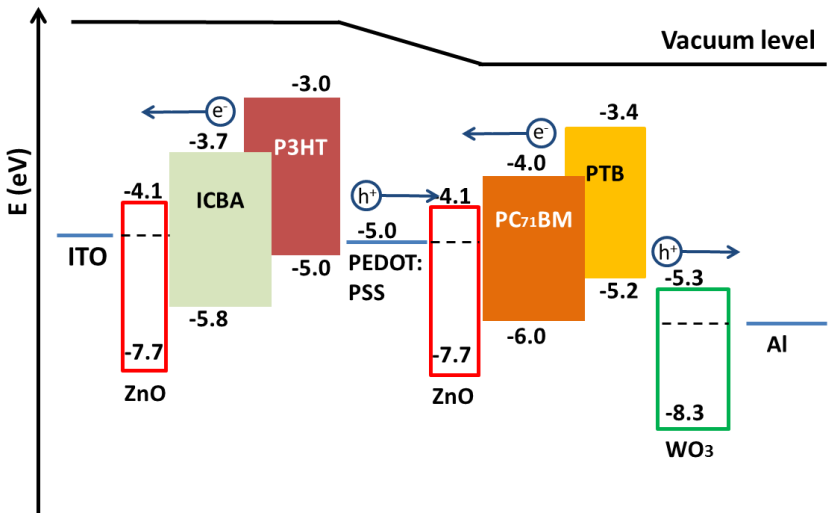

Figure 5.9 ICL design and energy level diagram for PEDOT:PSS/ZnO.

Figure 5.10 shows another ICL configuration, WO_3/PEDOT:PSS/ZnO, designed to overcome the mismatch in energy levels between the deep HOMO level of medium-bandgap and low-bandgap polymers (i.e., PTB and LBG) and the PEDOT:PSS interface; that is, by inserting a solution-based WO_3 thin layer from an alcohol-based nanoparticle dispersion. WO_3, with a conduction band of -5.3 eV close to the HOMO energy levels (~ -5.2 eV) of PTB and LBG, can form an ohmic-like contact that allows the transport of hole carriers to PEDOT:PSS or Al with negligible energy barriers. [140, 141] In particular, the deep-lying energy level of WO_3 should also improve the charge transport selectivity, which allows only hole carriers to be extracted from bulk heterojunction.[142] On the other hand, ZnO, with a conduction band of -4.1 eV, can be closed to the LUMO energy level of $PC_{71}BM$, functioning as the electron transporting layer. In between, a heavily doped interlayer, PEDOT:PSS (-5.0 eV), can function as a charge recombination junction for opposite charge carriers from adjacent subcells to recombine and to cancel out. Thus, the quasi-Fermi energy level of donor in one subcell can align with the quasi-Fermi energy level of acceptor in the other, resulting in a downward shift of the vacuum level, as displayed in the energy level diagram. Notably, this design for the ICL, using WO_3 as a hole transporting layer, allowed us to realize a fully solution processable multi-junction solar cell. More importantly, the universal compatibility of this ICL should allow additional donor materials to be incorporated into such a tandem design.

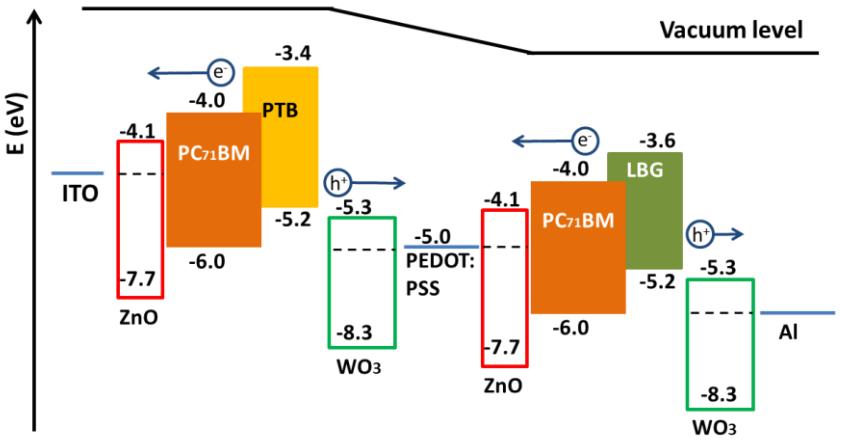

Figure 5.10 ICL design and energy level diagram for WO_3/PEDOT:PSS/ZnO.

5.9 Photovoltaic performance of double-junction cells

Figure 5.11 presents *J*–*V* characteristics of these three configurations of double-junction cells. Table 5.2 provides a summary of the photovoltaic performance.

In configuration 3, P3HT and LBG have large difference (0.5 eV) in their values of E_g. Thus, the maximum photocurrent provided by the front subcell of P3HT (ca. 10 mA·cm^{-2} in single-junction cells) can be fully matched by that of the back cell with LBG as the donor. When minimal spectral interference exists between two subcells, the ideal photocurrent of a tandem cell can equal the maximum current of the front cell in its single-junction setup.

In configuration 2, featuring PTB with its smaller bandgap (1.58 eV) and higher current density (ca. 14 mA·cm^{-2} in single-junction) in the front subcell position, the photocurrent in the tandem cell increased marginally, indicating the potential for LBG to provide a photocurrent greater than 10mA·cm^{-2} from the back subcell position. Nevertheless, because the absorption

windows of PTB and LBG overlap partially, the photocurrent obtained in their tandem cell reached only 75% of the maximum value of J_{SC} of the PTB-based single-junction cell.

In configuration 1 (P3HT and PTB-based subcells), which has slightly larger difference in the values of E_g (0.32 eV), the tandem provided a photocurrent density of 8.8 mA·cm^{-2}. In that case, the photocurrent of the tandem cell was 85% of the value of J_{SC} of the front subcell (P3HT) in a single-junction cell.

These results suggest that spectral interference of the subcells was the determining effect on the photocurrent output of the tandem cells. Between the two subcells, a difference in values of E_g of 0.5 eV (e.g., configuration 3) is desirable to ensure that the photocurrent of the tandem cell is close to that of its front subcell's maxima. Nevertheless, when the difference in values of E_g is only 0.2 or 0.3 eV, efficient tandem devices (e.g., configurations 1 and 2) can still be obtained by reducing the effect of optical interference through optical simulation and thickness fine-tuning, as we explain in the next section.

Table 5.2: Performance of double-junction (configurations 1–3) tandem cells.

Configuration	V_{OC} **(V)**	J_{SC} **(mA·cm^{-2})**	***FF***	**PCE (%)**
Double-junction 1	1.58	8.81	68.83	9.58
Double-junction 2	1.42	11.30	66.67	10.70
Double-junction 3	1.53	9.50	67.65	9.83

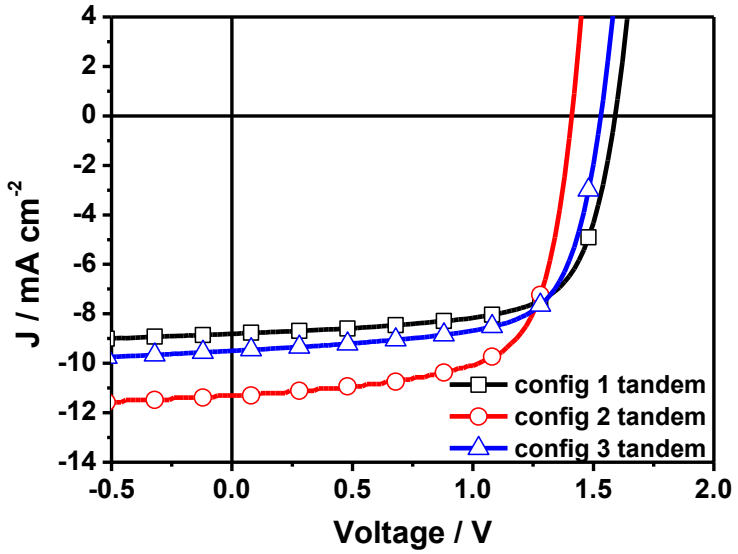

Figure 5.11 *J–V* curves of double-junction cells featuring different combinations of active layers.

5.10 Optical simulation

The optical modeling based on the transfer matrix formalism (TMF) was used to study the propagation of light within full stacks of layers in our study. The TMF method can be useful to calculate the amplitude of the electromagnetic field vector within a multilayer system (e.g., a tandem solar cell), including the effects of Fresnel reflections, transmissions, absorption, and phase shift.[143] To do so, we first need the refractive indices (*n*) and extinction coefficients (*k*) of the absorber materials tested in this study, which are shown in Figure 5.12.

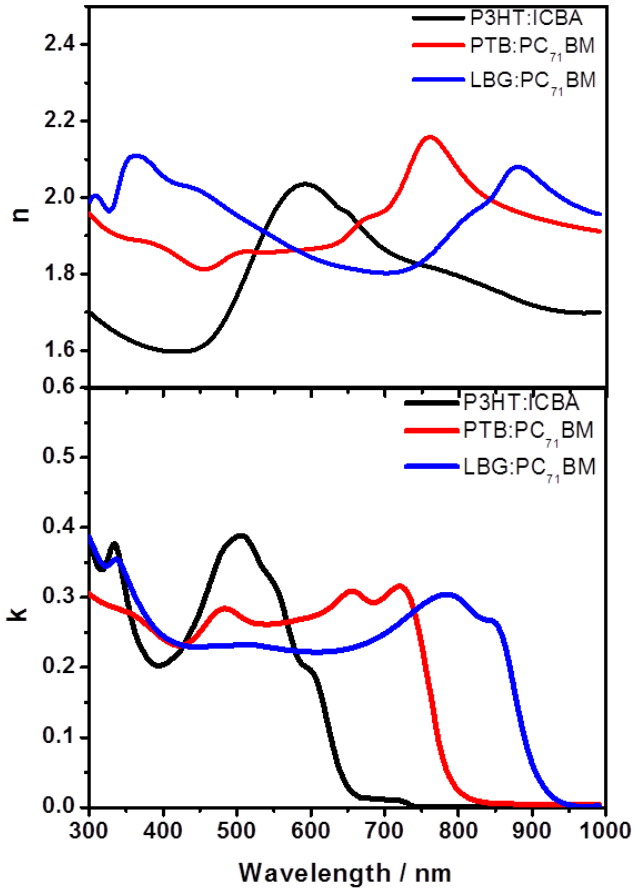

Figure 5.12 Optical parameters *n* and *k* for P3HT:ICBA, PTB:$PC_{71}BM$, and LBG:$PC_{71}BM$ absorbers used in tandem structure.

The relations between the complex refractive index and the dielectric function can be expressed by $\varepsilon'=n^2-k^2$ and $\varepsilon''=2nk$. All the optical simulations can thereby be carried out in terms of *n* and *k*. Assuming a wave traveling in one direction is E_{1R} and in opposite direction is E_{1L}, the change of phase and amplitude in wave vector when passing from layer 1 to layer 2 can then be expressed in a 2x2 matrix. More details on TMF can be found elsewhere.[144]

$$\begin{bmatrix} E_{1R} \\ E_{1L} \end{bmatrix} = \frac{1}{t_{12}} \begin{bmatrix} e^{-i\delta_2} & -r_{12}e^{i\delta_2} \\ -r_{12}e^{-i\delta_2} & e^{i\delta_2} \end{bmatrix} \begin{bmatrix} E_{2R} \\ E_{2L} \end{bmatrix} = \frac{1}{t_{12}} M_{12} \begin{bmatrix} E_{2R} \\ E_{2L} \end{bmatrix}$$

$$\delta_2 = \frac{2\pi}{\lambda} n_2 d_2 \tag{3.1}$$

The absorbed photon flux ($= \int \Phi G_j(x)\, dx$) for each subcell in multilayer tandem structure can be integrated from its optical absorption profile. Φ is the photon flux of the AM1.5G solar spectrum. $G_j(x)$ is the photon absorption rate based on the time-averaged energy density, $Q(x)$, dissipated per unit volume per second in layer j at position x.

$$G_j(x) = \frac{\lambda}{hc} \cdot \frac{Q_j(x)}{I_0} \tag{3.2}$$

I_0 is the energy density per unit area of the incident electric field. Commercially available software, such as FreeSnell and FLUXiM, can help calculate the absorbed photon flux profile.[145]

Figure 5.13 presents the simulated photon flux absorption rate profiles for our three double-junction tandem configurations. Here, the TMF allowed us to discover the distribution of photon flux of each subcell; in response, we could adjust the thickness parameter of each subcell accordingly to ensure similar amounts of photons being absorbed by the each subcell.[133] Here, we further calculate the maximum J_{SC} = (absorbed photon flux) * IQE * (1.6×10^{-19}) of the subcells in tandem, providing internal quantum efficiency for P3HT:ICBA,[146] PTB:$PC_{71}BM$,[147] and LBG:$PC_{71}BM$,[148] of approximately 75%, 80%, and 80%, respectively. Table 5.3 provides the details of these simulations and calculated J_{SC}.

Table 5.3: Results of TMF simulation details for double-junction devices based on the different configurations of active layer combinations. Simulated J_{SC} = (photon flux) * IQE * ($1.6x10^{-19}$).

Double Junc. (config 1)	**Thickness (nm)**	**Photon flux($x10^{16}$)**	**IQE(%)**	**Calculated J_{SC}(mA/cm^2)**
P3HT:ICBA	170	7.53	75	8.98
PTB:$PC_{71}BM$	100	7.36	80	9.36
Double Junc. (config 2)	**Thickness (nm)**	**Photon flux($x10^{16}$)**	**IQE(%)**	**Calculated J_{SC}(mA/cm^2)**
PTB:$PC_{71}BM$	80	8.89	80	11.31
LBG:$PC_{71}BM$	105	9.21	80	11.72
Double Junc. (config 3)	**Thickness (nm)**	**Photon flux($x10^{16}$)**	**IQE(%)**	**Calculated J_{SC}(mA/cm^2)**
P3HT:ICBA	200	8.26	75	9.85
LBG:$PC_{71}BM$	100	7.95	80	10.11

The predicted values of J_{SC} are labeled in the simulated graph for each subcell. Assuming that the lower value of J_{SC} in each tandem subcell configuration was equal to the photocurrent generated by that tandem cell, the results of the simulations were in good agreement with both the EQE and *J*–*V* measurements discussed above.

From Figures 5.13a and 5.13c, we can identify a relatively low photon absorption rate for the P3HT cell and confirm the requirement of a thick P3HT:ICBA film (150~200 nm) to ensure sufficient charge carrier generation. The PTB and LBG cells, on the other hand, have a broad range of photoresponses and much higher absorption rates; therefore, typical thicknesses for these two cells ranged from 80 to 100 nm.

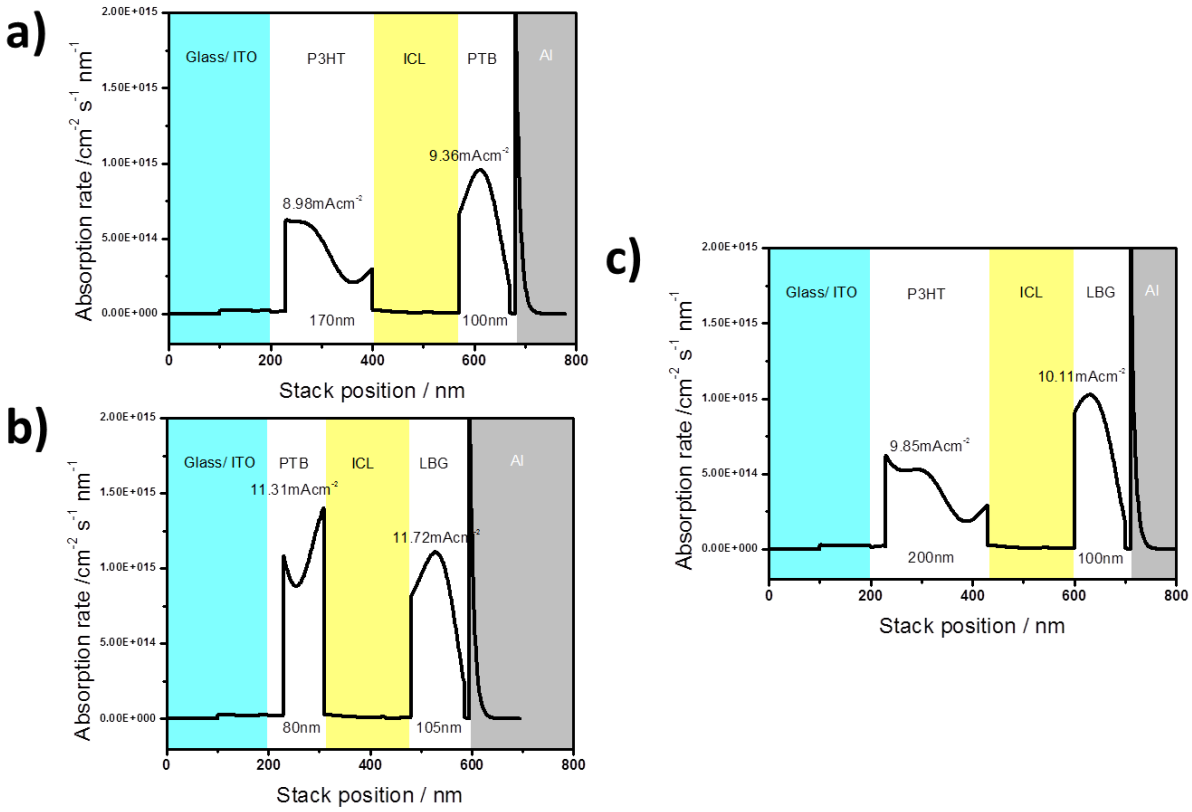

Figure 5.13 Photon absorption rates simulation for double-junction cells having the configurations P3HT:ICBA/PTB:$PC_{71}BM$, PTB:$PC_{71}BM$/LBG:$PC_{71}BM$, and P3HT:ICBA/LBG:$PC_{71}BM$.

5.11 External quantum efficiency measurement

To verify the accuracy of our optical simulations, we recorded EQE measurements under bias light (550, 650, and 800 nm wavelength) to provide each subcell's charge carrier generation profile vs. wavelength.

Figure 5.14a provides the EQE spectra of configuration 1. A region of spectral overlap between P3HT and PTB appears from 500 to 650 nm, resulting in a decrease in the overall EQE response. In particularly, the PTB cell could provide a J_{SC} of only 8.6 mA·cm^{-2} (integrated from the EQE spectrum), which is a huge loss compared with its capability in a single junction (14.5 mA·cm^{-2}).

Figure 5.14b reveals that both PTB and LBG depend on the spectral region from 550 nm to 750 nm for light harvesting. Similarly, when a broad region of optical interference exists in an EQE spectrum, the back subcell (LBG) would suffer a greater loss than the front subcell (PTB) in its capability to generate charge carriers.

Figure 5.14c reveals complementary spectral responses from both P3HT and LBG. One noticeable difference is that the peak maximum of the P3HT-based subcell (64%) is close to that of its single-junction cell (65%), suggesting negligible absorption interference from LBG in the back subcell. All the measured J_{SC} above from EQE are in a good agreement with our simulated J_{SC} from optical modeling.

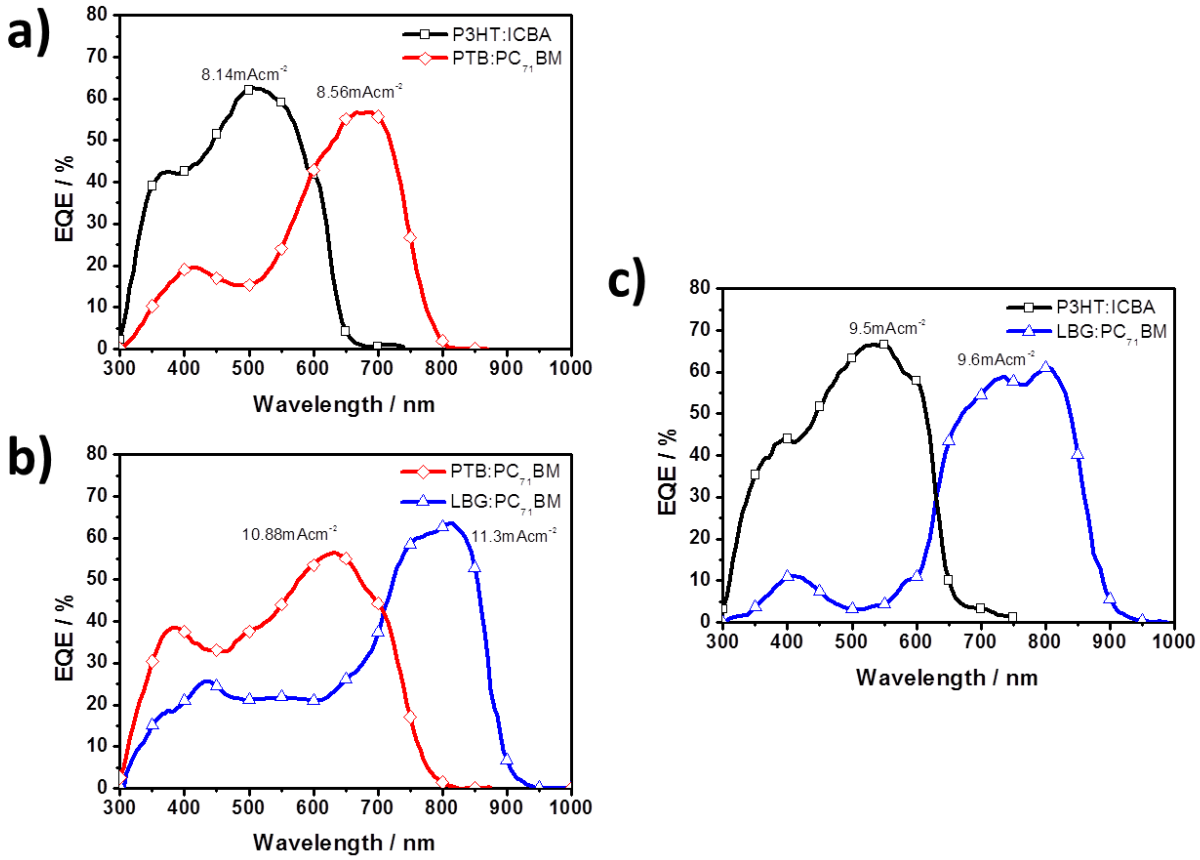

Figure 5.14 The EQE spectra for double-junction cells having the configurations P3HT:ICBA/PTB:$PC_{71}BM$, PTB:$PC_{71}BM$/LBG:$PC_{71}BM$, and P3HT:ICBA/LBG:$PC_{71}BM$.

5.12 Summary

In summary, we have explored different designs for double-junction solar cells. To study the optical interference effect, we arranged polymeric materials having bandgaps of 1.9, 1.58, and 1.4 eV as either the front or back subcell in double-junction tandem structures. We found that the difference in E_g should be at least 0.2 eV between front and back subcells to avoid spectra overlap. When the difference in E_g reached 0.5 eV, the spectra is mismatched and favorable in generating high photocurrent output.

Chapter 6 Triple-Junction Organic Tandem Solar Cells

6.1 Introduction

In the last section, we demonstrated that organic tandem solar cells based on double-junction and complementary absorbers can exhibit power conversion efficiencies (PCEs) exceeding 10%. The maximum efficiency is, however, only slightly higher than the record efficiency of a single-junction organic cell,[14, 147] suggesting that there is great room for improvement in the design of multi-junction organic solar cells. To advance the performance of their PCEs, multi-junction tandem solar cells should feature an optimal combination of bandgap energies (E_g) and complete coverage of the solar spectrum. From a theoretical point of view, triple-junction tandem solar cells have the tendency to outperform their double-junction analogues in terms of enhanced open circuit voltages (V_{OC}).

In the ideal configuration of a triple-junction tandem solar cell, broad differences in the values of E_g of the individual absorbers would guarantee each subcell generated a sufficient number of charge carriers without optical interference between the subcells. For example, in III–V multi-junction solar cells, the optimal arrangement for a high-current-output triple-junction tandem cell features one wide-bandgap absorber (2.0–1.85 eV), one medium-bandgap absorber (1.4–1.2 eV), and one low-bandgap absorber (1.0–0.7 eV).[149, 150]

This optimal design rule cannot be applied directly to organic solar cells, however, because of the lack of efficient donor materials having bandgaps as low as 1 eV.[151] In fact, when the bandgap of a polymeric material is 1 eV, one encounters several critical issues, including an extremely low value of V_{OC} and a small lowest unoccupied molecular orbital (LUMO) offset with PCBM, resulting in compromised charge separation efficiency and inferior

PCE.[152] Therefore, we wished to determine a practical combination of bandgap energies for triple-junction cells to develop an efficient organic tandem solar cell structure.

In the previous chapter, we already discussed wide-bandgap (e.g., P3HT) and low-bandgap (e.g., PDTP-DFBT) candidate materials. Here, we propose to use a novel medium-bandgap material that has the E_g in between low-bandgap and wide-bandgap materials. The requirement and available candidates for medium-bandgap absorbers are provided as follows:

a) Medium-bandgap materials ($1.5 < E_g < 1.7$ eV): **PBDTTT-C (**E_g ~ 1.61 eV)[153] are the first medium-bandgap absorber exceeding 6% PCE, followed by **PTB7 (**E_g ~ 1.60 eV)[11] with 7~8% PCE. Last year, the most recently developed medium-bandgap absorber was **PTB7-Th (**E_g ~ 1.58 eV)[14] with 9% PCE. The corresponding chemical structures are shown in Figure 6.1.

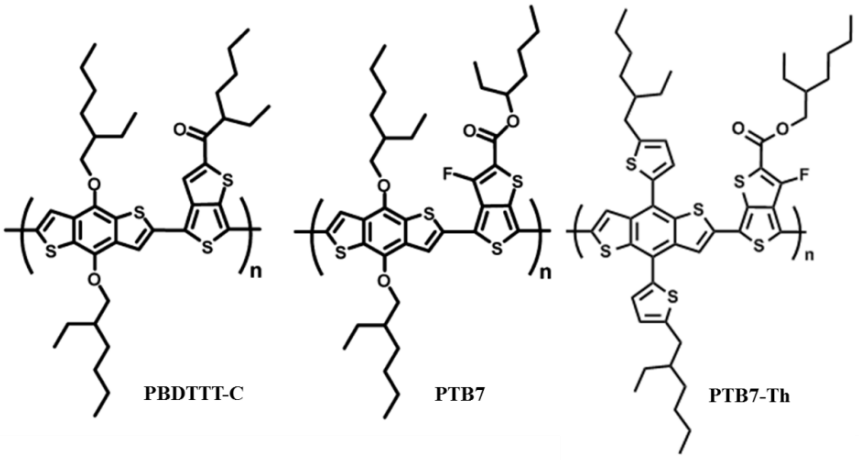

Figure 6.1 The chemical structure of commonly used medium-bandgap polymers.

Here, we present a triple-junction organic tandem solar cell featuring a configuration of bandgap energies designed to maximize the tandem photocurrent output. For the practical design of a triple-junction tandem cell containing organic absorbers, the arrangement of bandgap energies for subcells should be set as following:

a) one wide-bandgap donor (E_{g1}, 1.85–2.0 eV),

b) one medium-bandgap donor (E_{g2}, 1.5–1.7 eV), and

c) one low-bandgap donor (E_{g3}, 1.3–1.4 eV).

Furthermore, given that the absorption spectra of these three materials will inevitably overlap, due to the narrow variations in their values of E_g, we used optical simulation to balance the rates of photon absorption among the subcells and, thereby, minimize current-mismatch losses.

6.2 Device structure

Figure 6.2 displays a schematic representation of the complete device structure. We placed P3HT:ICBA, which has the widest-bandgap donor (E_{g1} = 1.9 eV), in the front subcell position, followed by PTB:$PC_{71}BM$ (E_{g2} = 1.58 eV) as the middle subcell (i.e., $E_{g1} > E_{g2}$); we employed LBG:$PC_{71}BM$, which has the lowest-bandgap donor (E_{g3} = 1.4 eV), as the back subcell (i.e., $E_{g1} > E_{g2} > E_{g3}$). In this design, a photon energy $h\nu$ greater than E_{g1} would be absorbed first by the front subcell, leaving lower energy photons to be harvested selectively by the middle and back subcells. Excess thermalization energy of charge carriers would, therefore, be utilized more efficiently in this triple-junction cell resulting in a higher theoretical efficiency limit relative to those of single- and double-junction cells.[154]

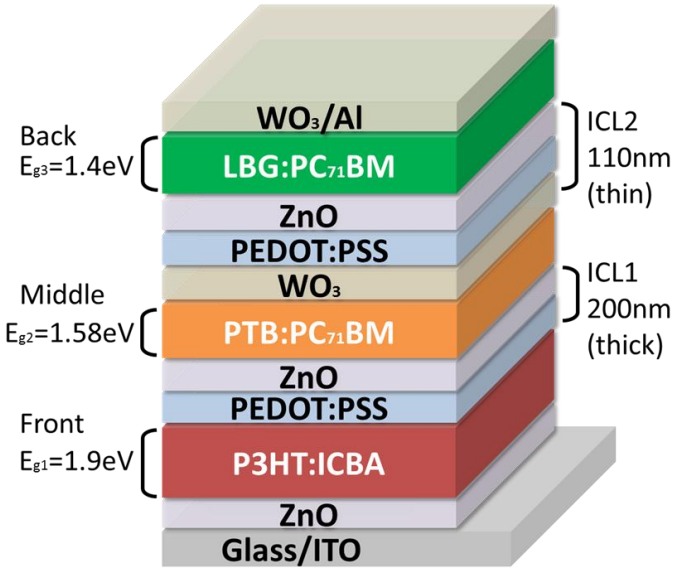

Figure 6.2 Layer stacks of the triple-junction tandem solar cell in the inverted architecture.

6.3 Material and device fabrication

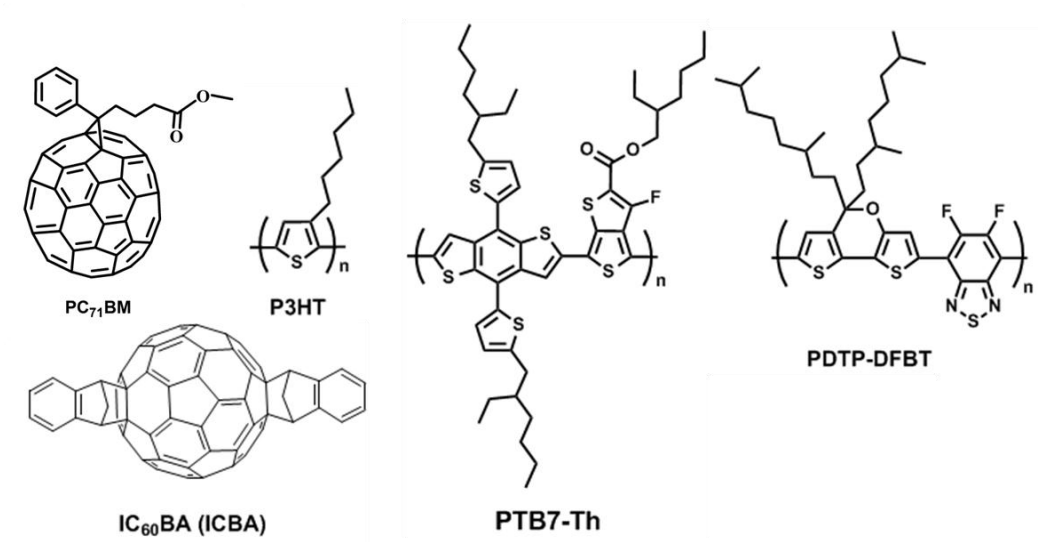

Figure 6.3 Chemical structures of the polymers and fullerene derivatives.

Triple-junction tandem fabrication: First, the same procedure as that for fabrication of P3HT:ICBA (160 nm) as the front subcell was followed. After depositing the 170-nm PEDOT:PSS and 30-nm ZnO layers, a chlorobenzene solution of PTB:$PC_{71}BM$ was spin-coated and then the sample was left in a glove box for 1 h to remove residual DIO. Next, a 10-nm-thick WO_3 layer was spin-coated from an EtOH dispersion, followed by deposition of 80-nm-thick PEDOT:PSS and annealing at 100 °C for 10 s. A 20-nm-thick ZnO layer was deposited using the previous solution and then the sample was annealed at 100 °C for 20 s. The active layer of the back subcell (LBG:$PC_{71}BM$) was spin-coated on the ZnO surface. Finally, a 20-nm WO_3 layer was deposited on the back subcell using the same solution and then 100-nm Al was deposited through thermal evaporation. All steps were carried out inside N_2-filled glovebox.

Device characterization: The *J–V* characteristics of the photovoltaic cells were recorded using a Keithley 2400 source measure unit under a simulated AM1.5G spectrum with an Oriel 9600 solar simulator, adjusted using a monocrystalline silicon solar cell equipped with a KG5 filter and calibrated by the National Renewable Energy Laboratory (NREL). During measurements, to avoid parasitic current, each device (fingers) was absolutely isolated by scratching the films surrounding the devices and measured with a 0.1 cm^2 mask. EQEs were measured using an integrated system (Enlitech, Taiwan) and a lock-in amplifier with a current preamplifier under short-circuit conditions. The light spectrum was calibrated using a monocrystalline photodetector of known spectral response. Light bias of 550, 650, and 800 nm was selected to excite the front, middle, and back subcells, respectively, in the tandem devices.[137] The unexcited subcell was then measured using a Xe lamp passing through a monochromator with a typical intensity of 10 μW. The optical parameters *n* and *k* were obtained

through spectroscopic ellipsometry. Energy levels were obtained through UPS measurements performed within an Omicron XPS/UPS system.

6.4 Optical absorption

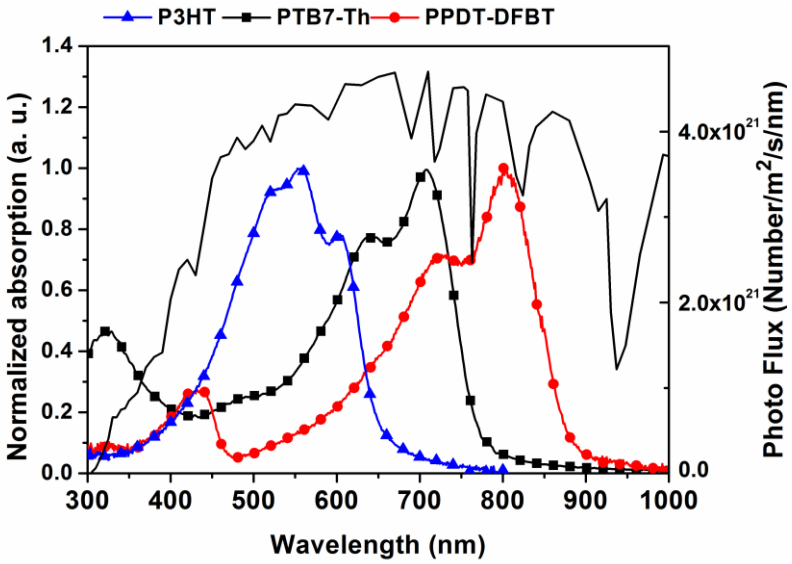

Figure 6.4 Normalized absorption spectra of the polymers used in the study.

Figure 6.4 presents the normalized absorption spectra of the absorber materials tested in this study. Starting with the wide-bandgap (E_{g1}) and low-bandgap (E_{g3}) donors, we selected polymers having the largest possible difference in their values of E_g. Accordingly, we chose the polymers P3HT and PDTP-DFBT (hereafter designated as LBG) for their complementary absorption spectra. P3HT (E_{g1} = 1.9 eV) has an absorption window for visible light that extends to 650 nm; LBG (E_{g3} = 1.4 eV) can sense near-IR photons up to 950 nm. In between, there is a 300-nm gap in absorption wavelengths, allowing the application of a third absorber material. The ideal candidate should possess a medium-level bandgap to harvest most of the light in the window between 600 and 750 nm and, at the same time, exhibit minimal optical interference with the other two donor materials outside that absorption window.

We selected PTB7-Th (hereafter designated as PTB), a medium-bandgap absorber having a value of E_{g2} of 1.58 eV for this study. From the *k* spectrum, the absorption edge of PTB lies approximately 120 nm to the right of that of P3HT and approximately 150 nm to the left of that of LBG. More importantly, a predominant absorption peak of PTB is centered at 650 nm, coinciding with the minimal absorptions of both P3HT and LBG, suggesting that this combination of donors has an excellent chance of providing a high photocurrent output when used in tandem.

6.5 Design of interconnecting layers

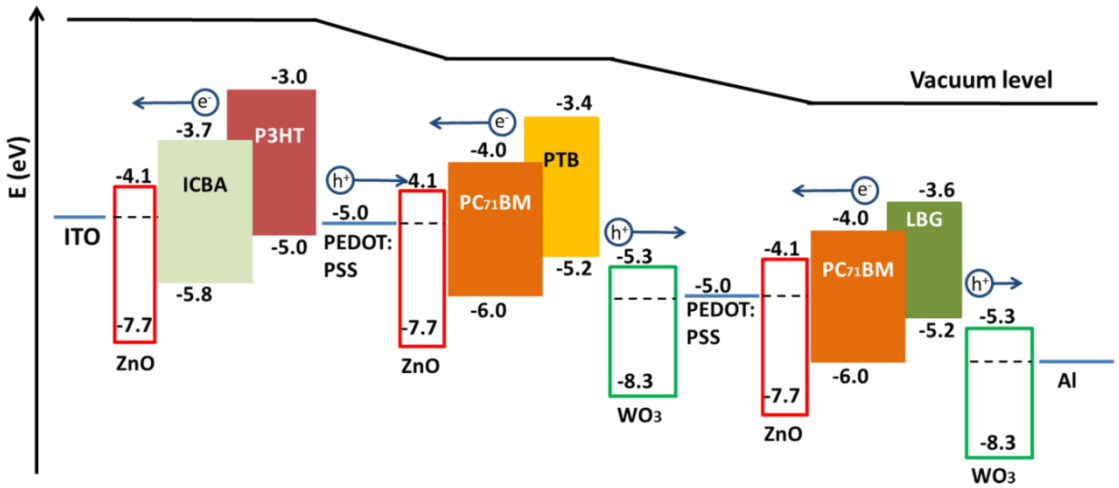

Figure 6.5 Device structure and energy level diagram of ICL.

The triple-junction tandem structure is simply the stacking of two double-junction tandem structure monolithically. Therefore, the ICL design in triple-junction follows the designs (PEDOT:PSS/ZnO, WO_3/PEDOT:PSS/ZnO) previously demonstrated by the double-junction tandem devices in Chapter 5.

6.6 Optical simulation: $|E|^2$

Optical simulation of the triple-junction tandem cell was performed in order to find out the optimized thickness for each layer. As more layers are incorporated, the stacking thickness of the complete tandem device can easily reach 500 nm, making the relative position of each subcell an influential parameter that might affect the rates of absorption of the polymers.

Figure 6.6 presents the normalized optical electrical fields $|E|^2$ for the peak absorptive wavelengths (λ = 500, 600, 700, 800 nm) of the donor materials. All the waves propagating inside the triple-junction cell were standing waves with a fixed node starting at the reflective electrode, Al.[144] Since the propagating wave can have several antinodes within the tandem device, only the subcells with the position matching the peaks of antinodes in $|E|^2$ amplitude of the waves will feature the highest number of utilizable photons.

At first look, the LBG-based subcell with close proximity to the Al electrode will come across the first antinode's peak of all wavelengths making its photon collection efficient. A thick layer of P3HT can cover up to two antinodes' peaks of 500- and 600-nm light, regardless of its position. The most inefficient subcell—the one that is most often far from the position of the maximum $|E|^2$ amplitude—should become the middle subcell.

Here, we found that the thicknesses of the ICLs between the front and middle subcell (ICL1) and between the middle and back subcell (ICL2) could be varied to tune the relative position of the middle subcell. Starting with thick layers (PEDOT:PSS, 160 nm; ZnO, 20 nm) for both ICL1 and ICL2, we found that the unoptimized position of the middle subcell coincided with the minimal optical fields of the 600- and 700-nm light.

By adjusting the thickness of ICL1 to 200 nm (PEDOT:PSS, 160 nm; ZnO, 40 nm) and ICL2 to 110 nm (WO_3, 10 nm; PEDOT:PSS, 80 nm; ZnO, 20 nm), we shifted the position of the middle subcell toward the back subcell, where the third antinode's peaks of all wavelengths coincided with the middle subcell. Thus, having identified the optimized position for all subcells, we believed that the achievable photocurrent would increase accordingly.

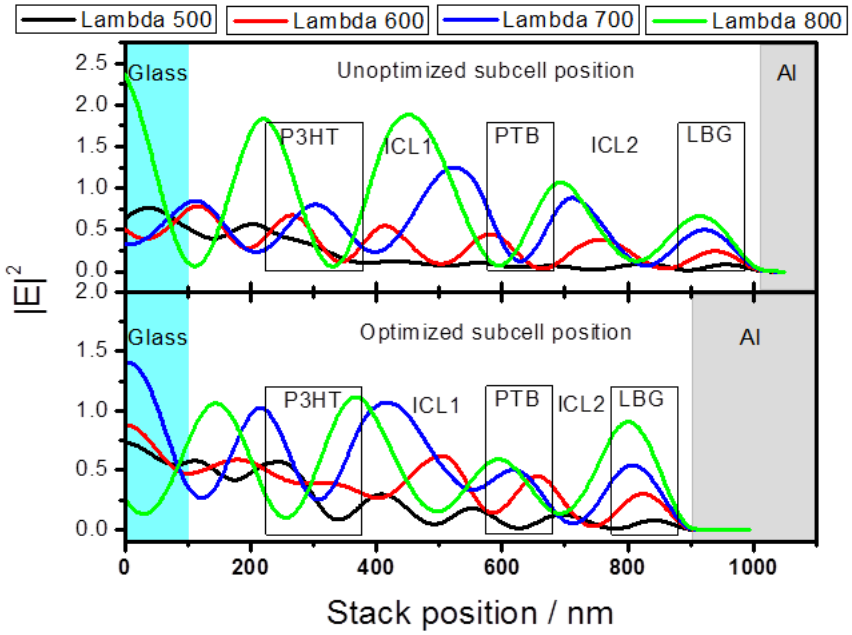

Figure 6.6 Values of $|E|^2$ in triple-junction tandem cells at wavelengths (λ) of 500 nm (black), 600 nm (red), 700 nm (blue), and 800 nm (green) for the optimized (ICL1: 200 nm; ICL2: 110 nm) and unoptimized (ICL1, ICL2: 180 nm); subcell positions are shown by rectangles.

6.7 Optical simulation: photon flux

In a triple-junction cell, optical interference is inevitable between donor materials having small differences in their values of E_g; therefore, adjusting the thicknesses of the subcells can redistribute the uneven photon absorptions among the subcells to provide matched photocurrents.[133] Here, we used TMF simulations to make these adjustments.

In the initial setup, we applied the unoptimized thicknesses of the three subcells according to the values in which their single-junction cells absorbed the most photons in their spectral responses—namely 200, 100, and 100 nm for the P3HT-, PTB-, and LBG-based cells, respectively. These values can be considered as upper limits for their adjustment before the charge collection efficiency begins to drop, resulting in a low fill factor (*FF*).

From the corresponding photon absorption profiles in Figure 6.7, a 100-nm-thick PTB cell produced the lowest photon flux (5.8×10^{16} s^{-1} cm^{-2}) among the three subcells. From Table 6.1, the predicted value of J_{SC} indicates an unmatched charge carrier generation of approximately 1 mA cm^{-2} in between PTB and the other two subcells. Increasing the thickness of the PTB cell could enhance its absorbed photon flux, but at the cost of decreasing the FF. More importantly, from the optical electrical field, we found that light having wavelengths of 600 and 700 nm already have their maximum intensity field at the center of the PTB cell. Therefore, increasing the PTB cell thickness alone would not improve the degree of photon absorption significantly.

Instead, we had to decrease the thickness of the P3HT and LBG cells in response to the excess generated carriers that would flow to adjacent subcells as unwanted leakage current. Figure 6.7 reveals that the most balanced photon absorption was achieved when the P3HT, PTB, and LBG cells had thicknesses of 160, 110, and 85 nm, respectively. Because the peaks of first antinodes for all wavelengths of light coincided perfectly with the position of the back subcell inside the tandem cell, the LBG cell could provide the same amount of charge carriers as the other two cells while being the thinnest of them all. The calculated values of J_{SC} for the P3HT, PTB, and LBG cells at their optimized thicknesses were 7.9, 7.9, and 7.8 mA cm^{-2}, respectively from Table 6.1.

Table 6.1 Results of TMF simulation details for triple-junction devices based on the different subcell thickness. Simulated J_{SC} = (photon flux) * IQE * ($1.6x10^{-19}$).

Triple Junc. (unoptimized)	**Thickness (nm)**	**Photon flux($x10^{16}$)**	**IQE(%)**	**Calculated J_{SC}(mA/cm^2)**
P3HT:ICBA	200	7.21	75	8.6
PTB:$PC_{71}BM$	100	5.81	80	7.4
LBG:$PC_{71}BM$	100	6.76	80	8.6
Triple Junc. (optimized)	**Thickness (nm)**	**Photon flux($x10^{16}$)**	**IQE(%)**	**Calculated J_{SC}(mA/cm^2)**
P3HT:ICBA	160	6.62	75	7.9
PTB:$PC_{71}BM$	110	6.21	80	7.9
LBG:$PC_{71}BM$	85	6.13	80	7.8

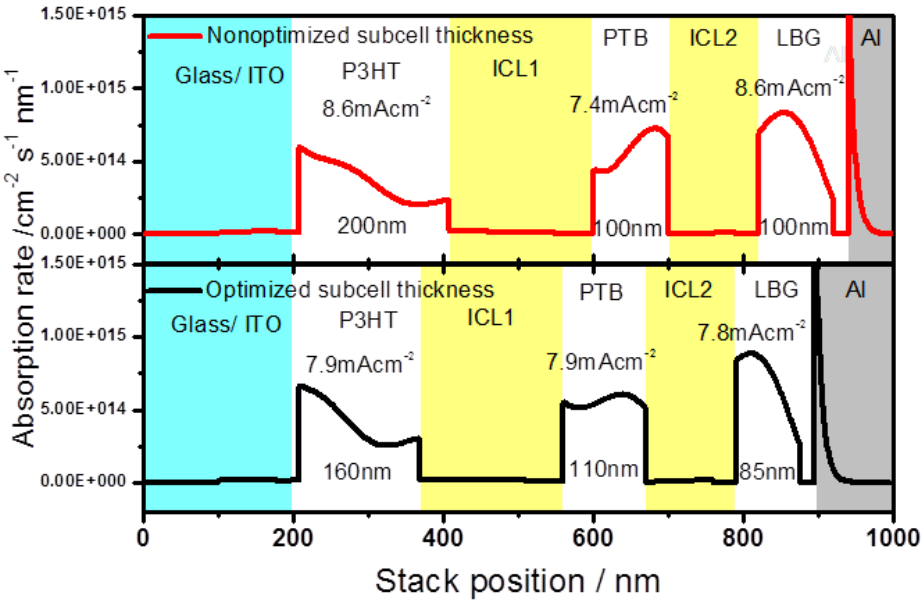

Figure 6.7 Photon absorption rates simulated for triple-junction tandem cells having optimized (160, 110, and 85 nm) and unoptimized (200, 100, and 100 nm) subcell thicknesses (P3HT:ICBA, PTB:$PC_{71}BM$, LBG:$PC_{71}BM$).

6.8 Photovoltaic performance of triple-junction cells

Finally, we fabricated the triple-junction tandem solar cells; Figure 6.8 presents their photovoltaic performance. The combination of subcells of unoptimized thickness (200, 100, 100 nm) produced a PCE of only 8.64%, with a value of J_{SC} of 6.95 mA·cm^{-2}, a value of V_{OC} of 2.22 V, and an *FF* of 0.56. Clearly, even if the number of charge carriers generated by each subcell was unbalanced by only a small fraction (1 mA·cm^{-2}, as suggested by simulation), a tandem solar cell can experience a great loss in performance.

Using the combination of calculated optimized thicknesses (160, 110, 85 nm), the PCE improved to 11.55%, along with a value of J_{SC} of 7.63 mA·cm^{-2}, a value of V_{OC} of 2.28 V, and an *FF* of 0.66; Table 6.2 summarizes the details. One noticeable difference here is the recovery of the value of V_{OC} when using the optimized thickness combination—it is close to the theoretical sum of the values of V_{OC} from the individual subcells. This finding indicates that approximately equal numbers of charge carriers were generated from the subcells and efficiently recombined at the two ICL interfaces, resulting in minimal energy loss for quasi-Fermi level alignment between subcells in the tandem solar cell.

Table 6.2 Performance of triple-junction (unoptimized/optimized subcell thicknesses) tandem cells.

Configuration	V_{OC} **(V)**	J_{SC} **(mA·cm^{-2})**	***FF***	**PCE (%)**
Triple-junction[1]	2.22	6.95	56.64	8.64
Triple-junction[2]	2.28	7.63	66.39	11.55
	(2.26 ± 0.02)*	(7.3 ± 0.3)*	(64 ± 3)*	(11.0 ± 0.5)*

[1]Unoptimized thicknesses (200, 100, 100 nm),
[2]Optimized thicknesses (160, 110, 85 nm),
*Average performance taken from 20 devices.

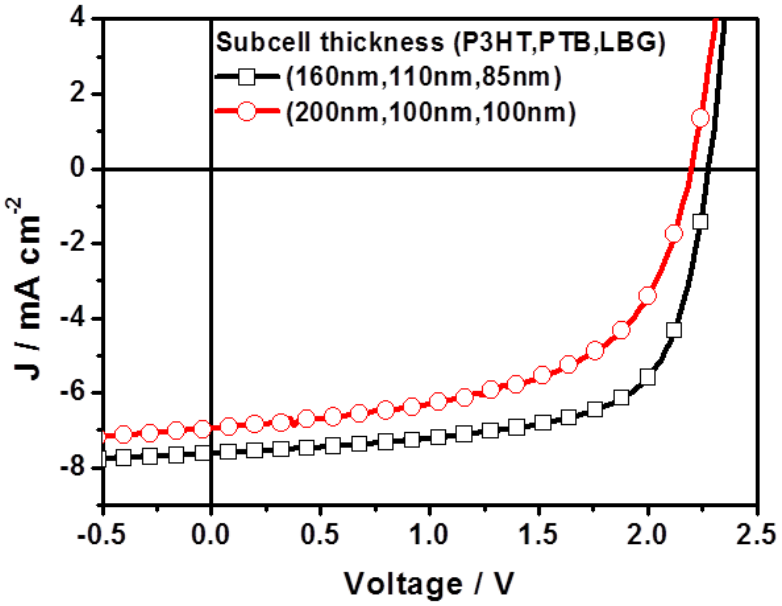

Figure 6.8 *J-V* for triple-junction tandem cells having optimized (160, 110, and 85 nm) and unoptimized (200, 100, and 100 nm) subcell thicknesses (P3HT:ICBA, PTB:$PC_{71}BM$, LBG:$PC_{71}BM$).

6.9 External quantum efficiency measurement

We also investigated the improvement in photocurrent through EQE measurements, with the integrated values of J_{SC} labeled for each subcell (Figure 6.9). These results are in good agreement with the values of J_{SC} calculated through optical modeling and measured from *J-V* curve. The EQE spectra of the front and middle subcells closely resemble those of the double-junction cell in configuration 1. This observation might imply a possible limitation, due to similar optical interference issues; further improvements in performance might be possible by raising the EQEs of these two subcells.

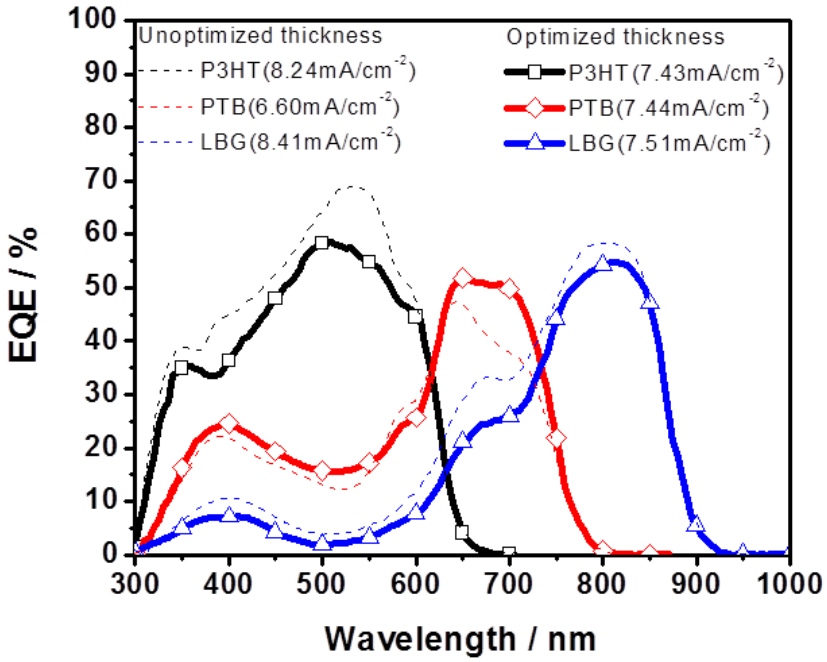

Figure 6.9 EQE spectra for triple-junction tandem cells having optimized (160, 110, and 85 nm) and unoptimized (200, 100, and 100 nm) subcell thicknesses (P3HT:ICBA, PTB:$PC_{71}BM$, LBG:$PC_{71}BM$).

6.10 Summary

In conclusion, we have demonstrated an efficient design for a triple-junction tandem solar cell: using three materials with different energy bandgaps as electron donors, blended with fullerene derivatives. To improve current matching, we selected materials having bandgaps in the order 1.9, 1.58, and 1.4 eV. With such an arrangement of bandgap energies, we fabricated a highly efficient triple-junction tandem solar cell having a PCE of 11%—exceeding the record efficiency of a double-junction tandem solar cell previously demonstrated by our group.

Through optical simulation and the TMF modeling method, we could overcome the difficulty of current matching the subcells and simplify the process of fine-tuning the thickness of each subcell and ICL. The agreement between our experimental results and the simulated data reveals the feasibility and accuracy of using optical modeling in the design of organic multi-junction solar cells—especially in optimizing the thicknesses of the subcell absorbers. Our results also suggest that triple-junction tandem solar cells have great potential for use in high-performance applications.

Chapter 7 Conclusions and Future Outlook

In this dissertation, we studied the design and formation of organic tandem solar cells. Design improvements to tandem structure are implemented via the interconnecting layers, top electrode, and absorber arrangement to improve the photovoltaic performance. Formations of organic tandem solar cells are demonstrated in both double- and triple-junction cells, and also in both regular and inverted device architectures.

In Chapter 3 and 4, the designs of semi-transparent organic tandem solar cells based on regular device architecture are revealed. The motivation is to demonstrate organic solar cells with controllable visible transmission. First, the design of single-junction cells with exceptional visibly transparency is disclosed. The polymer absorbers selected for this task are low-bandgap polymers (with E_g ~ 1.4 eV), which mainly harvest the near-IR photons and are transparent to visible wavelength. The top electrode is spray-coated silver nanowire electrode. The resulting efficiency and transparency for single-junction cells are 4% PCE and 60% visible transmission, respectively. Furthermore, a design of tandem structure is also implemented to create high-performance, semi-transparent solar cell devices. By stacking two IR-absorbers in tandem structures, the performance of semi-transparent solar cells can be improved to 7% PCE with 30% visible transmission.

In Chapter 5 and 6, the designs of organic tandem solar cells are introduced in inverted device architecture, in order to create double- and triple-junction cells. The motivation is driven by the potential to break the efficiency limits above 10% PCE. The efforts of Chapter 5 and 6 are devoted to the interfacial layer designs, new polymeric materials developments, and optical simulations. As result, the double-junction tandem cells are able to reach 10% PCE while the

triple-junction tandem cells can achieve 11% PCE. Based on these achievements, we are optimistic that PCE will continue to improve for tandem-structure PSCs in the near future. Even at the current stage, the excellent performance of tandem PSCs over 10% PCE is already cost-effective and ready for commercialization.

Furthermore, when it comes to up-scaling and mass production of organic solar cells, the tandem structure may become a major concern regarding its complicated processing steps that may take up to 10 sequential layer-by-layer depositions. Here, we expect the future research development of organic tandem solar cells will address the manufacturing complexity by the simplification of device structures as well as reducing processing steps.

One way to simplify the tandem structure for PSC, is through reducing the interfacial layers in ICL. One approach may be integrating ETL materials (e.g., polyethylenimine) or HTL materials (e.g., fluoropolymers) into the coating step of the bulk heterojunction layer. Due to lateral phase separation driven by the difference in the surface energy, the interfacial layers will "float" to the right position in the tandem structure. Another alternative approach in simplifying tandem structure is designing an interfacial layer that can act as the HTL when contacting donor materials and as the ETL when contacting acceptor materials. Thus, we only need one single layer in ICL design.

Another approach to reduce processing steps may be realized through slot-die coating. A special design of slot-die coater may allow multiple layers to be coated at once, thereby reducing the manufacturing complexity caused by the tandem structures.

References

[1] A. Campoccia, L. Dusonchet, E. Telaretti, and G. Zizzo, “An analysis of feed’in tariffs for solar PV in six representative countries of the European Union,” *Solar Energy,* **2014**, 107, 530-542.

[2] M. A. Green, “Photovoltaic physics and devices,” *Solar Energy: The State of the Art*, **2013**, 291.

[3] L. M. Fraas, "History of solar cell development," *Low-Cost Solar Electric Power*, pp. 1-12: Springer, 2014.

[4] A. K. Ghosh, and T. Feng, “Merocyanine organic solar cells,” *Journal of Applied Physics*, **1978**, 49(12), 5982-5989.

[5] C. W. Tang, “Two-layer organic photovoltaic cell,” *Applied Physics Letters*, **1986**, 48(2), 183-185.

[6] N. Sariciftci, D. Braun, C. Zhang, V. Srdanov, A. Heeger, G. Stucky, and F. Wudl, “Semiconducting polymer-buckminsterfullerene heterojunctions: Diodes, photodiodes, and photovoltaic cells,” *Applied Physics Letters,* **1993**, 62(6), 585-587.

[7] M. D. McGehee, and M. A. Topinka, “Solar cells: pictures from the blended zone,” *Nature materials,* **2006**, 5(9), 675-676.

[8] S. E. Shaheen, C. J. Brabec, N. S. Sariciftci, F. Padinger, T. Fromherz, and J. C. Hummelen, “2.5% efficient organic plastic solar cells,” *Applied Physics Letters,* **2001**, 78(6), 841-843.

[9] F. Padinger, R. S. Rittberger, and N. S. Sariciftci, “Effects of postproduction treatment on plastic solar cells,” *Advanced Functional Materials,* **2003**, 13(1), 85-88.

[10] G. Li, V. Shrotriya, J. Huang, Y. Yao, T. Moriarty, K. Emery, and Y. Yang, “High-efficiency solution processable polymer photovoltaic cells by self-organization of polymer blends,” *Nature Materials,* **2005**, 4(11), 864-868.

[11] Y. Liang, Z. Xu, J. Xia, S. T. Tsai, Y. Wu, G. Li, C. Ray, and L. Yu, “For the bright future—bulk heterojunction polymer solar cells with power conversion efficiency of 7.4%,” *Advanced Materials,* **2010**, 22(20), E135-E138.

[12] M. G. Turbiez, R. A. J. Janssen, M. M. Wienk, H. J. Kirner, M. Düggeli, B. Tieke, and Y. Zhu, "Diketopyrrolopyrrole polymers as organic semiconductors," Google Patents, 2007.

[13] J. C. Bijleveld, A. P. Zoombelt, S. G. Mathijssen, M. M. Wienk, M. Turbiez, D. M. de Leeuw, and R. A. Janssen, “Poly (diketopyrrolopyrrole-terthiophene) for ambipolar logic and photovoltaics,” *Journal of the American Chemical Society,* **2009**, 131(46), 16616-16617.

[14] S.-H. Liao, H.-J. Jhuo, P.-N. Yeh, Y.-S. Cheng, Y.-L. Li, Y.-H. Lee, S. Sharma, and S.-A. Chen, "Single junction inverted polymer solar cell reaching power conversion efficiency 10.31% by employing dual-doped zinc oxide nano-film as cathode interlayer," *Scientific Reports,* **2014**, 4.

[15] L. Dou, J. You, Z. Hong, Z. Xu, G. Li, R. A. Street, and Y. Yang, "25th anniversary article: A decade of organic/polymeric photovoltaic research," *Advanced Materials,* **2013**, 25(46), 6642-6671.

[16] Y. Liu, X. Wan, F. Wang, J. Zhou, G. Long, J. Tian, J. You, Y. Yang, and Y. Chen, "Spin-coated small molecules for high performance solar cells," *Advanced Energy Materials,* **2011**, 1(5), 771-775.

[17] A. K. K. Kyaw, D. H. Wang, V. Gupta, J. Zhang, S. Chand, G. C. Bazan, and A. J. Heeger, "Efficient Solution-processed small-molecule solar cells with inverted structure," *Advanced Materials,* **2013**, 25(17), 2397-2402.

[18] A. K. K. Kyaw, D. H. Wang, D. Wynands, J. Zhang, T.-Q. Nguyen, G. C. Bazan, and A. J. Heeger, "Improved light harvesting and improved efficiency by insertion of an optical spacer (ZnO) in solution-processed small-molecule solar cells," *Nano letters,* **2013**, 13(8), 3796-3801.

[19] V. Gupta, A. K. K. Kyaw, D. H. Wang, S. Chand, G. C. Bazan, and A. J. Heeger, "Barium: an efficient cathode layer for bulk-heterojunction solar cells," *Scientific Reports*, **2013**, 3.

[20] B. Kan, Q. Zhang, M. Li, X. Wan, W. Ni, G. Long, Y. Wang, X. Yang, H. Feng, and Y. Chen, "Solution-processed organic solar cells based on dialkylthiol-substituted benzodithiophene unit with efficiency near 10%," *Journal of the American Chemical Society,* **2014**, 136(44), 15529-15532.

[21] G. Li, R. Zhu, and Y. Yang, "Polymer solar cells," *Nature Photonics,* **2012**, 6(3), 153-161.

[22] J. Holt, S. Singh, T. Drori, Y. Zhang, and Z. Vardeny, "Optical probes of π-conjugated polymer blends with strong acceptor molecules," *Physical Review B,* **2009**, 79(19), 195210.

[23] S. Singh, and Z. V. Vardeny, "Ultrafast transient spectroscopy of polymer/fullerene blends for organic photovoltaic applications," *Materials*, **2013**, 6(3), 897-910.

[24] T. Drori, C.-X. Sheng, A. Ndobe, S. Singh, J. Holt, and Z. Vardeny, "Below-gap excitation of π-conjugated polymer-fullerene blends: Implications for bulk organic heterojunction solar cells," *Physical Review Letters,* **2008**, 101(3), 037401.

[25] S. Singh, B. Pandit, T. P. Basel, S. Li, D. Laird, and Z. V. Vardeny, "Two-step charge photogeneration dynamics in polymer/fullerene blends for photovoltaic applications," *Physical Review B,* **2012**, 85(20), 205206.

[26] T. Drori, J. Holt, and Z. Vardeny, "Optical studies of the charge transfer complex in polythiophene/fullerene blends for organic photovoltaic applications," *Physical Review B*, **2010**, 82(7), 075207.

[27] R. A. Street, S. A. Hawks, P. P. Khlyabich, G. Li, B. J. Schwartz, B. C. Thompson, and Y. Yang, "Electronic structure and transition energies in polymer-fullerene bulk heterojunctions," *The Journal of Physical Chemistry C*, **2014**, 118(38), 21873-21883.

[28] M. Graetzel, R. A. Janssen, D. B. Mitzi, and E. H. Sargent, "Materials interface engineering for solution-processed photovoltaics," *Nature*, **2012**, 488(7411), 304-312.

[29] W. Shockley, and H. J. Queisser, "Detailed balance limit of efficiency of p-n junction solar cells," *Journal Of Applied Physics*, **1961**, 32(3), 510-519.

[30] T. Tiedje, E. Yablonovitch, G. D. Cody, and B. G. Brooks, "Limiting efficiency of silicon solar cells," *Electron Devices, IEEE Transactions on*, **1984**, 31(5), 711-716.

[31] S. Günes, H. Neugebauer, and N. S. Sariciftci, "Conjugated polymer-based organic solar cells," *Chemical Reviews*, **2007**, 107(4), 1324-1338.

[32] W. Tress, K. Leo, and M. Riede, "Optimum mobility, contact properties, and open-circuit voltage of organic solar cells: A drift-diffusion simulation study," *Physical Review B*, **2012**, 85(15), 155201.

[33] S. R. Forrest, "The limits to organic photovoltaic cell efficiency," *MRS Bulletin*, **2005**, 30(01), 28-32.

[34] M. T. Dang, L. Hirsch, and G. Wantz, "P3HT:PCBM, best seller in polymer photovoltaic research," *Advanced Materials*, **2011**, 23(31), 3597-3602.

[35] Z. Chen, P. Cai, J. Chen, X. Liu, L. Zhang, L. Lan, J. Peng, Y. Ma, and Y. Cao, "Low band-gap conjugated polymers with strong interchain aggregation and very high hole mobility towards highly efficient thick-film polymer solar cells," *Advanced Materials*, **2014**, 26(16), 2586-2591.

[36] J. Gao, L. Dou, W. Chen, C. C. Chen, X. Guo, J. You, B. Bob, W. H. Chang, J. Strzalka, and C. Wang, "Improving structural order for a high-performance diketopyrrolopyrrole-based polymer solar cell with a thick active layer," *Advanced Energy Materials*, **2014**, 4(5).

[37] B. Qi, and J. Wang, "Open-circuit voltage in organic solar cells," *Journal of Materials Chemistry*, **2012**, 22(46), 24315-24325.

[38] Z. He, C. Zhong, S. Su, M. Xu, H. Wu, and Y. Cao, "Enhanced power-conversion efficiency in polymer solar cells using an inverted device structure," *Nature Photonics*, **2012**, 6(9), 591-595.

[39] G. Garcia-Belmonte, and J. Bisquert, "Open-circuit voltage limit caused by recombination through tail states in bulk heterojunction polymer-fullerene solar cells," *Applied Physics Letters,* **2010**, 96(11), 113301.

[40] M. A. Alam, B. Ray, M. R. Khan, and S. Dongaonkar, "The essence and efficiency limits of bulk-heterostructure organic solar cells: A polymer-to-panel perspective," *Journal of Materials Research,* **2013**, 28(04), 541-557.

[41] B. P. Rand, D. P. Burk, and S. R. Forrest, "Offset energies at organic semiconductor heterojunctions and their influence on the open-circuit voltage of thin-film solar cells," *Physical Review B,* **2007**, 75(11), 115327.

[42] K. Vandewal, K. Tvingstedt, A. Gadisa, O. Inganäs, and J. V. Manca, "On the origin of the open-circuit voltage of polymer-fullerene solar cells," *Nature Materials,* **2009**, 8(11), 904-909.

[43] D. Veldman, S. C. Meskers, and R. A. Janssen, "The energy of charge-transfer states in electron donor-acceptor blends: insight into the energy losses in organic solar cells," *Advanced Functional Materials,* **2009**, 19(12), 1939-1948.

[44] M. C. Scharber, D. Mühlbacher, M. Koppe, P. Denk, C. Waldauf, A. J. Heeger, and C. J. Brabec, "Design rules for donors in bulk-heterojunction solar cells-Towards 10% energy-conversion efficiency," *Advanced Materials,* **2006**, 18(6), 789-794.

[45] G. Dennler, H.-J. Prall, R. Koeppe, M. Egginger, R. Autengruber, and N. S. Sariciftci, "Enhanced spectral coverage in tandem organic solar cells," *Applied Physics Letters,* **2006**, 89(7), 073502-073503.

[46] M. Yamaguchi, T. Takamoto, K. Araki, and N. Ekins-Daukes, "Multi-junction III–V solar cells: Current status and future potential," *Solar Energy,* **2005**, 79(1), 78-85.

[47] F. Dimroth, "High-efficiency solar cells from III-V compound semiconductors," *Physica Status Solidi (c),* **2006**, 3(3), 373-379.

[48] R. Schueppel, R. Timmreck, N. Allinger, T. Mueller, M. Furno, C. Uhrich, K. Leo, and M. Riede, "Controlled current matching in small molecule organic tandem solar cells using doped spacer layers," *Journal of Applied Physics,* **2010**, 107(4), 044503.

[49] M. A. Green, K. Emery, Y. Hishikawa, W. Warta, and E. D. Dunlop, "Solar cell efficiency tables (version 39)," *Progress In Photovoltaics: Research And Applications,* **2012**, 20(1), 12-20.

[50] G. Dennler, M. C. Scharber, T. Ameri, P. Denk, K. Forberich, C. Waldauf, and C. J. Brabec, "Design rules for donors in bulk-heterojunction tandem solar cells towards 15% energy-conversion efficiency," *Advanced Materials,* **2008**, 20(3), 579-583.

[51] T. Ameri, N. Li, and C. J. Brabec, "Highly efficient organic tandem solar cells: a follow up review," *Energy & Environmental Science,* **2013**, 6(8), 2390-2413.

[52] M. Hiramoto, M. Suezaki, and M. Yokoyama, “Effect of thin gold interstitial-layer on the photovoltaic properties of tandem organic solar cell,” *Chemistry Letters,* **1990**(3), 327-330.

[53] A. Yakimov, and S. Forrest, “High photovoltage multiple-heterojunction organic solar cells incorporating interfacial metallic nanoclusters,” *Applied Physics Letters,* **2002**, 80(9), 1667-1669.

[54] Y. Yuan, J. Huang, and G. Li, “Intermediate layers in tandem organic solar cells,” *Green,* **2011**, 1(1), 65-80.

[55] R. Timmreck, S. Olthof, K. Leo, and M. K. Riede, “Highly doped layers as efficient electron–hole recombination contacts for tandem organic solar cells,” *Journal of Applied Physics,* **2010**, 108(3), 033108.

[56] J. Y. Kim, K. Lee, N. E. Coates, D. Moses, T.-Q. Nguyen, M. Dante, and A. J. Heeger, “Efficient tandem polymer solar cells fabricated by all-solution processing,” *Science,* **2007**, 317(5835), 222-225.

[57] L. Dou, J. You, J. Yang, C.-C. Chen, Y. He, S. Murase, T. Moriarty, K. Emery, G. Li, and Y. Yang, “Tandem polymer solar cells featuring a spectrally matched low-bandgap polymer,” *Nature Photonics,* **2012**, 6(3), 180-185.

[58] Y. Zhou, C. Fuentes-Hernandez, J. Shim, J. Meyer, A. J. Giordano, H. Li, P. Winget, T. Papadopoulos, H. Cheun, and J. Kim, “A universal method to produce low-work function electrodes for organic electronics,” *Science,* **2012**, 336(6079), 327-332.

[59] W. Tress, A. Merten, M. Furno, M. Hein, K. Leo, and M. Riede, “Correlation of absorption profile and fill factor in organic solar cells: The role of mobility imbalance,” *Advanced Energy Materials,* **2013**, 3(5), 631-638.

[60] P. P. Boix, J. Ajuria, I. Etxebarria, R. Pacios, G. Garcia-Belmonte, and J. Bisquert, “Role of ZnO electron-selective layers in regular and inverted bulk heterojunction solar cells,” *The Journal of Physical Chemistry Letters,* **2011**, 2(5), 407-411.

[61] S. Murase, and Y. Yang, “Solution processed MoO3 interfacial layer for organic photovoltaics prepared by a facile synthesis method,” *Advanced Materials,* **2012**, 24(18), 2459-2462.

[62] J. Yoon, A. J. Baca, S.-I. Park, P. Elvikis, J. B. Geddes, L. Li, R. H. Kim, J. Xiao, S. Wang, and T.-H. Kim, “Ultrathin silicon solar microcells for semitransparent, mechanically flexible and microconcentrator module designs,” *Nature Materials,* **2008**, 7(11), 907-915.

[63] A. Boueke, "Progress in semitransparent silicon solar cells." pp. 1709-1712.

[64] R. Stouffs, P. Janssen, S. Roudavski, and B. Tunçer, "Semi-transparent building integrated photovoltaic facades." **2013**.

[65] G. Yu, J. Gao, J. Hummelen, F. Wudl, and A. Heeger, "Polymer photovoltaic cells: enhanced efficiencies via a network of internal donor-acceptor heterojunctions," *Science,* **1995**, 270(5243), 1789-1790.

[66] C. J. Brabec, S. Gowrisanker, J. J. Halls, D. Laird, S. Jia, and S. P. Williams, "Polymer-fullerene bulk-heterojunction solar cells," *Advanced Materials,* **2010**, 22(34), 3839-3856.

[67] G. Dennler, M. C. Scharber, and C. J. Brabec, "Polymer-fullerene bulk-heterojunction solar cells," *Advanced Materials,* **2009**, 21(13), 1323-1338.

[68] C. C. Chen, W. H. Chang, K. Yoshimura, K. Ohya, J. You, J. Gao, Z. Hong, and Y. Yang, "An efficient triple-junction polymer solar cell having a power conversion efficiency exceeding 11%," *Advanced Materials,* **2014**, 26(32), 5670-5677.

[69] D. J. Lipomi, B. C. K. Tee, M. Vosgueritchian, and Z. Bao, "Stretchable organic solar cells," *Advanced Materials,* **2011**, 23(15), 1771-1775.

[70] H. J. Park, T. Xu, J. Y. Lee, A. Ledbetter, and L. J. Guo, "Photonic color filters integrated with organic solar cells for energy harvesting," *ACS Nano,* **2011**, 5(9), 7055-7060.

[71] A. Henemann, "BIPV: Built-in solar energy," *Renewable Energy Focus,* **2008**, 9(6), 14-19.

[72] M. Pagliaro, R. Ciriminna, and G. Palmisano, "BIPV: merging the photovoltaic with the construction industry," *Progress in Photovoltaics: Research and Applications,* **2010**, 18(1), 61-72.

[73] Y.-Y. Lee, K.-H. Tu, C.-C. Yu, S.-S. Li, J.-Y. Hwang, C.-C. Lin, K.-H. Chen, L.-C. Chen, H.-L. Chen, and C.-W. Chen, "Top laminated graphene electrode in a semitransparent polymer solar cell by simultaneous thermal annealing/releasing method," *ACS Nano,* **2011**, 5(8), 6564-6570.

[74] Y. Zhou, H. Cheun, S. Choi, W. J. Potscavage Jr, C. Fuentes-Hernandez, and B. Kippelen, "Indium tin oxide-free and metal-free semitransparent organic solar cells," *Applied Physics Letters,* **2010**, 97(15), 153304.

[75] D. S. Hecht, L. Hu, and G. Irvin, "Emerging transparent electrodes based on thin films of carbon nanotubes, graphene, and metallic nanostructures," *Advanced Materials,* **2011**, 23(13), 1482-1513.

[76] G.-M. Ng, E. L. Kietzke, T. Kietzke, L.-W. Tan, P.-K. Liew, and F. Zhu, "Optical enhancement in semitransparent polymer photovoltaic cells," *Applied Physics Letters,* **2007**, 90(10), 103505.

[77] K.-S. Chen, J.-F. Salinas, H.-L. Yip, L. Huo, J. Hou, and A. K.-Y. Jen, "Semi-transparent polymer solar cells with 6% PCE, 25% average visible transmittance and a color

rendering index close to 100 for power generating window applications," *Energy & Environmental Science*, **2012**, 5(11), 9551-9557.

[78] Y. Zhou, H. Cheun, S. Choi, C. Fuentes-Hernandez, and B. Kippelen, "Optimization of a polymer top electrode for inverted semitransparent organic solar cells," *Organic Electronics*, **2011**, 12(5), 827-831.

[79] J. Czolk, A. Puetz, D. Kutsarov, M. Reinhard, U. Lemmer, and A. Colsmann, "Inverted semi-transparent polymer solar cells with transparency color rendering indices approaching 100," *Advanced Energy Materials*, **2013**, 3(3), 386-390.

[80] R. Betancur, P. Romero-Gomez, A. Martinez-Otero, X. Elias, M. Maymó, and J. Martorell, "Transparent polymer solar cells employing a layered light-trapping architecture," *Nature Photonics*, **2013**, 7(12), 995-1000.

[81] C. C. Chueh, S. C. Chien, H. L. Yip, J. F. Salinas, C. Z. Li, K. S. Chen, F. C. Chen, W. C. Chen, and A. K. Y. Jen, "Toward high-performance semi-transparent polymer solar cells: Optimization of ultra-thin light absorbing layer and transparent cathode architecture," *Advanced Energy Materials*, **2013**, 3(4), 417-423.

[82] T. Ameri, G. Dennler, C. Waldauf, H. Azimi, A. Seemann, K. Forberich, J. Hauch, M. Scharber, K. Hingerl, and C. J. Brabec, "Fabrication, optical modeling, and color characterization of semitransparent bulk-heterojunction organic solar cells in an inverted structure," *Advanced Functional Materials*, **2010**, 20(10), 1592-1598.

[83] Y. Galagan, J.-E. JM Rubingh, R. Andriessen, C.-C. Fan, P. WM Blom, S. C Veenstra, and J. M Kroon, "ITO-free flexible organic solar cells with printed current collecting grids," *Solar Energy Materials and Solar Cells*, **2011**, 95(5), 1339-1343.

[84] D. S. Leem, A. Edwards, M. Faist, J. Nelson, D. D. Bradley, and J. C. de Mello, "Efficient organic solar cells with solution-processed silver nanowire electrodes," *Advanced Materials*, **2011**, 23(38), 4371-4375.

[85] M. Song, D. S. You, K. Lim, S. Park, S. Jung, C. S. Kim, D. H. Kim, D. G. Kim, J. K. Kim, and J. Park, "Highly efficient and bendable organic solar cells with solution-processed silver nanowire electrodes," *Advanced Functional Materials*, **2013**, 23(34), 4177-4184.

[86] J. B. Franklin, J. B. Gilchrist, J. M. Downing, K. A. Roy, and M. A. McLachlan, "Transparent conducting oxide top contacts for organic electronics," *Journal of Materials Chemistry C*, **2014**, 2(1), 84-89.

[87] H. Schmidt, H. Flügge, T. Winkler, T. Bülow, T. Riedl, and W. Kowalsky, "Efficient semitransparent inverted organic solar cells with indium tin oxide top electrode," *Applied Physics Letters*, **2009**, 94(24), 243302.

[88] M. Vosgueritchian, D. J. Lipomi, and Z. Bao, "Highly conductive and transparent PEDOT:PSS films with a fluorosurfactant for stretchable and flexible transparent electrodes," *Advanced Functional Materials,* **2012**, 22(2), 421-428.

[89] Y. Wang, S. W. Tong, X. F. Xu, B. Özyilmaz, and K. P. Loh, "Interface engineering of layer-by-layer stacked graphene anodes for high-performance organic solar cells," *Advanced Materials,* **2011**, 23(13), 1514-1518.

[90] M. H. Park, J. H. Li, A. Kumar, G. Li, and Y. Yang, "Doping of the metal oxide nanostructure and its influence in organic electronics," *Advanced Functional Materials,* **2009**, 19(8), 1241-1246.

[91] L. Dou, J. Gao, E. Richard, J. You, C.-C. Chen, K. C. Cha, Y. He, G. Li, and Y. Yang, "Systematic investigation of benzodithiophene-and diketopyrrolopyrrole-based low-bandgap polymers designed for single junction and tandem polymer solar cells," *Journal of the American Chemical Society,* **2012**, 134(24), 10071-10079.

[92] A. Du Pasquier, H. E. Unalan, A. Kanwal, S. Miller, and M. Chhowalla, "Conducting and transparent single-wall carbon nanotube electrodes for polymer-fullerene solar cells," *Applied Physics Letters,* **2005**, 87(20), 203511.

[93] M. W. Rowell, M. A. Topinka, M. D. McGehee, H.-J. Prall, G. Dennler, N. S. Sariciftci, L. Hu, and G. Gruner, "Organic solar cells with carbon nanotube network electrodes," *Applied Physics Letters,* **2006**, 88(23), 233506.

[94] H. A. Becerril, J. Mao, Z. Liu, R. M. Stoltenberg, Z. Bao, and Y. Chen, "Evaluation of solution-processed reduced graphene oxide films as transparent conductors," *ACS Nano,* **2008**, 2(3), 463-470.

[95] S. Pang, Y. Hernandez, X. Feng, and K. Müllen, "Graphene as transparent electrode material for organic electronics," *Advanced Materials,* **2011**, 23(25), 2779-2795.

[96] Y. H. Kim, C. Sachse, M. L. Machala, C. May, L. Müller-Meskamp, and K. Leo, "Highly conductive PEDOT:PSS electrode with optimized solvent and thermal post-treatment for ITO-free organic solar cells," *Advanced Functional Materials,* **2011**, 21(6), 1076-1081.

[97] Y. Xia, K. Sun, and J. Ouyang, "Solution-processed metallic conducting polymer films as transparent electrode of optoelectronic devices," *Advanced Materials,* **2012**, 24(18), 2436-2440.

[98] L. Hu, H. S. Kim, J.-Y. Lee, P. Peumans, and Y. Cui, "Scalable coating and properties of transparent, flexible, silver nanowire electrodes," *ACS Nano,* **2010**, 4(5), 2955-2963.

[99] E. C. Garnett, W. Cai, J. J. Cha, F. Mahmood, S. T. Connor, M. G. Christoforo, Y. Cui, M. D. McGehee, and M. L. Brongersma, "Self-limited plasmonic welding of silver nanowire junctions," *Nature Materials,* **2012**, 11(3), 241-249.

[100] R. Zhu, C.-H. Chung, K. C. Cha, W. Yang, Y. B. Zheng, H. Zhou, T.-B. Song, C.-C. Chen, P. S. Weiss, and G. Li, "Fused silver nanowires with metal oxide nanoparticles and organic polymers for highly transparent conductors," *ACS Nano,* **2011**, 5(12), 9877-9882.

[101] Z. Xu, L. M. Chen, G. Yang, C. H. Huang, J. Hou, Y. Wu, G. Li, C. S. Hsu, and Y. Yang, "Vertical phase separation in poly (3-hexylthiophene):fullerene derivative blends and its advantage for inverted structure solar cells," *Advanced Functional Materials,* **2009**, 19(8), 1227-1234.

[102] J. Y. Kim, S. H. Kim, H. H. Lee, K. Lee, W. Ma, X. Gong, and A. J. Heeger, "New Architecture for high-efficiency polymer photovoltaic cells using solution-based titanium oxide as an optical spacer," *Advanced Materials,* **2006**, 18(5), 572-576.

[103] C.-C. Chen, L. Dou, R. Zhu, C.-H. Chung, T.-B. Song, Y. B. Zheng, S. Hawks, G. Li, P. S. Weiss, and Y. Yang, "Visibly transparent polymer solar cells produced by solution processing," *ACS Nano,* **2012**, 6(8), 7185-7190.

[104] L. Dou, W. H. Chang, J. Gao, C. C. Chen, J. You, and Y. Yang, "A selenium-substituted low-bandgap polymer with versatile photovoltaic applications," *Advanced Materials,* **2013**, 25(6), 825-831.

[105] Z. He, C. Zhong, X. Huang, W. Y. Wong, H. Wu, L. Chen, S. Su, and Y. Cao, "Simultaneous enhancement of open-circuit voltage, short-circuit current density, and fill factor in polymer solar cells," *Advanced Materials,* **2011**, 23(40), 4636-4643.

[106] J.-Y. Lee, S. T. Connor, Y. Cui, and P. Peumans, "Semitransparent organic photovoltaic cells with laminated top electrode," *Nano Letters,* **2010**, 10(4), 1276-1279.

[107] X. Wang, T. Ishwara, W. Gong, M. Campoy‐Quiles, J. Nelson, and D. D. Bradley, "High-performance metal-free solar cells using stamp transfer printed vapor phase polymerized poly (3, 4-ethylenedioxythiophene) top anodes," *Advanced Functional Materials,* **2012**, 22(7), 1454-1460.

[108] S. Schubert, J. Meiss, L. Müller‐Meskamp, and K. Leo, "Improvement of transparent metal top electrodes for organic solar cells by introducing a high surface energy seed layer," *Advanced Energy Materials,* **2013**, 3(4), 438-443.

[109] Z. Tang, Z. George, Z. Ma, J. Bergqvist, K. Tvingstedt, K. Vandewal, E. Wang, L. M. Andersson, M. R. Andersson, and F. Zhang, "Semi-transparent tandem organic solar cells with 90% internal quantum efficiency," *Advanced Energy Materials,* **2012**, 2(12), 1467-1476.

[110] A. Colsmann, A. Puetz, A. Bauer, J. Hanisch, E. Ahlswede, and U. Lemmer, "Efficient semi-transparent organic solar cells with good transparency color perception and rendering properties," *Advanced Energy Materials,* **2011**, 1(4), 599-603.

[111] F. Huang, K.-S. Chen, H.-L. Yip, S. K. Hau, O. Acton, Y. Zhang, J. Luo, and A. K.-Y. Jen, "Development of new conjugated polymers with donor-π-bridge-acceptor side chains for high performance solar cells," *Journal of the American Chemical Society,* **2009**, 131(39), 13886-13887.

[112] S. Sista, M. H. Park, Z. Hong, Y. Wu, J. Hou, W. L. Kwan, G. Li, and Y. Yang, "Highly efficient tandem polymer photovoltaic cells," *Advanced Materials,* **2010**, 22(3), 380-383.

[113] J. Yang, R. Zhu, Z. Hong, Y. He, A. Kumar, Y. Li, and Y. Yang, "A robust inter-connecting layer for achieving high performance tandem polymer solar cells," *Advanced Materials,* **2011**, 23(30), 3465-3470.

[114] G. Kim, J. Kong, J. Kim, H. Kang, H. Back, H. Kim, and K. Lee, "Overcoming the light-soaking problem in inverted polymer solar cells by introducing a heavily doped titanium sub-oxide functional layer," *Advanced Energy Materials*, **2014**.

[115] S. K. Hau, H.-L. Yip, H. Ma, and A. K. Jen, "High performance ambient processed inverted polymer solar cells through interfacial modification with a fullerene self-assembled monolayer," *Applied Physics Letters,* **2008**, 93(23), 233304-233304-3.

[116] Y. Li, L. Mao, Y. Gao, P. Zhang, C. Li, C. Ma, Y. Tu, Z. Cui, and L. Chen, "ITO-free photovoltaic cell utilizing a high-resolution silver grid current collecting layer," *Solar Energy Materials and Solar Cells,* **2013**, 113, 85-89.

[117] S. I. Na, S. S. Kim, J. Jo, and D. Y. Kim, "Efficient and flexible ITO-free organic solar cells using highly conductive polymer anodes," *Advanced Materials,* **2008**, 20(21), 4061-4067.

[118] T. R. Andersen, H. F. Dam, M. Hösel, M. Helgesen, J. E. Carlé, T. T. Larsen-Olsen, S. A. Gevorgyan, J. W. Andreasen, J. Adams, and N. Li, "Scalable, ambient atmosphere roll-to-roll manufacture of encapsulated large area, flexible organic tandem solar cell modules," *Energy & Environmental Science,* **2014**, 7(9), 2925-2933.

[119] P. Sullivan, S. Schumann, R. Da Campo, T. Howells, A. Duraud, M. Shipman, R. A. Hatton, and T. S. Jones, "Ultra-high voltage multijunction organic solar cells for low-power electronic applications," *Advanced Energy Materials,* **2013**, 3(2), 239-244.

[120] J. Wu, Y. Li, Q. Tang, G. Yue, J. Lin, M. Huang, and L. Meng, "Bifacial dye-sensitized solar cells: A strategy to enhance overall efficiency based on transparent polyaniline electrode," *Scientific Reports,* **2014**, 4.

[121] S. H. Moon, S. J. Park, Y. J. Hwang, D.-K. Lee, Y. Cho, D.-W. Kim, and B. K. Min, "Printable, wide band-gap chalcopyrite thin films for power generating window applications," *Scientific Reports,* **2014**, 4.

[122] N. Yeh, and P. Yeh, "Organic solar cells: their developments and potentials," *Renewable and Sustainable Energy Reviews,* **2013**, 21, 421-431.

[123] R. R. Søndergaard, M. Hösel, and F. C. Krebs, "Roll-to-Roll fabrication of large area functional organic materials," *Journal of Polymer Science Part B: Polymer Physics,* **2013**, 51(1), 16-34.

[124] F. Livi, R. R. Søndergaard, T. R. Andersen, B. Roth, S. Gevorgyan, H. F. Dam, J. E. Carl, M. Helgesen, G. D. Spyropoulos, and J. Adams, "Round-Robin studies on roll-processed ITO-free organic tandem solar cells combined with inter-laboratory stability studies," *Energy Technology,* **2014**.

[125] G. D. Spyropoulos, P. Kubis, N. Li, D. Baran, L. Lucera, M. Salvador, T. Ameri, M. Voigt, F. C. Krebs, and C. J. Brabec, "Flexible organic tandem solar modules with 6% efficiency: Combining roll-to-roll compatible processing with high geometric fill factors," *Energy & Environmental Science,* **2014**, 7(10), 3284-3290.

[126] T. Xu, and L. Yu, "How to design low bandgap polymers for highly efficient organic solar cells," *Materials Today,* **2014**, 17(1), 11-15.

[127] N. Kaur, M. Singh, D. Pathak, T. Wagner, and J. Nunzi, "Organic materials for photovoltaic applications: Review and mechanism," *Synthetic Metals,* **2014**, 190, 20-26.

[128] D. H. Apaydın, D. E. Yıldız, A. Cirpan, and L. Toppare, "Optimizing the organic solar cell efficiency: Role of the active layer thickness," *Solar Energy Materials and Solar Cells,* **2013**, 113, 100-105.

[129] M. Jørgensen, J. E. Carlé, R. R. Søndergaard, M. Lauritzen, N. A. Dagnæs-Hansen, S. L. Byskov, T. R. Andersen, T. T. Larsen-Olsen, A. P. Böttiger, and B. Andreasen, "The state of organic solar cells—A meta analysis," *Solar Energy Materials and Solar Cells,* **2013**, 119, 84-93.

[130] J. Sakai, K. Kawano, T. Yamanari, T. Taima, Y. Yoshida, A. Fujii, and M. Ozaki, "Efficient organic photovoltaic tandem cells with novel transparent conductive oxide interlayer and poly (3-hexylthiophene):fullerene active layers," *Solar Energy Materials and Solar Cells*, **2010**, 94(2), 376-380.

[131] V. S. Gevaerts, A. Furlan, M. M. Wienk, M. Turbiez, and R. A. Janssen, "Solution processed polymer tandem solar cell using efficient small and wide bandgap polymer: fullerene blends," *Advanced Materials,* **2012**, 24(16), 2130-2134.

[132] D. Moet, P. De Bruyn, J. Kotlarski, and P. Blom, "Enhanced efficiency in double junction polymer: fullerene solar cells," *Organic Electronics,* **2010**, 11(11), 1821-1827.

[133] J. Gilot, M. M. Wienk, and R. A. Janssen, "Optimizing polymer tandem solar cells," *Advanced Materials,* **2010**, 22(8), E67-E71.

[134] S. H. Liao, H. J. Jhuo, Y. S. Cheng, and S. A. Chen, "Fullerene derivative-doped zinc oxide nanofilm as the cathode of inverted polymer solar cells with low-bandgap polymer (PTB7-Th) for high performance," *Advanced Materials,* **2013**, 25(34), 4766-4771.

[135] G. Zhao, Y. He, and Y. Li, "6.5% efficiency of polymer solar cells based on poly (3-hexylthiophene) and indene-C60 bisadduct by device optimization," *Advanced Materials,* **2010**, 22(39), 4355-4358.

[136] W. J. Beek, M. M. Wienk, M. Kemerink, X. Yang, and R. A. Janssen, "Hybrid zinc oxide conjugated polymer bulk heterojunction solar cells," *The Journal of Physical Chemistry B,* **2005**, 109(19), 9505-9516.

[137] J. Gilot, M. M. Wienk, and R. A. Janssen, "Measuring the external quantum efficiency of two-terminal polymer tandem solar cells," *Advanced Functional Materials,* **2010**, 20(22), 3904-3911.

[138] S. Zhang, L. Ye, W. Zhao, D. Liu, H. Yao, and J. Hou, "Side chain selection for designing highly efficient photovoltaic polymers with 2D-conjugated structure," *Macromolecules,* **2014**, 47(14), 4653-4659.

[139] L. Dou, C.-C. Chen, K. Yoshimura, K. Ohya, W.-H. Chang, J. Gao, Y. Liu, E. Richard, and Y. Yang, "Synthesis of 5h-dithieno [3, 2-b:2', 3'-d] pyran as an electron-rich building block for donor-acceptor type low-bandgap polymers," *Macromolecules,* **2013**, 46(9), 3384-3390.

[140] G. WooáKim, and J. HyukáKwon, "A highly efficient transition metal oxide layer for hole extraction and transport in inverted polymer bulk heterojunction solar cells," *Journal of Materials Chemistry A,* **2013**, 1(23), 6895-6900.

[141] T. Stubhan, N. Li, N. A. Luechinger, S. C. Halim, G. J. Matt, and C. J. Brabec, "High fill factor polymer solar cells incorporating a low temperature solution processed WO3 hole extraction layer," *Advanced Energy Materials,* **2012**, 2(12), 1433-1438.

[142] K. H. Wong, K. Ananthanarayanan, J. Luther, and P. Balaya, "Origin of hole selectivity and the role of defects in low-temperature solution-processed molybdenum oxide interfacial layer for organic solar cells," *The Journal of Physical Chemistry C,* **2012**, 116(31), 16346-16351.

[143] L. A. Pettersson, L. S. Roman, and O. Inganas, "Modeling photocurrent action spectra of photovoltaic devices based on organic thin films," *Journal of Applied Physics,* **1999**, 86(1), 487-496.

[144] H. Hoppe, N. Arnold, N. Sariciftci, and D. Meissner, "Modeling the optical absorption within conjugated polymer/fullerene-based bulk-heterojunction organic solar cells," *Solar Energy Materials and Solar Cells,* **2003**, 80(1), 105-113.

[145] T. Kim, H. Kim, J. Park, H. Kim, Y. Yoon, S.-M. Kim, C. Shin, H. Jung, I. Kim, and D. S. Jeong, "Triple-junction hybrid tandem solar cells with amorphous silicon and polymer-fullerene blends," *Scientific Reports,* **2014**, 4.

[146] S. Kouijzer, S. Esiner, C. H. Frijters, M. Turbiez, M. M. Wienk, and R. A. Janssen, "Efficient inverted tandem polymer solar cells with a solution-processed recombination layer," *Advanced Energy Materials,* **2012**, 2(8), 945-949.

[147] J. D. Chen, C. Cui, Y. Q. Li, L. Zhou, Q. D. Ou, C. Li, Y. Li, and J. X. Tang, "Single-junction polymer solar cells exceeding 10% power conversion efficiency," *Advanced Materials,* **2014**.

[148] J. You, L. Dou, K. Yoshimura, T. Kato, K. Ohya, T. Moriarty, K. Emery, C.-C. Chen, J. Gao, and G. Li, "A polymer tandem solar cell with 10.6% power conversion efficiency," *Nature Communications,* **2013**, 4, 1446.

[149] W. Guter, J. Schöne, S. P. Philipps, M. Steiner, G. Siefer, A. Wekkeli, E. Welser, E. Oliva, A. W. Bett, and F. Dimroth, "Current-matched triple-junction solar cell reaching 41.1% conversion efficiency under concentrated sunlight," *Applied Physics Letters,* **2009**, 94(22), 223504.

[150] I. Mathews, D. O'Mahony, B. Corbett, and A. P. Morrison, "Theoretical performance of multi-junction solar cells combining III-V and Si materials," *Optics Express,* **2012**, 20(105), A754-A764.

[151] O. Adebanjo, P. P. Maharjan, P. Adhikary, M. Wang, S. Yang, and Q. Qiao, "Triple junction polymer solar cells," *Energy & Environmental Science,* **2013**, 6(11), 3150-3170.

[152] E. Zhou, J. Cong, K. Hashimoto, and K. Tajima, "Introduction of a conjugated side chain as an effective approach to improving donor–acceptor photovoltaic polymers," *Energy & Environmental Science,* **2012**, 5(12), 9756-9759.

[153] H.-Y. Chen, J. Hou, S. Zhang, Y. Liang, G. Yang, Y. Yang, L. Yu, Y. Wu, and G. Li, "Polymer solar cells with enhanced open-circuit voltage and efficiency," *Nature Photonics,* **2009**, 3(11), 649-653.

[154] B. Minnaert, and P. Veelaert, "Guidelines for the bandgap combinations and absorption windows for organic tandem and triple-junction solar cells," *Materials,* **2012**, 5(10), 1933-1953.